

Understanding Viscosity Changes due to Polyelectrolyte Surfactant Complexes

From the Department of Chemistry at the Technical University of Darmstadt

submitted in fulfilment of the requirements for the
degree of Doctor rerum naturalium
(Dr. rer. nat.)

Doctoral Thesis
by Giuseppe Rosario Del Sorbo

First assessor: Prof. Dr. Nico van der Vegt
Second assessor: Prof. Dr. Emanuel Schneck

Darmstadt 2022

Date of submission: 21/December/2021

Day of the oral examination: 07/February/2022

Giuseppe Rosario Del Sorbo: Understanding Viscosity
Changes due to Polyelectrolyte Surfactant Complexes.

Darmstadt, Technische Universität Darmstadt,

Year thesis published in TUprints 2022

Day of the viva voce: 07/02/2022

Published under CC BY-NC-ND International

<https://creativecommons.org/licenses/>

Abstract

Aqueous mixtures of polyelectrolytes and oppositely charged surfactants can give rise to a large variety of self-assembled structures, depending on the concentration and chemical nature of both components. These mixtures form clear and homogeneous solutions if either the polyelectrolyte or the surfactant is present in excess. Around charge equilibrium, macroscopic precipitates are formed. For some of these systems, near the phase boundary on the polyelectrolyte-rich side a drastic increase in solution viscosity is observed, due to the formation of nanometric mixed rod-like aggregates. These polyelectrolyte/surfactant complexes act as cross-links between several polyelectrolyte chains, conferring high viscosity but also shear thinning behavior to the solution. In this thesis, different aqueous mixtures of the cationically modified cellulose-based polyelectrolyte JR 400 and anionic surfactants were studied with various characterization techniques to shed light on unexplored aspects of their unique rheological behavior. (I) Solutions of JR 400 and sodium dodecyl sulfate (SDS) were investigated by small angle neutron scattering under rheological deformation (rheo-SANS) to study the origin of the shear thinning behavior while simultaneously inspecting the structural evolution of the rod-like aggregates under steady shear. Results have shown that the shear thinning is correlated to a slight orientation of the aggregates under shear. (II) To investigate the influence of the surfactant tail length on the rheological behavior, complexes consisting of JR 400 and two different surfactants, namely sodium octyl sulphate (SOS, with C8 tail) and sodium tetradecyl sulphate (STS, with C14 tail) were analyzed. SANS and neutron spin-echo (NSE) spectroscopy experiments revealed that the pronounced increase in viscosity for JR 400/STS solutions is due to the presence of mixed aggregates which interconnect different polyelectrolyte chains. Solutions with SOS are not viscous since distinct polyelectrolyte chains are not cross-linked. To gain complementary insights into the mesostructure of the mixed aggregates observed in the experiments, atomistic molecular dynamics (MD) simulations were performed using two charged polypeptides as generic representations of JR 400. MD and experimental results show good qualitative agreement. (III) In order to elucidate the influence of the surfactants headgroup charge, mixtures of JR 400 and the anionic surfactant sodium monododecyl phosphate (SDP) were investigated. At $\text{pH} > 12$, the surfactant headgroup bears two charges and solutions exhibit a water-like behavior, while at lower pH the same mixtures become highly viscous. The change of the mesoscopic structure of the system was again studied using SANS and NSE, revealing that the double-charged form of the surfactant is not hydrophobic enough for the formation of network-forming mixed aggregates. (IV) Finally, further information on the role of the mixed rod-like aggregates in gluing together two or more polyelectrolyte chains was obtained by performing MD simulations involving defined forces. Taking all these results together, the physical mechanisms leading to the unique viscosity behavior of PESC are now better understood.

Wässrige Mischungen von Polyelektrolyten (geladenen Polymeren) und gegensätzlich geladenen Tensiden können, je nach chemischer Zusammensetzung und Konzentration, verschiedenste selbstorganisierte Strukturen hervorbringen. Die Mischungen bilden klare, homogene Lösungen, wenn entweder Polyelektrolyt oder Tensid im Überschuss vorhanden sind. In der Nähe der Ladungsausgleichskonzentrationen bilden sich aber makroskopische Präzipitate. In manchen Fällen beobachtet man bei Annäherung an die Präzipitationsgrenze von der polyelektrolytreichen Seite kommend einen dramatischen Anstieg der Lösungsviskosität, hervorgerufen durch die Bildung gemischter, stäbchenförmiger Nano-Aggregate. Diese sogenannten Polyelektrolyt-Tensid-Komplexe (engl. Abk.: PESCs) erzeugen netzwerkartige Verknüpfungen zwischen verschiedenen Polyelektrolytketten, was eine hohe Viskosität bei gleichzeitigem Scherverdünnungsverhalten zur Folge hat. In der vorliegenden Arbeit wurden Mischungen des kationisch-modifizierten, zellulose-basierten Polyelektrolyts JR400 mit verschiedenen Tensiden mit Hilfe mehrerer Charakterisierungsmethoden untersucht, um Einblicke in die noch unbekannten Aspekte von deren einzigartigen rheologischen Eigenschaften zu gewinnen. (I) Um die Ursache für das beobachtete Scherverdünnungsverhalten zu identifizieren, wurden Mischungen aus JR400 und Natriumdodecylsulfat (engl. Abk.: SDS) mit einer Methode namens rheo-SANS untersucht, bei welcher Kleinwinkelneutronenstreuung (engl. Abk.: SANS) mit gleichzeitig stattfindender rheologischer Deformation kombiniert wird. Dabei zeigte sich, dass der Scherverdünnung eine scher-induzierte Reorientierung der stäbchenförmigen Aggregate zugrunde liegt. (II) Um den Einfluss der Tensidkettenlänge auf die rheologischen Eigenschaften zu verstehen, wurde JR400 mit Tensiden unterschiedlicher Kettenlänge gemischt, und zwar entweder mit Natriumoctylsulfat (engl. Abk.: SOS) mit C8-Ketten oder mit Natriumtetradecylsulfat (engl. Abk.: STS) mit C14-Ketten. Dabei haben SANS und Neutronenspincho-Spektroskopie (NSE-Spektroskopie) gezeigt, dass die beobachtete Viskositäts-erhöhung durch STS-Zugabe der Bildung stäbchenförmiger Aggregate zugeschrieben werden kann. Im Gegensatz dazu führt die Zugabe von SOS nicht zur Bildung solcher Aggregate und dementsprechend auch nicht zu einer erhöhten Viskosität. Um ergänzende Einblicke in die Struktur der gemischten Aggregate zu bekommen wurden atomistische Molekulardynamik (MD) Simulationen an generischen Modellen von JR400 in Form von geladenen Polypeptiden durchgeführt. Diese zeigen beim Vergleich zwischen SOS und STS gute qualitative Übereinstimmung mit den Experimenten. (III) Um den Einfluss der Tensid-Kopfgruppenladung zu beleuchten, wurden im nächsten Schritt Mischungen von JR 400 mit dem Tensid Natriummonododecylphosphat (engl. Abk.: SDP) untersucht. Bei $\text{pH} > 12$ trägt dieses Tensid zwei negative Ladungen und führt nicht zu einer Viskositäts-erhöhung. Bei niedrigerem pH kommt es aber zu dem markanten Viskositätsanstieg. Wieder wurde die zugrundeliegende Strukturbildung dieser Mischungen mittels SANS and NSE charakterisiert. Dabei zeigte sich, dass die zweifach geladene Form des Tensids nicht hydrophob genug zur Bildung netzwerkbildender Aggregate ist. (IV) Am Ende wurde die Rolle der gemischten Aggregate beim Verbinden mehrerer

Polyelektrolytketten mithilfe von MD Simulationen untersucht, bei denen definierte Kräfte auf zwei Polyelektrolytketten ausgeübt wurden.

Zusammenfassend führen die in dieser Arbeit vorgestellten Ergebnisse zu einem besseren Verständnis der physikalischen Mechanismen, die dem einzigartigen Viskositätsverhalten von PESCs zugrunde liegen.

Acknowledgements

First, I would like to express my sincere gratitude to Prof. Dr. Nico van der Vegt for accepting me as his PhD student. I would also like to thank Prof. Dr. Markus Biesalski and Prof. Dr. Giuseppina Luciani for agreeing to be part of my thesis committee. Thanks to my supervisors Dr. Ingo Hoffmann and Prof. Dr. Emanuel Schneck for having given me the possibility of this PhD project, for their time and for their precious advice. Thanks to this opportunity, I grew both personally and professionally.

I will always have in my heart the dynamic environment at ILL, the possibility of collaboration with so many scientists, always available in giving support but mostly for the friends, the special friends I met. I spent an incredible time with people who now have a special place in my life. Interacting with them, I also learned how to look at life with new perspectives, with an open mind.

Infine, voglio ringraziare mia madre, mio padre e mia sorella, per la nostra semplicità, per quello che siamo e costruiamo. Per il loro supporto, il loro coraggio ed il loro esempio. Qualunque siano le distanze sapere di avere un porto sicuro è come sentirsi sempre a casa.

E grazie alla vita, per quello che mi ha offerto, per quello che avrei voluto perché è stato uno stimolo. Ma soprattutto grazie a chi mi ha fatto incontrare, perché sono gli incontri che regalano i colori più belli ed avere ricordi pieni di vita, di passione, di condivisione è l'arma vincente per riuscire sempre a trovare la giusta dose di energia.

Declarations

I hereby declare that I have completed my doctoral thesis independently and only with the means indicated and that I have not yet attempted a doctorate.

Signature

Giuseppe Rosario M. Zorbo

I hereby declare that the electronic version of the doctoral thesis is identical to the written version. The electronic version is available at the examination office.

Signature

Giuseppe Rosario Jullorbo

Contents

1	Introduction	1
1.1	Interaction of Polyelectrolytes and Surfactants	2
1.2	PESCs' Structural Organization	4
1.3	The Cellulose-Based Polyelectrolyte JR 400	6
1.4	PESCs as Rheology Modifiers	8
1.4.1	Mixtures of JR 400 and Oppositely Charged Surfactants	9
1.5	Aim of the Thesis	11
2	Theoretical Background	14
2.1	Dynamic Light Scattering (DLS)	14
2.1.1	Principle	14
2.1.2	Semi-Dilute Polymer Solutions	16
2.2	Rheology	17
2.2.1	Principles	17
2.3	Small Angle Neutron Scattering (SANS)	22
2.3.1	Principle	22
2.3.2	PE Excess Region: Cylindrical Objects	25
2.3.3	Surfactant Excess Regime: Spherical Objects	25
2.4	Neutron Spin-Echo (NSE) Spectroscopy	26
2.4.1	Principle	26
2.5	Molecular Dynamics (MD) Simulations	28
2.5.1	Principle	28
2.5.2	Bonded Interactions	29
2.5.3	Non-Bonded Interactions	29
2.5.4	Boundary Conditions	31
2.5.5	Thermodynamic Ensembles	32
3	Materials, Sample Preparation and Experimental Methods	34
3.1	Chemicals	34
3.2	Sample Preparation	35

3.3	Experimental Methods	36
3.3.1	DLS	36
3.3.2	Rheology	36
3.3.3	SANS	36
3.3.4	NSE	37
3.3.5	MD Simulations	38
4	Investigation of the Mechanism Responsible of the Shear Thinning behavior of PESCs Solution	40
4.1	Introduction	40
4.2	Results and Discussion	41
4.2.1	Rheo-SANS	42
4.3	Conclusion	44
5	The Influence of the Surfactant Tail Length on PESCs Viscosity	45
5.1	Introduction	45
5.2	Results and Discussion	46
5.2.1	Phase behavior	46
5.2.2	Rheological behavior	47
5.2.3	SANS	49
5.2.4	NSE	53
5.2.5	MD Simulations	55
5.3	Conclusions	60
6	Stimuli-Responsive PESCs for the Reversible Control of the Solution Viscosity	63
6.1	Introduction	63
6.2	Results and Discussion	64
6.2.1	Rheological behavior	65
6.2.2	Mesoscopic Structure and Dynamics	66
6.3	Conclusions	68
7	Mechanical Stability of Mixed Aggregates	70
8	Conclusions	78
8.1	Project Overview	78
8.2	Outlook	81
Appendix A	content related to chapter 4	84
A.1	Rheology	84
A.1.1	Rheology Measurements on JR 400/SDS Samples	84
A.2	SANS	86
A.2.1	Modelling the SANS Data	86
A.2.2	SANS Measurements on JR 400/SDS Samples	87
Appendix B	content related to chapter 5	90
B.1	Rheology	90
B.1.1	Rheology Measurements on JR 400/STS Samples	90

B.2	SANS	92
B.2.1	Modeling the SANS Data	92
B.2.2	SANS Measurements on JR 400/SOS and JR 400/STS Samples	92
B.3	DLS	94
B.3.1	DLS Measurements on JR 400/STS Samples	94
B.3.2	DLS Measurement on the pure JR 400 Solution	96
B.4	NSE	96
B.4.1	NSE Measurement on the Pure JR 400 Solution	96
B.4.2	NSE Measurement on the JR 400/STS Solutions	98
B.5	MD Simulations	98
B.5.1	Detailed Description of STS Micelle Simulation Protocol	98
B.5.2	How to Define the Largest Distance to be Considered in a Cluster	98
B.5.3	PLG/SDS Aggregate	99
B.5.4	Minimum vs Detailed Counterions	100
B.5.5	PLL/SOS and PLL/STS from Pre-aggregated Micelle	100
B.5.6	Cluster Analysis	101
Appendix C content related to chapter 6		103
C.1	Materials	103
C.1.1	SDP Titration Curve	103
C.2	Rheology	104
C.2.1	Rheology Measurements on JR 400/SDP Samples	104
C.3	SANS	106
C.3.1	Modelling the SANS Data	106
C.4	NSE	108
C.4.1	Modelling the NSE Data	108
C.4.2	Measurements on SDP ⁻ Samples	109
Bibliography		111

Chapter 1

Introduction

Polyelectrolytes are an important class of polymers that bearing ionizable groups are able to dissociate in polar solvents, resulting in charged polymer chains and small counterions. They are widely used in many industrial formulations [186], including pharmaceutical [38, 237], cosmetics, food, paper industries and water treatment [145, 237]. Numerous synthetic polyelectrolytes are available like polyacrylic acid (PAA), polymethacrylic acid (PMAA), and polystyrene sulfonate (PSS) [174]. The synthesis of new polyelectrolytes allows to confer them specific properties [164] for use in industrial applications [191]. However, due to a modern tendency towards an increasing demand for ecofriendly materials, a great deal of attention has been paid to biopolyelectrolytes (PEs). In this thesis we will focus on the interaction between an oppositely charged cellulose-based polyelectrolyte and alkyl surfactants. Solutions containing biopolyelectrolytes and oppositely charged ionic surfactant have attracted special interest in the past decades [55, 100, 124–126, 158, 168, 257] because their used in a variety of applications, like in the food industry, biotechnology and medicine [65, 67, 140, 162, 200]. The formation of oppositely charged polyelectrolytes-surfactant complexes (PESCs) occurs frequently and the driving forces of this process are intermolecular interactions, both electrostatic and hydrophobic [151]. PESCs can exhibit a plethora of different structures in solution, depending on the chemical parameters of both surfactant and polyelectrolyte [55, 125, 151, 153]. The mesoscopic structures of PESCs depend on several parameters such as the concentration of the components, charge density, molecular weight, functional groups and contour length of the PE as well as packing parameter, head group and tail length of the surfac-

tant [55, 73, 107, 151]. Depending on the different structure these complexes are able to modify the rheological properties of solutions in which they are present, exhibiting their potential use of rheological modifiers [55, 126, 128]. To shed light on the PESCs formation and how they modify solution properties, in the following a concise overview is given.

1.1 Interaction of Polyelectrolytes and Surfactants

To gain insight in the complexation of oppositely charged polyelectrolytes surfactants mixtures it is crucial to understand their self-assembly, by investigating their binding mechanism. Self-assembly is an intermolecular spontaneous association via noncovalent bonds (e.g., electrostatic interactions, hydrogen bonds, or hydrophobic interactions) [292, 297]. In PESCs' formation the two governing interactions are hydrophobic and electrostatic [31, 151, 297, 298]. In the binding process hydrophobic interactions among the surfactant hydrophobic tails play an important role [117, 180]. However, it should be noted that also the counterions release contributes to the complexation due to the entropy gain [42, 166], which further strengthens the interaction between PE and surfactants.

After mixing in solution the two oppositely charged components, surfactant molecules bind to the polymer chains [97, 171, 229]. The binding process is the first step in forming PESCs and it has a strong impact on the morphology and properties of these materials [117, 198, 200], consequently surfactant/polyelectrolyte binding has been extensively studied [97, 114, 118, 198, 229]. The binding characteristics can be described by a binding isotherm which can be measured through several techniques, among which isothermal titration calorimetry (ITC) has been extensively used over the last few years since it offers a complete thermodynamic characterization of binding process [24, 25, 112, 212, 272–274]. The binding equilibria can be considered as [137]:



where O is a binding site on the polymer, S^- is an anionic surfactant, S is an occupied site on the polymer; OO indicates two neighboring sites both empty, OS when one is empty and the other occupied, and SS when both are occupied. Considering the polyelectrolyte as a linear polymer lattice consisting of a large number of equivalent binding sites, it is possible

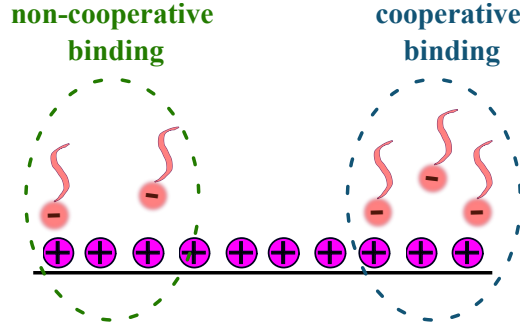


Figure 1.1: Non-cooperative and cooperative binding of surfactant to polyelectrolyte.

to distinguish two different mechanisms of adsorption: cooperative and non-cooperative. In the cooperative binding the adsorption of other molecules is promoted on sites adjacent to one already filled, while in non-cooperative binding on sites adjacent to a vacant one, see fig. 1.1, [151, 163]. The non-cooperative mechanism is described by the equilibrium constant K , see eq. (1.1.1). The strength of the cooperative adsorption is described by the equilibrium constant Ku where u is the cooperativity parameter, see eq. (1.1.2). Describing the binding isotherm with the Yang-Satake model [229], based on the Zimm-Bragg theory [301], the average fractional coverage is expressed as: [229]

$$\beta = \frac{1}{2} \left[1 + \frac{KuC_s - 1}{\sqrt{(1 - KuC_s)^2 + 4KC_s}} \right] \quad (1.1.3)$$

where C_s is the free surfactant concentration. Although the model is widely used to treat binding isotherms for different systems [89, 93, 155, 168, 169, 279], some of them show deviations from the model. The model, in fact, does not take in account the steric hindrance between adjacent adsorbed surfactant's headgroups and interactions between the adjacent bound ligands separated by an unoccupied site [198, 199].

More recently, Chiappisi et al. [56] introduced a new contribution in the model. They implemented the Yang-Satake model, that considers only the cooperative and non-cooperative binding, with a new process: the transfer of bound surfactant from the non-cooperatively bound to the cooperatively bound state. This contribution is particularly important near the critical aggregation concentration (CAC), where the binding becomes mainly cooperative. For PE/surfactant mixtures, the CAC is usually a few orders of magnitude lower than the critical micellization concentration (CMC) of the free surfactant [11, 17, 128, 162, 163, 265]. Non-cooperative binding occurs below the CAC at very low surfactant concentration, as there should be very few occupied sites when the surfactant interacts with the polymer. Therefore, above the CAC the binding mechanism becomes cooperative [137, 163]. The CAC value is influenced by the strength of electrostatic or hydropho-

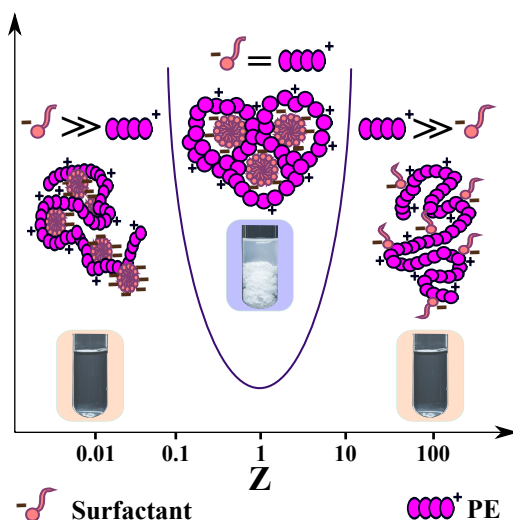


Figure 1.2: Schematic representation of the phase diagram of oppositely charged PE/surfactant solution as a function of Z . In excess of either PE or surfactant the solution is clear and lives in the one-phase region. Differently, the charge equilibrium leads to the precipitation.

bic interactions. Increasing the polyelectrolyte charge density, for example, increases the strength of the electrostatic interactions. Consequently, the surfactant-PE association occurs at lower surfactant concentrations, decreasing the CAC [151, 171]. A decrease of the CAC, furthermore, is also effectuated by increasing the surfactant chain length due to the enhanced propensity of hydrophobic interactions between PE-surfactant and surfactant-surfactant [73, 151, 269]. However, there are many other parameters like added salt, pH, temperature or added hydrophobic regions [151] that affect the CAC.

1.2 PESCs' Structural Organization

The strong attractive interaction between oppositely charged PEs and surfactants leads to an associative phase separation [171, 209, 258, 259] of the PE/surfactant complex. At a given polyelectrolyte concentration with a gradual increase of surfactant amount in solution, whose ratio is expressed by the parameter $Z = [\text{PE charges}]/[\text{surfactant charges}]$, the mixtures show a phase diagram with 3 distinct regions, see fig. 1.2. At low surfactant concentrations, $Z > 1$, in presence of PE excess, the system exhibits one-phase behavior, with transparent solutions. As the surfactant concentration increases, i.e., reducing Z , the effective charges on the PE chains start to be reduced because of the association with oppositely charged surfactant, until they reach the charge neutralization point, at $Z = 1$. Typically here the system reaches two distinct phases and neutral, water-insoluble complexes occur [16, 151, 171]. After passing the charge neutralization point, in surfactant excess regime at $Z < 1$, complexes become increasingly charged since extra negative charges are

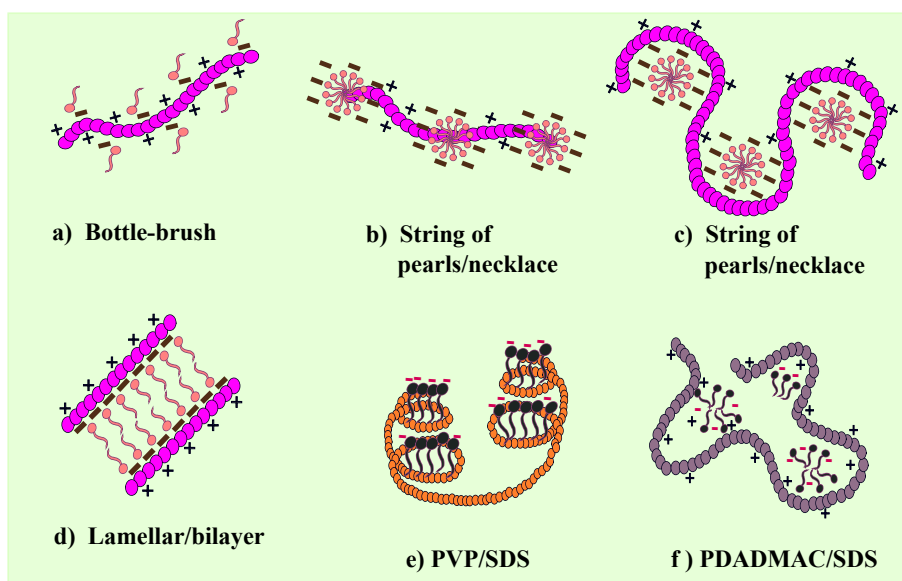


Figure 1.3: Possible PESCs structures: a) polyelectrolyte decorate with few surfactant molecules; b) pearl-necklace structure where hydrophobic interactions predominate; c) pearl-necklace structure where the PE wraps around micelles; d) bilayer structure; e) PVP/SDS interaction where hydrophobic interaction predominate [53]; f) PDADMAC/SDS interaction where electrostatic interaction predominate [53].

provided from the surfactant. The further addition of surfactant is able to redissolve the associated complexes and the system turns in a single phase, exhibiting clear solutions again. For these systems depending on the concentration and chemical nature of polyelectrolytes and surfactants involved, different PE-surfactant interactions and phase behavior can occur. By tuning the surfactant tail length [5, 24, 60, 73, 170, 256, 294, 297, 298] and type of head group [107, 125] as well as charge density [107, 210, 295], hydrophobicity [115, 176], chain conformation [187, 284], molecular weight [55, 59], stiffness of the polyelectrolyte [107, 296] and charges ratio Z , their self-assembly behavior and the resulting supramolecular structures can be modulated.

In the following some examples of different PESCs structures are given.

At high Z values, in PE excess, for oppositely charged polyelectrolyte/surfactant one may have bottle-brush structures, see fig. 1.3 a, where single amphiphilic molecules are attached to the PE chain [55]. Sometimes is not easy to extract the representative structure of the complexes. For the neutral poly(vinylpyrrolidone) (PVP)/ sodium dodecyl sulfate (SDS) mixture, for example, different studies have proposed as a model of interaction a pearl-necklace structure as in fig. 1.3 c [51, 68, 213, 238, 239]. Other groups, in contrast, have suggested a different PE/surfactant interaction resulting in a structure like in fig. 1.3 b [227, 241, 276]. Chatterjee et al. [53] resolved this discrepancy by comparing the PVP/SDS system with the cationic poly(diallyldimethyl ammonium chloride)

(PDADMAC)/SDS ones, analyzing both with photoluminescence (PL) microscopy and atomic force microscopy (AFM). They demonstrated that in presence of PVP, SDS binds to the polyelectrolyte mostly through hydrophobic interactions. With PDADMAC, on the other hand, the complexation comes through electrostatic interactions between the negatively charged SDS headgroups and positively charged nitrogen centers of the polymer. A representative cartoon for PVP/SDS self-assembly is shown in fig. 1.3 e and for PDADMAC/SDS in fig. 1.3 f.

Goswami et al. [106] illustrated with molecular dynamics (MD) simulations the effect of the PE backbone charge density on the complexation of oppositely charged PE/surfactant complexes. In a different work Liu et al. [176] used MD to demonstrate that for hydrophilic PE, with increasing amount of adsorbed surfactant, the structure evolves from bottle-brush structure, through necklace, then to rod-like micelle, with a tendency for flexible polyelectrolytes to wrap around the micelle surface. Another study of the effect of the polymer flexibility has been done on complexes of poly(sodium styrenesulfonate) (PSSNa)/C_n trimethylammonium bromide (TAB) (n = 14-18), for which a bilayer structure as in fig. 1.3 d has been proposed [296, 299], dictated by the low flexibility of the polymer and cylindrical surfactant aggregates. The PESC's morphology is thus a direct consequence of the system's parameters since many variables can dictate the aggregation. This thesis project focuses on mixtures of alkyl surfactants with a biopolyelectrolyte: an ionically modified cellulose PE named JR 400.

1.3 The Cellulose-Based Polyelectrolyte JR 400

As stated above, the field of biomaterials has grown significantly in the past decade [13, 131, 134, 149, 190] due to discoveries in tissue engineering [121], regenerative medicine [181], biotechnology, etc., but also because they are eco-friendly being extracted from biological resources or manufactured by using the green technology [240]. In this work the biopolyelectrolyte used is a cationic, cellulose-based polymer named JR 400. Among all the natural polymers, cellulose is of very high importance as it is an easily accessible, abundant [21] and biodegradable material [242, 291]. It is a linear polymer [120] composed of D-anhydroglucopyranose units (AGUs) [69, 120] which are linked by β 1-4 glycosidic bonds [152] where each ring contains three hydroxyl groups, one primary and two secondary, see fig. 1.4. Cellulose is insoluble in water [184] and in many organic solvents [184]. In order to be used in various applications, cellulose materials often require functionalization. The chemical modification consists in apporating new functional groups on the cellulose chain by reacting hydroxyl groups [1, 152], for example with alkylating agents, which can enrich its functionality and thus expand application range. Most

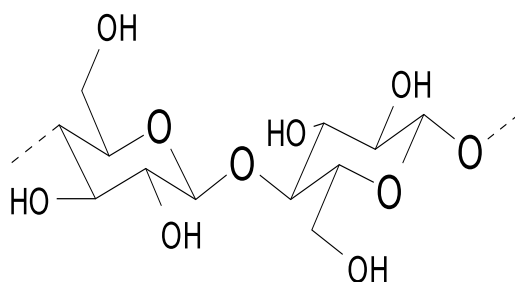


Figure 1.4: chemical structure of cellulose

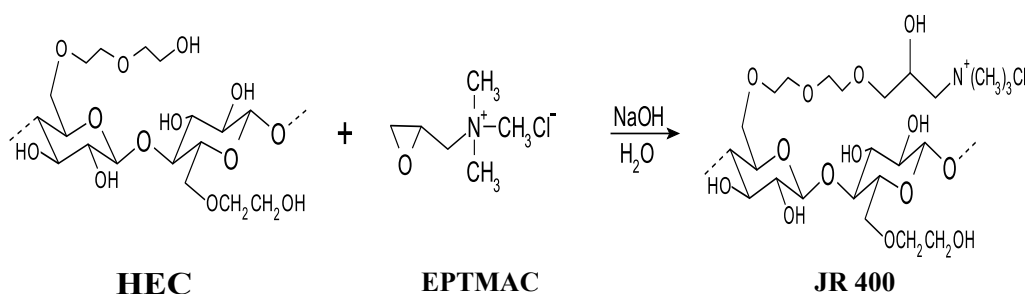


Figure 1.5: Chemical reaction of the hydroxyethyl cellulose (HEC) with EPTMAC to produce JR 400.

of the cellulose derivatives are products of esterification and etherification of hydroxyl groups [120]. The average number of hydroxyl groups substituted per monomeric unit defines the degree of substitution (DS), ranging from 0 up to a maximum of 3. Between the different cellulose based polymer, hydroxyethylcellulose (HEC) is well-known and widely used. Its relatively good water solubility, biodegradability, hydrophilicity, antibacterial properties [31] and good viscosifying properties make it extremely useful as a viscosifier for many different applications [78]. HEC is produced by ethoxylation of the cellulose, adding ethylene oxide (EO) chains. The length of the EO chain impacts the hydrophilicity of the polymer [298]. Moreover, the hydroxyl groups of HEC present in the side chains can be modified to enhance the properties of HEC. Cationically modified HEC (cat-HEC), for example, are widely applied in different fields, such as the production of fibers or paper, adsorbents, in the cosmetics industry like conditioner in shampoos [220], and as antibacterial agents [26, 50]. Furthermore, the interactions between cat-HEC polyelectrolytes and different anionic surfactants have been extensively studied in recent years [167, 201, 283]. JR 400 is a cat-HEC obtained from an etherification reaction between the alkali activated hydroxyl group of HEC and 2,3-epoxypropyl trimethylammonium chloride (EPTMAC) through the reaction shown in fig. 1.5. It has a molecular weight of about 500000 g/mol [76] with the cationic group on 27 % of the glucose unit [173], resulting in 1000 g of PE per mol of positive charges [261]. It is a large, bulky and relatively stiff polyelectrolyte with a persistence length of the free PE segments of $L_{PE} \approx 6$ nm [73, 125]. The mean contour

length between charges is 2 nm [205, 218] and they are located on the chains on every fourth glucose unit in the PE backbone on average. However, also other cat-HEC PEs are available, like JR 125, JR 30M, LR 400, LR 30M, HR 400 where H, J and L indicates the degree of substitution (DS), with $H > J > L$ and numbers are molecular weight index [102, 257].

1.4 PESCs as Rheology Modifiers

The rheological behavior of a polyelectrolyte solution can be tuned by the addition of surfactant, finding use in many industrial products such as pharmaceuticals, cosmetics or in some processes like extraction of petroleum and processing of minerals [59]. Of particular interest are systems containing oppositely charged PE and surfactants [24, 113, 197, 262–264, 278]. As stated in section 1.1 their binding process involves both electrostatic and hydrophobic interactions [15, 52], exhibiting a synergistic effect much more complex than that between non-oppositely charged systems. Goddard and co-workers studied through surface tension measurements the interaction of JR 400 with a non-ionic and ionic surfactant, namely respectively Tergitol 15-S-9 (a linear surfactant that is a secondary ethoxylated alcohol) and SDS [98, 103, 172]. Experiments have shown that JR 400 had no significant effect on the surface tension of Tergitol, suggesting a minimal interaction between the two components. In contrast, for JR 400/SDS, the surface tension values were dramatically lower than that of the pure surfactant solution, even for SDS concentrations two decades below the CMC.

Apart from their industrial relevance, mixtures of oppositely charged polyelectrolytes and surfactants attract considerable scientific interest due to their use to control the rheological behavior of aqueous solutions [124, 144, 197, 206, 265, 284]. Depending on the conditions, the addition of oppositely charged surfactant to a PE solution can produce two different effects: a decrease or an increase of the solution viscosity.

Plucktaveesak et al. [210] reported that in mixtures of poly-acrylic acid (PAA) partially neutralized with NaOH and dodecyl trimethylammonium bromide (C_{12} TAB), the solution viscosity is lowered after the addition of the oppositely charged surfactant. In these solutions the effect of the surfactant is to induce a partial collapse of the polymer, and the loss of part of its effective chain length [110, 162, 210].

Differently, solutions of a hydrophobically modified polymers and surfactants [94, 132, 143, 254, 261], as well as systems containing oppositely charged polysaccharide-based biopolyelectrolytes and surfactants [97, 123–126, 167, 265], exhibit a large increase in solution viscosity. Among these latter systems, mixtures of cationic cellulose ether derivatives (cat-HEC) and oppositely charged amphiphilic molecules have been extensively stud-

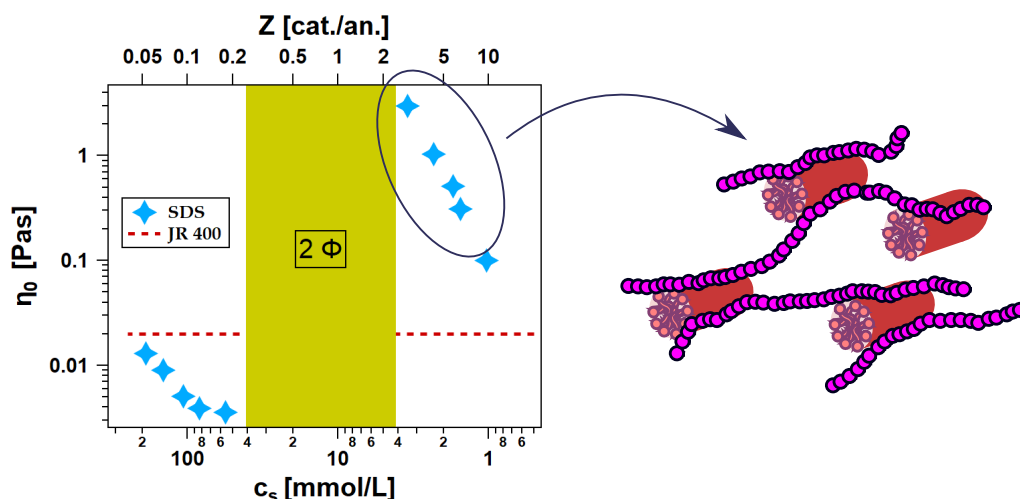


Figure 1.6: On the left, zero shear viscosity of JR 400, SDS/JR 400 mixture as function of Z (top) and surfactant concentration (bottom). On the PE rich side a strong increase of the viscosity is registered, while in surfactant excess is reduced even below the value of the pure PE solution. Right, schematic representation of mixed rod-like aggregates interconnecting PE chains.

ied [73, 74, 109, 124–126, 183, 245, 283] ever since Goddard reported the increase in viscosity upon addition of an anionic surfactant to JR 400 [100].

In the following an overview on mixtures of JR 400 and oppositely charged surfactants is given.

1.4.1 Mixtures of JR 400 and Oppositely Charged Surfactants

As stated above, mixtures of JR 400 and oppositely charged surfactants have been widely studied in literature, since the 1970's [14, 97, 101, 104, 167, 167, 219, 282]. In particular, even if the enhancement of viscosity in mixtures of JR 400/anionic surfactant was already attributed to the presence of cross-links in solution, recent investigation with neutron experiments on these mixtures shed light on the relation between mesoscopic structure and macroscopic viscosity [123–126, 128]. In general, for semi-dilute solution at 1 wt% JR 400 a progressive increase of solution viscosity occurs upon addition of an oppositely charged surfactant. Overall, approaching the phase boundary, on PE rich side, a viscosity enhancement by almost three orders of magnitude can be observed, see fig. 1.6. Typical flow curves of these mixtures show that the viscosity follows a Newtonian behavior at low shear rates, while at high shear rates a shear thinning (that is, deviating from Newtonian behavior the viscosity decreases under shear strain) is observed. Additionally oscillatory shear measurements reveal that these systems are viscoelastic. All the mixtures behave as

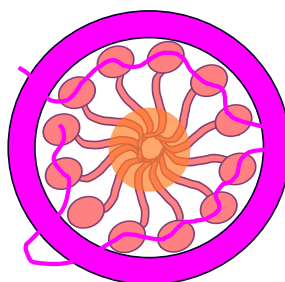


Figure 1.7: Cross section of the aggregates described with a core made of only surfactant, a mixed layer with PE and surfactant and an outer shell made of only PE [125].

viscous fluids at low frequencies, ($G'' > G'$), while the elastic response dominates, ($G' > G''$), after the crossover frequency is reached, (where $G' = G''$). Reaching the two phase region, the relaxation time τ_{cross} , i.e., the inverse of the frequency at the crossover, increases and the critical shear rate shifts towards smaller shear rates [55, 124, 126]. These findings suggest that a probably stronger network is present as more surfactant is added. An efficient investigation on these viscoelastic structures has been achieved mostly with small angle neutron (SANS) measurements. From experiments on JR 400/ SDS and JR 400/ sodium dodecyl benzene sulfonate (SDBS) [123–125, 128] it can be deduced that the increase in viscosity is due to the presence of mixed rod-like aggregates. Furthermore, using the contrast matching technique (that is, by selectively labeling a component with deuterium, see section 2.3.1) it has been possible to better understand the mesoscopic structure of the aggregates, which was described with a core shell model. According to this model, rods have a small core consisting of only surfactant, a middle layer where PE and surfactant are mixed and an outer shell of only PE [125], see fig. 1.7. It has also been seen that the amount of JR 400 incorporated in the aggregates increases with the increase of the surfactant concentration, i.e., reducing Z and it conserved in the structure. An important point that has been clarified is that the viscosity enhancement is not related to a growth in length of the aggregates, but rather to the presence of cross-links [123, 125], that is the aggregates interconnect different PE chains, see again fig. 1.6. Hoffmann et al. [125] have demonstrated that for both JR 400/SDS and JR 400/SDBS mixtures the length of the aggregates is rather constant and independent of Z . These findings explain the higher viscosity of JR 400/SDBS mixtures since it has been found that for these solutions roughly 5 PE chains are bounded along the aggregates versus roughly 3 PE chains for JR 400/SDS. However, a key parameter for the viscosity increase is the PE concentration in solution. For mixtures at 0.33 wt% of JR 400, below the overlap concentration, the number of PE chain per aggregate is much lower, about 1 single chain. This results in a less viscosity enhancement when reaching the phase boundary.

Once in surfactant excess regime, i.e., at low Z values, a strong decrease in viscosity oc-

curs, equaling the pure PE solution. For JR 400/SDS, SANS analysis showed that no longer rod-like aggregates are present, but spherical structures. Being in surfactant excess, the amount of PE incorporated in them was found to be much lower than that in the rod-like aggregates. The difference in the amount of PE involved in the structures is the key to explain the transition in shape (from rod-like aggregates to spherical structures) moving from PE excess to surfactant excess. The rodlike shape of the aggregate is strongly favoured by both the amount and the arrangement of JR 400 involved since it enters in the middle layer of the structure. This means that on the one hand it reduces the head group area because it reduces the charges on the surface. On the other hand it increases the volume of the surfactant chains since it penetrates in the aggregate. Considering a non-negligible amount of mixed PE, this results in an increase of the packing parameter p , promoting a rod-like shape [136] (with $p = v/a_0l$ where l and v are the effective maximum length and volume of the hydrophobic tail, respectively, and a_0 is the effective cross-sectional area of the hydrophilic headgroup [185]). Differently, at low Z values the PE incorporated in the spherical structures is so small that it does not sufficiently change the packing parameter to induce a shape transition. Combining neutron spin-echo (NSE) and fluorescence correlation spectroscopy (FCS), Hoffmann et al. [128] found that the spherical aggregates are bound to the PE chains, since their diffusion is lower than that of micelles of the same size.

1.5 Aim of the Thesis

Although an earlier study already resolved the structural details of the PESCs formed by one particular PE/surfactant combination (JR 400 and SDS), the influence of the surfactant chemistry on the mechanisms responsible for the remarkable rheological behavior has remained unexplored. However, such fundamental insights are required for the rational design of PESCs with desired properties.

This thesis was therefore aimed at a systematic investigation of the role of the surfactants' chemical characteristics for the mesoscopic structure of PESCs and the resulting rheological properties, with a focus on the underlying mechanisms. The conducted research can be separated into four parts:

1. Before varying the surfactant characteristics, a first study has been made to investigate the mechanism responsible of the shear thinning behavior of PESC solutions. Specifically, JR 400/SDS mixtures have been investigated through rheo-SANS measurements. The rheo-SANS method employs SANS while simultaneously imposing a mechanical stress field, in order to measure flow-induced structures in fluids [84]. This technique offers the unique opportunity to develop a qualitative and quantitative understanding of the relationships between the PESCs mesoscopic structure

and macroscopic flow properties. The measurements revealed that the capability of the aggregates to orientate under an imposed stress plays an important role for the solution rheological behavior.

This study is described in detail in chapter 4.

2. The next step was aimed at elucidating the influence of the surfactant tail length on the viscosity of oppositely charged PE/surfactant mixtures. Although in the literature there are some studies on the role of the surfactant tail on the PESCs flow behavior [5, 24, 256, 294, 297], its influence on the aggregate mesostructure and their dynamics is still unknown. To elucidate this point, two different mixtures were analyzed: JR 400/sodium octyl sulphate (SOS) and JR 400/sodium tetradecyl sulphate (STS). SOS and STS differ for the length of their tails: the former has 8 carbon atoms while the latter 14. Together with existing data on SDS with C_{12} tails [125], this study offered a robust analysis on the effect of the surfactant tail in determining PESCs' structures.

Additional information on the PESCs dynamics was obtained with NSE measurements. In the end, experimental results were compared with molecular dynamics (MD) simulations involving stretched polypeptides as generic mimics of JR 400.

This study is described in detail in chapter 5.

3. In the following step, the effect of the charge of the surfactant head group has been studied. For this purpose, mixtures of JR 400 with sodium dodecyl phosphate (SDP) have been investigated. SDP has the advantages that it can exist in the monoanionic and dianionic species depending on the pH, enabling to explore the charge effect for fixed components in solution. In presence of the double-charged form, SDP^{2-} in alkaline solutions, mixtures are not shear thinning and the viscosity does not increase substantially while the mono-charged form, SDP^- in neutral solutions, samples show viscoelastic properties with an enhancement of the viscosity when approaching the to the two phases region, in PE excess. Macroscopically, the charge has the same effect of the surfactant tail length. The flow behavior was again investigated with both oscillatory and steady shear measurements. SANS and NSE measurements were used to investigate the mesostructures in solution, to reveal the difference induced by the surfactant head group charge. Results confirm that as for JR 400/STS, the viscosity behavior of JR 400/ SDP^- can be inferred to the presence of the mixed rod-like aggregates.

This study is described in detail in chapter 6.

4. In the end, in order to study the mechanical stability of mixed rod-like aggregates, constant-force pulling (CFP) MD simulations were performed with two positively

charged polyelectrolyte strands held together by adsorbed SOS or STS molecules. As already motivated in point 2 above, generic mimics of JR 400 in the form of polypeptides were again used for this purpose and two extreme relative configurations were investigated: parallel and orthogonal polyelectrolytes. The results are compared with the experimental observation and qualitative agreement is found.

This study is described in detail in chapter 7.

Parts 1-3 have been published or submitted for publication, while part 4 is to be published when the study is completed.

The thesis is organized as follows:

- chapter 2: this chapter introduces the theoretical principles of the different techniques used to characterize the solutions studied. Therefore, theoretical principles of Rheology, Dynamic Light Scattering (DLS), SANS, NSE and MD simulations are provided;
- chapter 3: this chapter consists of two sections. The first section provides both the specifications of the materials employed and the procedure with which they were used to prepare the analyzed solutions. The second section lists the technical parameters (setting) of the various experiments carried out in this thesis project;
- chapter 4, chapter 5, chapter 6: these chapters elaborate on what was introduced in points 1, 2 and 3 (see above) respectively. Content and text in these chapters are in the respective manuscripts;
- chapter 7: this chapter develops what was introduced in point 4, (see above);
- chapter 8: this is the last chapter of this thesis. In the first part, it summarizes the key points of this project, providing a general overview of the work carried out and underlining the new knowledge made on the mechanisms behind the unique rheological behavior of PESC solutions. In the second part ideas are provided for possible future work on this topic.

Chapter 2

Theoretical Background

2.1 Dynamic Light Scattering (DLS)

2.1.1 Principle

In a typical light-scattering experiment, the sample is exposed to a monochromatic wave of light. The sample is usually a solution containing particles and light scatters in all directions as a function of their size and shape. Dynamic light scattering (DLS), is a useful technique [34] that can be used to determine the size-distribution profile of small particles in suspension, with the size range of analysis ranging from a few nanometers to a few micrometers [281]. The technique measures the time dependence of the intensity of scattered light caused due to the Brownian motion of particles in solution. Brownian motion is the random particles movement due to the stochastic collisions with the solvent molecules and it is strongly dependent on the particles size and on the temperature. The knowledge of the temperature is very important since it influences the viscosity of the liquid [10] and it affects the diffusion coefficient, D , as expressed in the Stokes Einstein equation [214]:

$$D = \frac{k_B T}{6\pi\mu R_h} \quad (2.1.1)$$

with μ the viscosity of the medium, R_h the hydrodynamic radius and k_B the Boltzmann constant.

Monitoring the Brownian motion over the time, it is possible to get information on the par-

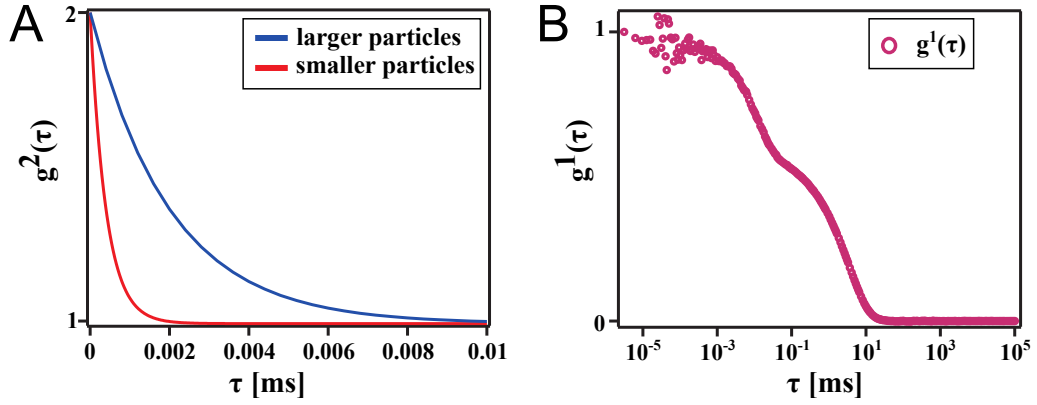


Figure 2.1: (A) Autocorrelation function $g^{(2)}$ from suspensions of different size particles. (B) example of the field autocorrelation function of PE solution at $\theta = 110^\circ$.

ticles size since larger particles diffuse slowly compared to smaller ones [116]. In a DLS experiment, the time-dependent fluctuations in the intensity of scattered light are analyzed using an autocorrelator which determines the autocorrelation function of the signal $G^{(2)}$. This function can be expressed as an integral over the product of intensities at time t and delayed time $(t + \tau)$ [34]:

$$G^2(\tau) = \langle I(t)I(t + \tau) \rangle \quad (2.1.2)$$

which can be normalized on the incident intensity to obtain:

$$g^2(\tau) = \frac{\langle I(t)I(t + \tau) \rangle}{\langle I(t) \rangle^2} \quad (2.1.3)$$

As indicated in eq. (2.1.3) when the delay time τ is zero, the signal is perfectly correlated, while when τ is infinity, it is perfectly uncorrelated. The rate of decay of this function follows a characteristic time scale depending on the size of the scatterers, see fig. 2.1 A.

However, the correlated particle movements is described by the electric field correlation function $g^{(1)}$ which can be coupled to $g^{(2)}$ by the Siegert relation [34]:

$$g^{(2)} = 1 + B|g^{(1)}|^2 \quad (2.1.4)$$

where B is the coherence factor that depends on detector area and optical alignment. For a monodisperse sample $g^{(1)}$ decays as an exponential with decay length Γ :

$$g^{(1)} = \exp(-\Gamma\tau) \quad (2.1.5)$$

The decay constant Γ is related to the diffusion behavior of particles through:

$$\Gamma = -DQ^2 \quad (2.1.6)$$

where the magnitude of the scattering vector Q is related to the scattering angle θ by $Q = (4\pi n/\lambda) \sin(\theta/2)$, with n being the refractive index of the medium, λ being the wavelength in vacuo and θ being the scattering angle. In the end, from D and using the Stokes–Einstein [214] equation, see eq. (2.1.1) it is possible to obtain the hydrodynamic radius R_h , which can be defined as the radius of a hypothetical sphere that diffuses at the same rate as the particle under investigation.

2.1.2 Semi-Dilute Polymer Solutions

In this project DLS measurements have been carried out on semi-dilute polymer solutions for which the mode coupling theory (MCT) has been successfully applied to describe the dynamics [28, 235]. According to the approach taken by Ngai and co-workers [195], the correlation function of semi-dilute solutions of entangled polymers can be described with a combination of an exponential function at short times and a stretched exponential at long times, see fig. 2.1 B,

$$g^{(1)}(t) = A_{\text{fast}} \exp(-t/\tau_{\text{fast}}) + A_{\text{slow}} \exp(-(t/\tau_{\text{slow}})^\beta) \quad (2.1.7)$$

The decay at short times described by τ_{fast} is related to the collective motion of single chains with the diffusion coefficient $D = (\tau_{\text{fast}} Q^2)^{-1}$ while the slow mode, described by τ_{slow} , accounts for the dynamics of larger cluster. The value of the stretching exponent, β , is related to the coupling parameter n through $\beta = 1 - n$.

The theory assumes that the system is composed of "basic units" whose interaction is sanctioned by a critical time t_{crit} . For $t \leq t_{\text{crit}}$ the base units diffuse independently, that is the dynamics is not perturbed by the formation of clusters. In this time window the correlation function is described by a single exponential decay, so that

$$g^{(1)}(t) = \exp(-t/\tau_{\text{fast}}) \quad (2.1.8)$$

For longer times, $t > t_{\text{crit}}$ the correlation function is characterized by a second slow stretched exponential decay, see eq. (2.1.7). For $t = t_{\text{crit}}$ an important relationship is given:

$$\tau_{\text{slow}}(Q) = (t_{\text{crit}}^{-n} \tau_{\text{fast}}(Q))^{1/(1-n)} \quad (2.1.9)$$

where the decay time of the slow mode is linked to τ_{fast} , t_{crit} and n . The coupling parameter, n , depends on the intermolecular interaction whose value is in the range $0 \leq n < 1$ and it increases (or β decreases) at the increasing of the strength of the interaction between the basic units. While the fast time shows diffusive Q^{-2} behavior, the Q dependence of τ_{slow} is

proportional to $Q^{-2/(1-\eta)}$, as follows from inserting the Q^{-2} dependence into the expression for τ_{slow} .

2.2 Rheology

2.2.1 Principles

Rheology is the study of the deformation and flow of material under an applied force. In this paragraph a brief overview on the basic aspects of flow deformation is given to give a basis to interpretate rheological experiments. To start, is given a little reminder about some definitions regarding polymer solutions, on which rheology measurements are done. According to the scaling theory [71] polymer solutions can be divided into three different regions: the dilute, semi-dilute, and concentrated solutions. A generic solution can be thought as stacking of imaginary spheres where each sphere, containing a single polymer chain, has a radius equal to the radius of gyration of each chain, R_g . At low concentration, c , these spheres are separated from each other. With the increasing in c they start to be closer until a critical concentration is reached, the so-called overlap concentration, c^* , where the whole volume of the solution is packed with these spheres. For convenience, it is considered that at c^* the total volume of the system is occupied by the volume of the polymer coils [105], so that:

$$c^* \approx \frac{M}{N_A} \frac{3}{4\pi R_g^3} \quad (2.2.1)$$

where M is the polymer molecular weight and N_A is Avogadro number. However, c^* can be also experimentally determined since its values is given by the slope change in viscosity vs concentration plot [144]. Figure 2.2 illustrates three different solution scenarios. At $c < c^*$ the solution is called dilute. Here polymer chains do not interact, behaving more or less independently since their interaction is primarily with the solvent molecules. At $c = c^*$ the mobility of the polymer chain starts to be reduced and at $c > c^*$ it is drastically reduced since chains are overlapped; the solution is now in the semi-dilute regime [6, 105]. Moreover, the overlapped polymer chains can also form entanglements, once the critical entanglement concentration, c_e is reached. Hence, for $c^* < c < c_e$ semi-dilute solutions are in the unentangled regime, switching to the entangled regime for $c > c_e$ [62]. With the further increasing of the concentration, the upper limit of the semi-dilute regime, c^{**} , is reached. It represents the onset of the concentrated regime where there are few fluctuations and the local concentration can be taken as the average over the system.

In this project the polymer solution are in the semi-dilute regime.

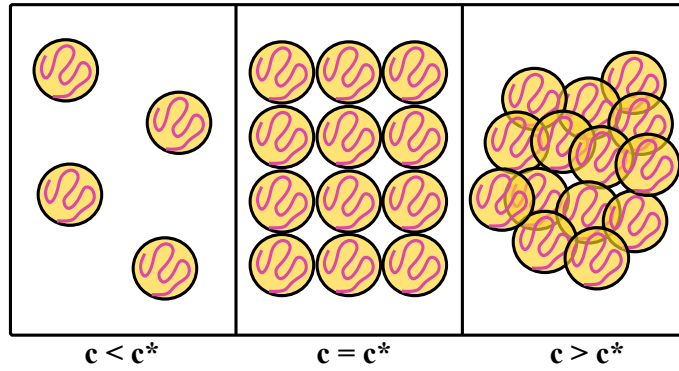


Figure 2.2: Illustration of different polymer solution regimes: at $c < c^*$ dilute solution; at $c = c^*$ solution at overlap concentration; at $c > c^*$ semi-dilute solution.

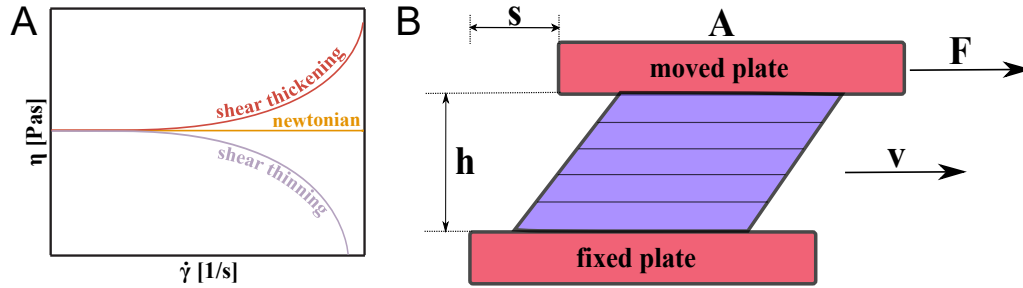


Figure 2.3: (A) Viscosity of newtonian, shear thinning and shear thickening fluids as function of shear rate. (B) Two-plates model to define rheological parameters.

At this point, let us consider the rheological parameters needed for a scientific description of flow behavior, with the help of the two-plates model shown in fig. 2.3 B. The model has a fixed lower plate, an upper plate that can be moved parallel to the lower plate and a volume of sample in the middle, ideally illustrated as individual planar fluid layers. The sample is going under deformation due to a force F applied to the upper plate which has an area A . The resulting important parameters are the shear stress, τ , shear strain, γ , and the shear rate, $\dot{\gamma}$, given by:

$$\tau = \frac{F}{A} \quad (2.2.2)$$

$$\gamma = \frac{s}{h} \quad (2.2.3)$$

$$\dot{\gamma} = \frac{d\gamma}{dt} \quad (2.2.4)$$

The meaning of $\dot{\gamma}$ is that it quantifies the rate at which fluid layers move past each other. Shear stress and shear strain are related by the viscosity η which represents the resistance of a material to flow:

$$\tau = \eta \dot{\gamma} \quad (2.2.5)$$

Equation (2.2.5), known as Newton's law, assumes that η is independent of $\dot{\gamma}$ and the law is linear. Liquids, whose viscosity remains constant with changing shear rate (at constant Temperature and Pressure) are called Newtonian liquid. However, not always the Newtonian postulate is respected and if the viscosity depends on the shear rate the fluids are called non Newtonian. In fig. 2.3 A two different types of non Newtonian flow behavior are shown: shear thinning and shear thickening. In shear thinning fluids, also known as pseudo-plastic, viscosity decreases as the shear rate increases while for shear thickening η increases with increasing shear rate.

In this thesis viscosity measurements are expressed as zero shear viscosity, η_0 . It refers to the viscosity plateau prior to the onset of shear thinning describing rheological response at low shear rate. The zero shear viscosity is a limiting value that cannot be measured directly but it needs to be estimated by extrapolation.

One important characteristics of polymeric materials is their viscoelastic behavior, that is solutions exhibit both viscous and elastic character. Elasticity is the tendency of solid materials to recover their original shape after removing forces applied on them, resulting in τ directly proportional to the strain γ :

$$\tau = G\gamma \quad (2.2.6)$$

with G as constant, known as shear modulus that indicates the material response to shearing strains; the higher the G value, the stiffer the material.

Viscosity, as mentioned above, is a measure of a fluid's resistance to flow. Polymer solutions can exhibit all intermediate range of properties between an elastic solid and a viscous liquid. Viscoelastic materials due to the viscosity factor have mechanical properties dependent on time. Normally the analysis of these viscoelastic systems is performed with oscillatory measurements. A sine wave strain is applied to the sample and normally the amplitude of the sinusoidal signal is kept constant while the frequency is the variable. Moreover, the strain amplitude is chosen in the limit of the linear viscoelastic region (LVE) to avoid that the measurements could destroy the structure of the sample. An oscillatory shear strain with angular frequency ω expressed as:

$$\gamma = \gamma_0 \sin \omega t \quad (2.2.7)$$

is applied. The stress response, due to the viscoelastic nature of the material, is also a sinusoidal but out of phase relative to the strain, expressed as:

$$\tau = \tau_0 \sin(\omega t + \delta) \quad (2.2.8)$$

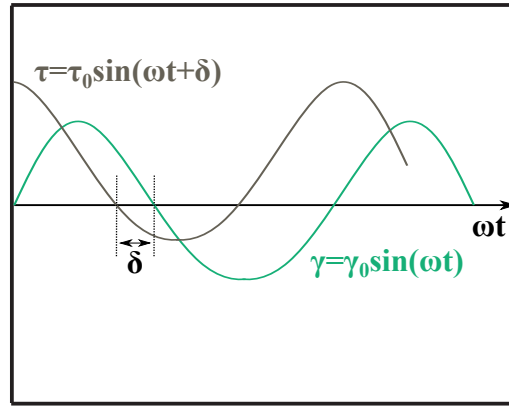


Figure 2.4: Two-plates model to define rheological parameters

with δ the phase angles which lies between 0° and 90° , see fig. 2.4. For a purely elastic material, the stress response is always in phase with the strain, i.e., $\delta=0^\circ$. For a purely viscous material, there is a 90° phase difference. The eq. (2.2.8) can be formulated as follows:

$$\tau = (\tau_0 \cos \delta) \sin \omega t + (\tau_0 \sin \delta) \cos \omega t \quad (2.2.9)$$

where the stress has two components; $(\tau_0 \cos \delta)$ in phase with the strain and $(\tau_0 \sin \delta)$ of 90° out of the phase. Introducing

$$G' = \frac{\tau_0}{\gamma_0} \cos \delta \quad (2.2.10)$$

$$G'' = \frac{\tau_0}{\gamma_0} \sin \delta \quad (2.2.11)$$

eq. (2.2.9) can be rewrite as:

$$\tau = \gamma_0 [G' \sin \omega t + G'' \cos \omega t] \quad (2.2.12)$$

Oscillatory measurements allow the determination of both the storage modulus G' and loss modulus G'' where the former is related to the elastic response of the solution, while the latter to the viscous. A typical behavior shows that at lower frequencies $G'' > G'$ so that viscous response predominate, while at high frequencies $G' > G''$. The point of crossover between G' and G'' defines a very important structural parameter, the relaxation time, τ_{cross} , which is strictly related to the internal structure of the material. With the increasing of frequencies G' continues to rise and it usually reach a plateau. The value at the plateau, known as the plateau modulus G_0 , is an important property in understanding the dynamics of the solutions, since it is related to the number of effective cross-links per unit volume [144] revealing important information about the internal structure. For this reason, as already stated above, it is important to work in the LVE region since the

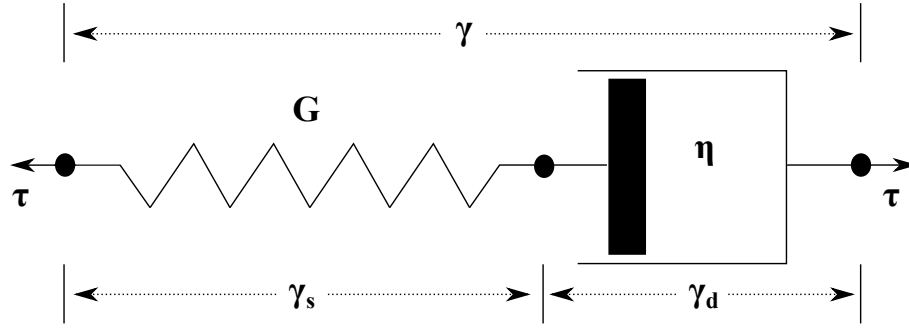


Figure 2.5: Rheological representation of the Maxwell model.

measured G' and G'' do not vary with the strain and they are intrinsic properties of the internal material organization. To describe a viscoelastic behavior, one can build a model by combining at least two components, one to describe the elastic contribution represented by a spring and the other to describe the viscous behavior, represented by a dash-pot. One of the simpler idealization of the viscoelastic parameters of a material is the Maxwell model [85], which consists of a spring connected in series with a dash-pot as shown in fig. 2.5. In the Maxwell model, the stress is the same in both elements, resulting:

$$\tau = \tau_s = \tau_d \quad (2.2.13)$$

where τ_s and τ_d represent the stress in the spring and dash-pot respectively. Consequently, the resulting total deformation of the viscoelastic material is given by the sum of the individual deformations of spring and dash-pot:

$$\gamma = \gamma_s + \gamma_d \quad (2.2.14)$$

with γ_s and γ_d the strain in the spring and in dash-pot. Considering that the stress–strain relations in spring and dash-pot can be written as:

$$\gamma = \frac{1}{G}\tau \quad (2.2.15)$$

$$\dot{\gamma} = \frac{1}{\eta}\tau \quad (2.2.16)$$

it is possible to differentiate eq. (2.2.14) with respect to time and express the partial strain rates $\dot{\gamma}_s$ and $\dot{\gamma}_d$ using eq. (2.2.15) and eq. (2.2.16), where the partial stresses τ_s and τ_d are replaced by τ according to eq. (2.2.13). To this end, the Maxwell equation comes out:

$$\dot{\gamma}(t) = \frac{\dot{\tau}(t)}{G} + \frac{\tau(t)}{\eta} \quad (2.2.17)$$

where γ and τ are functions of time, while G and η are considered as fixed model param-

eters.

2.3 Small Angle Neutron Scattering (SANS)

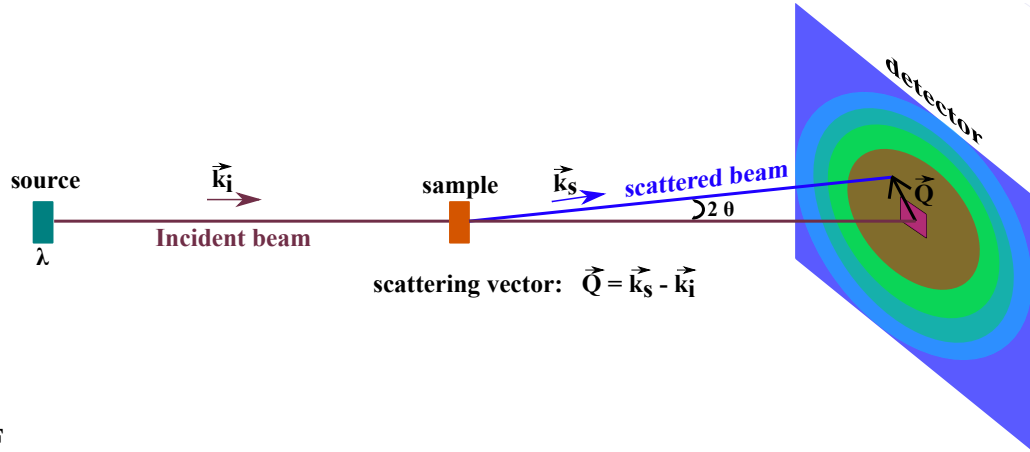
2.3.1 Principle

Small Angle Neutron Scattering (SANS) is a powerful technique to extract global structural parameters and shape information from materials with a typical size of the order 1 nm to over 100 nm. Thereby, it has been applied to a wide range of fields, from macro structures like polymers to biological molecules, molecular self-assemblies, magnetic systems, etc. Being a scattering technique the information gained from the measurements are statistically averaged over the entire sample. SANS is a powerful technique since neutrons' unique specificities, like:

- the charge neutrality and weak energy make them a powerful non destructive probe for the samples;
- their interaction with the matter occurs with the nuclei of the atoms. The important parameter for describing this interaction is the scattering length density, *SLD*, which depends on the isotope of the element. Replacing some hydrogen atoms of a molecule with deuterium atoms, in fact, the *SLD* results modified so that the techniques allows one to investigate selected chemical components via isotopic labeling. For this purpose, all the analyzed mixtures were prepared using D₂O as solvent instead of H₂O to create a better *SLD* contrast between the solvent and the organic materials;
- their magnetic moment allows to determine the range and degree of order in magnetic compounds;
- they are weakly absorbed by matter.

In a typical experiment, the sample is irradiated by a monochromatic neutron beam and the scattered neutrons are detected by a detector, see fig. 2.6. Usually the scattered intensity $I(Q)$ is expressed as function of the magnitude of the scattering vector \vec{Q} , given by:

$$Q = \frac{4\pi}{\lambda} \sin\theta \quad (2.3.1)$$



F

Figure 2.6: Schematic representation of a SANS experiment with the representation of the vector \vec{Q} .

with λ the wavelength of the incident radiation and θ the scattering angle. Introducing eq. (2.3.1) in the Bragg law, it gives:

$$Q = \frac{2\pi}{d} \quad (2.3.2)$$

The measured scattering intensity for 1N monodisperse particles of volume V_p is given by:

$$I(Q) = \phi V_p (\Delta SLD)^2 P(Q) S(Q) + I_{\text{bkg}} \quad (2.3.3)$$

where ϕ is the volume fraction of the particles in solution, $\Delta SLD = SLD_p - SLD_m$ is the scattering length density difference between the scattering particle and the solvent medium, $P(Q)$ the particle form factor, $S(Q)$ the particle structure factor and I_{bkg} the incoherent background which is subtracted in SANS measurements. The particle number density 1N is coupled to the volume fraction ϕ and the particle volume by $^1N = \phi/V_p$. The contrast term $(\Delta SLD)^2$ is a prefactor of the scattered intensity where the values of SLD are a summation of the coherent neutron scattering lengths of the constitutive atoms of the scatterer divided by the occupied volume. The form factor $P(Q)$ comes from intra-particle scattering and it describes the shape of the objects in solution. For concentrated system the intensity shows the structure factor $S(Q)$ which accounts for inter-particle scattering, probing the spatial correlations between objects. Considering an ensemble of monodisperse, non-interacting particles, the SANS signal is generally given as:

$$I(Q) = ^1N P(Q) + I_{\text{bkg}} \quad (2.3.4)$$

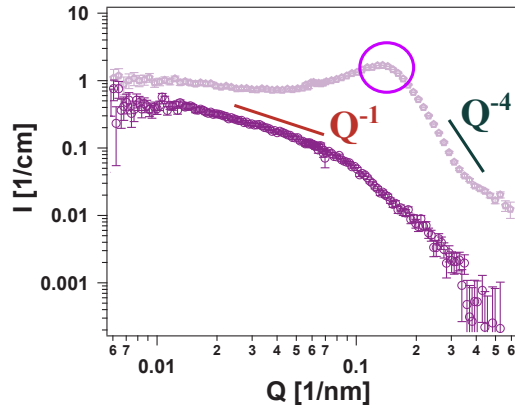


Figure 2.7: Different scattering pattern from different particle shape: cylindrical objects show $I(Q) \sim Q^{-1}$ dependence, while spheres $I(Q) \sim Q^{-4}$. Blue circle indicates the Structure Factor peak.

If the sample is polydisperse with regard to the radius, eq. (2.3.4) takes the form

$$I(Q) = {}^1N \int_0^\infty f(R)P(Q, R)dR + I_{\text{bkg}} \quad (2.3.5)$$

where $f(R)$ is the radius distribution and 1N takes the form

$${}^1N = \frac{\phi}{\int_0^\infty f(R)V_p(R)dR}. \quad (2.3.6)$$

Here, we used the normalised lognormal distribution function

$$f(R, R_m, \sigma) = \frac{1}{\sqrt{2\pi}\sigma R} \exp\left(-\frac{\ln(R/R_m)^2}{2\sigma^2}\right) \quad (2.3.7)$$

$$M = R_m \exp\left(\frac{1}{2\sigma^2}\right) \quad (2.3.8)$$

where M is the mean value of the distribution and the standard deviation is given by $\sqrt{\exp(\sigma^2) - 1}R_m \exp(1/2\sigma^2)$, fixed at 10%.

Mono-disperse particles of different shape show a different scattering pattern, as shown in fig. 2.7. In general, for any SANS curve there is a low Q -regime in which $I(Q)$ is independent of Q , called Guinier regime, valid in the limit of $QR_g < 1$, with R_g the radius of gyration of the particles. From Guinier regime it is possible to get a first size information. A very important Q -range is the intermediate Q -regime where the scattered intensity presents an $I(Q) \sim Q^{-\alpha}$ decay where α is related to the shape of the objects in solution. Cylindrical objects (like the mixed rod-like aggregates in PE excess regime) exhibit an intermediate region in which $I(Q)$ scales with Q^{-1} , fig. 2.7. A particular case is that of spheres (like micelles in surfactant excess region of mixtures) where the scattering pat-

tern goes from the Guinier region, defined by $QR_g < 1$, directly to Porod range with a slope of the plot equal to -4, see again fig. 2.7. The Porod region corresponds to a probed range smaller than the scattering objects and it gives information about the local structure. Porod [211] found that for large values of Q the scattering intensity should decay as $I(Q) \sim Q^{-4}$ since the effect of the sharp, smooth interface that separates the particle from its environment. A generalization of the Porod's approach can be expressed to rough or broad interfaces, in which case $I(Q) \sim Q^{(6-D_s)}$, where D_s is the fractal dimension of the surface [280]. In case of a smooth surface or sharp interface, $D_s = 2$ and a Porod slope of -4 is registered. For rough surfaces or broad interfaces $2 < D_s < 3$ and $I(Q)$ will decay with an exponent between -3 and -4 in the surface fractal regime. In particular, the power law is related to the fractal dimension, like: $I(Q) \sim Q^{-1}$ for 1D object, $I(Q) \sim Q^{-2}$ for 2D object, $I(Q) \sim Q^{-4}$ for 3D object. If the object in solution has a defined geometry, its form factor can be expressed with an exact analytical form so that it is possible to easily fit the data with theoretical models representing the shape of the scatterers in the sample. At this point, let's consider both extreme regions of PE-surfactant phase diagram, where different shapes of the objects are registered.

2.3.2 PE Excess Region: Cylindrical Objects

The form factor of randomly oriented cylinders with radius R and length L is given by

$$P_{\text{cyl}}(Q) = \int_0^1 F_{\text{cyl}}(Q, x)^2 dx, \quad (2.3.9)$$

where the integral over x takes into account the orientational average and $F_{\text{cyl}}(Q, x)$ is the scattering amplitude

$$F_{\text{cyl}}(Q, x) = \pi R^2 L \Delta SLD \frac{4J_1(Q, R\sqrt{1-x^2}) \sin(QLx/2)}{Q^2 R \sqrt{1-x^2} Lx} \quad (2.3.10)$$

comprising the first order Bessel function J_1 .

2.3.3 Surfactant Excess Regime: Spherical Objects

The scattering amplitude of a sphere with radius R is given by

$$F_{\text{sph}}(Q, R, \Delta SLD) = \frac{4\pi}{3} R^3 \Delta SLD \left(3 \frac{\sin(QR) - QR \cos(QR)}{(QR)^3} \right) \quad (2.3.11)$$

and the corresponding form factor reads $P_{\text{sph}}(Q, R, \Delta SLD) = F_{\text{sph}}(Q, R, \Delta SLD)^2$.

To describe the interactions between the charged micelles in the surfactant excess for all the systems analyzed, it has been used the structure factor for charged colloids by Baba-Ahmed, Benmouna and Grimson [23].

2.4 Neutron Spin-Echo (NSE) Spectroscopy

2.4.1 Principle

The neutron-spin-echo (NSE) technique was first proposed by Mezei in 1972 [188]. Among neutron scattering spectroscopic techniques, it is the one with the highest energy resolution, decoupling the latter from the monochromaticity of the beam. NSE has a broad range of applications, ranging from the investigation of the the dynamics of glasses, polymer melts, complex fluids and microemulsions to the elementary excitations in superfluid ^4He and to ferromagnets and spin glasses [189]. In particular, it is a powerful technique for studying internal dynamics of macromolecules in solutions because it can simultaneously probe length and time scales comparable to internal motions of macromolecules. In the most common cases, the incoming neutron beam is polarized along the neutrons' velocity direction (z in fig. 2.8). At the beginning of the instrument, a $\pi/2$ flipper rotates the spins direction to be perpendicular to the magnetic field in the coil. The neutron beam travels within the first magnetic field aligned along z and it precesses, with the spin performing a Larmor precession in the xy plane. Before being scattered by the sample, the neutron spin is rotated by 180 degrees around the x -axis by the π flipper. The neutrons are then scattered by the sample and travel through the second magnetic field, equal to that of the first coil. Inside the second coil, the Larmor precession effectively unwinds the neutron spin. Before the analyzer-detector system a second $\pi/2$ flipper rotates the neutron spin onto the yz plane.

If the scattering would be elastic, the neutron in the second field would travel with the same velocity as in the first field. The neutron spin direction at the end of the second coil is the

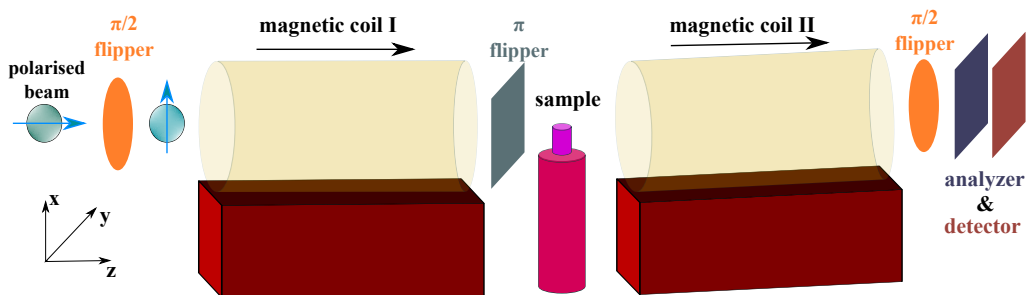


Figure 2.8: Schematic of Neutron spin echo experimental setup.

same as the one at the beginning of the first coil (which is along the x direction), since the fields and the lengths of two coils are equal. The polarization of the beam revealed by the detector, in this condition, would be the same as before the first field and an *Echo* signal is measured. If after the scattering a small change of neutron's energy occurs, the neutron will have a different velocity in the second field and neutrons' spins do not return to their initial state. Neutrons will arrive with slightly different polarization compared to that before the first field. This change of beam polarization contains the information about the energy change. Since the second coil can usually be moved, it's possible to investigate different Q values and study the microscopic dynamics in the sample at different length scales.

NSE measurements directly yield the intermediate scattering function $S(Q, t)$. Its initial slope can be described by

$$S(Q, t) \propto \exp(-D_{\text{app}}(Q)Q^2t) \quad (2.4.1)$$

where D_{app} is the apparent diffusion coefficient, which is related to the apparent hydrodynamic radius

$$R_{\text{H}}^{\text{app}}(Q) = \frac{k_{\text{B}}T}{6\pi\eta D_{\text{app}}(Q)}. \quad (2.4.2)$$

For the diffusion of non-interacting, spherical particles, $R_{\text{H}}^{\text{app}}$ coincides with the geometrical radius.

The diffusion of a rod can be described using the Broersma equation[40] for the translational (D_{rod}) and the rotational (Θ_{rod}) diffusion coefficient:

$$D_{\text{rod}} = \left(\frac{k_{\text{B}}T}{3\pi\eta_{\text{solv}}L} \right) (\delta - 0.5 [\gamma_{\parallel}(\delta) + \gamma_{\perp}(\delta)]) \quad (2.4.3)$$

$$\Theta_{\text{rod}} = \left(\frac{3k_{\text{B}}T}{\pi\eta_{\text{solv}}L^3} \right) (\delta - \zeta(\delta)), \quad (2.4.4)$$

where $\delta = \ln(L/R)$, $\gamma_{\parallel} = 1.27 - 7.4(1/\delta - 0.34)^2$, $\gamma_{\perp} = 0.19 - 4.2(1/\delta - 0.39)^2$ and $\zeta = 1.45 - 7.2(1/\delta - 0.27)^2$. This results in an intermediate scattering function with a double exponential decay:

$$S_{\text{rod}}(Q, t) = s_0(Q) \exp(-D_{\text{rod}}Q^2t) + s_1(Q) \exp(-(D_{\text{rod}}Q^2 + 6\Theta_{\text{rod}})t) \quad (2.4.5)$$

with the amplitudes

$$\begin{aligned} s_0(Q) &= \left(\frac{2}{QL} \int_0^{\frac{QL}{2}} j_0(z) dz \right)^2 \\ s_1(Q) &= 5 \left(\frac{1}{QL} \left(-3j_1\left(\frac{QL}{2}\right) + \int_0^{\frac{QL}{2}} j_0(z) dz \right) \right)^2 \end{aligned} \quad (2.4.6)$$

where j_n is the n_{th} order spherical Bessel function. A structurally similar expression with different coefficients was obtained by Ortega et al. [204]. Within the t and Q range of NSE, the decay due to rotational diffusion is a small correction.

2.5 Molecular Dynamics (MD) Simulations

2.5.1 Principle

Molecular Dynamics Simulation is a computational method used to simulate the behavior of interacting molecules based on a predetermined set of interaction parameters, called force field (FF). The first MD simulations were performed by Alder and Wainwright [8] in the late 1950's to study the interactions of hard spheres. Since then, MD simulations have been used more and more widely due to improvements in computer performances, force field optimization, and development of versatile and user-friendly simulations packages [129]. MD simulations have been widely used in modeling short peptides [37, 96, 182, 247, 286], protein-protein interactions [19, 22, 216], lipid-protein complexes [111, 135, 150, 182, 243, 247, 286], as well as in computational drug discovery and design [39, 72, 83] and neuroscience [70, 75, 80, 138], where they are used both to interpret experimental results and to guide experimental work.

The essence of MD simulations is to produce a dynamical trajectory of the molecular system by integrating Newton's equations of motion. The trajectory is an ensemble of frames, where each frame contains the positions of all atoms at a specific point in time or in simple words it represents the evolution of the system over the time. Considering a system composed of N particles (typically atoms), to perform an MD simulation it is necessary to define the initial positions (and velocities) of each particle, the interaction between particles (i.e., the force field) and the boundary conditions to use. The interactions are represented by a potential energy $U(\vec{r}_1, \vec{r}_2, \dots, \vec{r}_N)$ that depends on the particle coordinates \vec{r} . Once the initial conditions are defined, the classical equation of motion, eq. (2.5.1), can be solved:

$$m_i \frac{d^2 \vec{r}_i}{dt^2} = \vec{f}_i = -\vec{\nabla}_i U(\vec{r}_1, \vec{r}_2, \dots, \vec{r}_N) \quad (2.5.1)$$

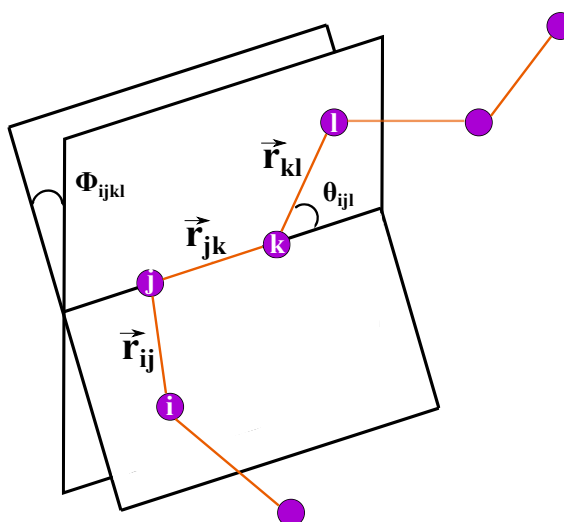


Figure 2.9: Geometry of a chain molecule, illustrating the interatomic distances r_{ij} , r_{jk} , r_{kl} , the bend angle θ_{ijk} and the torsion angle ϕ_{ijkl} .

2.5.2 Bonded Interactions

Molecules are defined as a group of atoms that are held in their geometrical shapes through so-called bonded interactions. Chemical bonds are described by simple harmonic potentials that approximate the quantum-chemical bond potential. Considering a simple molecular geometry, see fig. 2.9, the bond length coincides with the interatomic distance $r_{ij} = |\mathbf{r}_i - \mathbf{r}_j|$ and the associate harmonic potential is given in eq. (2.5.3), where r_{eq} indicates the equilibrium separation and k_{ij}^r the spring constant. A good estimation for r_{eq} values can be obtained from X-ray diffraction experiments [9, 77, 139], while the spring constant k_{ij}^r may be calculated from Raman spectra [208, 225]. The bending angle term potential is defined by eq. (2.5.4) and it is also represented by a harmonic potential, with the bond angle θ_{ijk} that is between successive bond vectors like $\mathbf{r}_{jk}^{\rightarrow}$ and $\mathbf{r}_{kl}^{\rightarrow}$. If the molecule contains more than three atoms in a row, a torsional term can be included, see eq. (2.5.5), with ϕ_{ijkl} the torsion angle. This term accounts for the (effective) rotational potential.

2.5.3 Non-Bonded Interactions

Non-bonded interactions describe interactions between atoms that are not intimately linked via covalent bonds. All intermolecular interactions are described in this way, but also interactions between atoms of the same molecule when they are sufficiently distant connectivity-wise. The pair-wise additive approximation is commonly used in treating the non-bonded

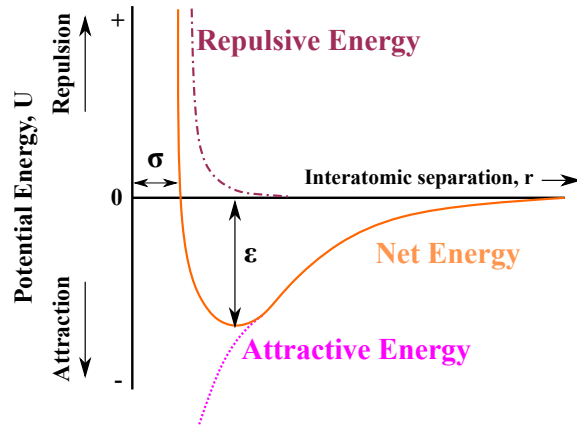


Figure 2.10: Variation of the attractive, repulsive and net potential energies as function of the interatomic separation, r , between two isolated atoms.

interactions. The total potential energy of a system of N interacting atoms is given by:

$$U(\vec{r}_1, \vec{r}_2, \dots, \vec{r}_N) = \sum_{i < j}^N U_2(r_i, r_j) + \sum_{i < j < k}^N U_3(r_i, r_j, r_k) + \dots + \sum_{i < j < k, \dots, n}^N U_n(r_i, r_j, r_k, \dots, r_n) \quad (2.5.2)$$

with U_n the n -body interaction term. This series is usually truncated after the first term, that is the pair-wise additive approximation. It is widely used and provides satisfactory results [66]. Usually three types of non-bonded interactions are considered: hardcore repulsion, van der Waals (vdW) attraction and Coulomb interaction. The former two are generally modeled with the 12-6 Lennard-Jones (LJ) potential, eq. (2.5.6), proposed by Lennard-Jones in 1931 [165], after London had derived that vdW dispersion interaction between atoms decays as r^{-6} . Figure 2.10 shows the Lennard-Jones potential function curve. Considering two atoms, if they are at very close distance r (measured from the center of one particle to the center of the other particle), they will repel each other according to Pauli's principle, whose form is empirically expressed by r^{-12} dependence. If located at a considerable distance, the attractive vdW forces dominate.

For each different pair of atoms it is possible to define two important parameters: ϵ and σ . The former is the well depth and it is a measure of how strongly the two particles attract each other, while the latter is the distance at which the intermolecular potential between the two particles is zero. It represents the van der Waals radius and offers an estimation on how close two nonbonding particles can be. The Lennard-Jones potential has its minimum at a distance of $r = r_m = 2^{1/6}\sigma$. In case of two different atoms A and B, with respective LJ parameters, the effective pair-wise LJ potential of the system is calculated according to FF-specific combination rules [230]. In most of the popular Force fields available, a geometric mean rule (the Berthelot rule) is used for ϵ and a geometric or arithmetic mean rule (the Lorentz rule) for σ [288], so that: $\epsilon_{AB} = \sqrt{\epsilon_A \epsilon_B}$ and $\sigma_{AB} = (\sigma_A + \sigma_B)/2$.

To take into account electrostatic charges the Coulomb potential is included in the FF, eq. (2.5.7), where q_i and q_j are the charges and ϵ_0 is the permittivity of free space. In a generic system, charges contribution comes not only from ions, with their total positive or negative charge, but also from partial charges of atoms in any polar molecule, due to the differences in electronegativities of different elements.

Merging together the discussion of this section and section 2.5.2, an example of Force field is given:

$$U = \frac{1}{2} \sum_{\text{bonds}} k_{ij}^r (r_{ij} - r_{eq})^2 \quad (2.5.3)$$

$$+ \frac{1}{2} \sum_{\substack{\text{bend} \\ \text{angles}}} k_{ijk}^\theta (\theta_{ijk} - \theta_{eq})^2 \quad (2.5.4)$$

$$+ \frac{1}{2} \sum_{\substack{\text{torsion} \\ \text{angles}}} \sum_m k_{ijkl}^{\phi,m} (1 + \cos(m\phi_{ijkl} - \gamma_m)) \quad (2.5.5)$$

$$+ \sum_{\text{LJ}} 4\epsilon_{ij} \left(\frac{\sigma_{ij}^{12}}{r_{ij}^{12}} - \frac{\sigma_{ij}^6}{r_{ij}^6} \right) \quad (2.5.6)$$

$$+ \frac{1}{4\pi\epsilon_0} \sum_{\text{elec}} \frac{q_i q_j}{r_{ij}}, \quad (2.5.7)$$

The parameters of the force field ($k_{ij}^r, r_{eq}, k_{ijk}^\theta, \theta_{eq}, k_{ijkl}^{\phi,m}, \gamma_m, \epsilon_{ij}, \sigma_{ij}, q$) can be derived with different procedures. Some of them are derived from quantum chemistry calculations, while others from experimental data. Since these parameters are usually obtained by studying systems that are not necessarily the same used in the simulation, FFs have inherent approximations which can introduce errors into simulations. However, over the last decades the ability of a large community of researchers have optimized FFs, improving the reliability of MD-derived findings. An important factor that impact a FF is the accuracy, that is the capability of estimate experimental observables [178], like dielectric constant, isothermal compressibility, thermal expansion coefficient, heat capacity, density, diffusion coefficient, viscosity, in the simple case of the water [244].

2.5.4 Boundary Conditions

Macroscopic systems are extremely large and consequently are expensive to compute by MD simulations. Normally, only small systems on the order of 10 x 10 x 10 nm can be simulated conveniently. It could be possible to use a box with rigid walls, but then the surface effects would affect the real bulk properties of the system. For this reason, the application of periodic boundary condition (PBC) is needed. PBC means that each unit

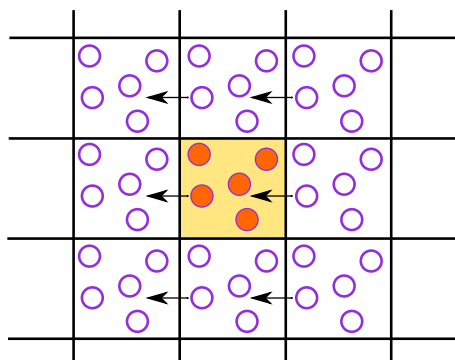


Figure 2.11: Schematic representation of periodic boundary condition. The unit cell is centered, in yellow.

cell is surrounded by an infinite number of replicas of itself, see fig. 2.11. As a particle moves out of the unit cell, another will enter from an adjacent box with the same speed to replace it, keeping the particle number constant. However, even using periodic boundary conditions there are finite-size effects that can lead to artifacts in certain aspects. As consequence of PBC, for example, both Lennard-Jones and Coulomb potential are truncated at a finite distance, r_{cut} , such that only the interactions between particles separated by a distance smaller than r_{cut} are taken into account. However, while the LJ potential is simply truncated at a certain distance (around 1 nm), the Coulomb potential is more problematic since it does not decay with distance rapidly enough to allow a safe simple truncation. Long-range forces, in fact, should never be truncated so that special algorithms are needed to be implemented in the FF, like reaction field or particle mesh ewald methods.

2.5.5 Thermodynamic Ensembles

The integration of eq. (2.5.1) leads to a trajectory in the microcanonical or NVE ensemble [133], where the number of particles N , the volume of the simulation cell V , and the energy of the system E are kept constant. The NVE ensemble that comes out of a standard MD simulation does not directly map to common experimental conditions. To compare MD with experiments, it is more useful to work at constant temperature (the canonical NVT ensemble) or pressure (the isothermal-isobaric NpT ensemble), that can be done using one of the available thermostats and barostats. In principle thermostats serve as a simulated heat bath around the system (with the heat bath much larger than the system), keeping their average temperature at a set value. A thermostat algorithm (which generates a thermodynamical ensemble at constant temperature) will compare the instantaneous temperature of the system, encoded in the distribution of particle kinetic energies, to that of the heat bath to which the system is coupled. Since any change in T can be achieved by varying the velocities of the atoms, thermostats re-scale the velocities of particles to

control the temperature. Just like using a thermostat to control the temperature, a barostat algorithm keeps the pressure constant by scaling the volume of the system. The changes in volume of the box can be isotropic or non-isotropic (for example only in one spatial direction), as it was done in the present work. Particularly important is the isothermal-isobaric (NpT) ensemble obtained by combining a barostat and a thermostat because these are the most common experimental boundary conditions.

Different algorithms are available with different accuracy in describing the dynamics of the system. However, the larger is the system, the less important are the differences between them [133], making the choice not very critical.

Chapter 3

Materials, Sample Preparation and Experimental Methods

This chapter is based on the text of the manuscripts^{1, 2, 3}.

3.1 Chemicals

JR 400 (Dow Chemical, USA, see fig. 3.1) is a cationically modified hydroxyethylcellulose with a molecular weight of about 500000 g/mol (PDI = 1.85 [168], with a partial molar density in water 1.66 g/ml) and a cationic group on 27 % of the glucose units, resulting in 1000 g of PE per mol of positive charges[261]. Its overlap concentration was found to be 0.8 wt% [124].

SOS, SDS, SDP and STS (all at 98.5%), see fig. 3.2 were purchased from Sigma-Aldrich and used without further purification. Water was taken from a Millipore System; SANS and NSE samples were prepared in D₂O (99.9 % isotopic purity, Sigma-Aldrich Co., St. Louis, MO).

¹On the mechanism of shear-thinning in viscous oppositely charged polyelectrolyte surfactant complexes (PESCs). *J.Phys.Chem.B*,124:909-913, 2020. Del Sorbo et al. [74]

²Influence of the surfactant tail length on the viscosity of oppositely charged polyelectrolyte/surfactant complexes. *Macromolecules*, 2021. Del Sorbo et al. [73]

³Stimuli-Responsive Polyelectrolyte Surfactant Complexes for the Reversible Control of Solution Viscosity.

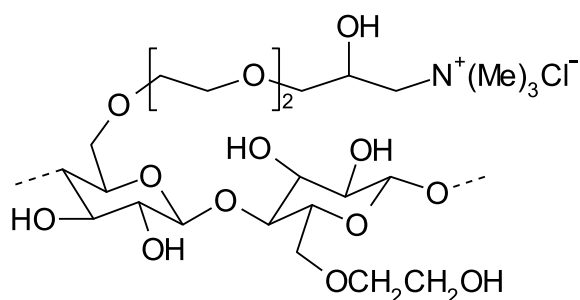


Figure 3.1: Chemical structure of JR 400.

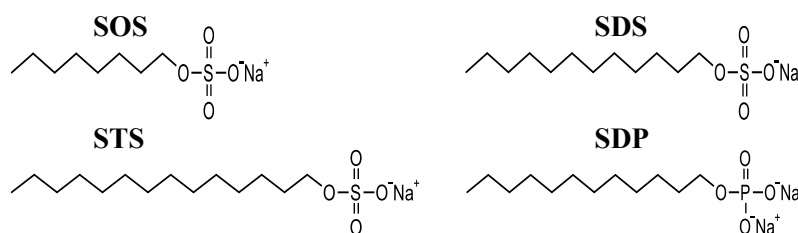


Figure 3.2: Chemical structure of SOS, SDS, STS and SDP.

3.2 Sample Preparation

JR 400 stock solution at 1 wt% was prepared by mixing the appropriate amount of PE powder and solvent (H_2O or D_2O). The stock solution was stirred overnight to ensure the complete dissolution of the PE. All mixed samples were prepared by adding the surfactant powder to a quantity of JR 400 solution. The amount of surfactant and JR 400 solution were calculated according to the relative charge ratio $Z = [\text{PE charges}]/[\text{surfactant charges}]$ of the sample. Each sample was gently stirred for 12 h in order to get homogeneous solutions if in the one phase region of the phase diagram. The stirring speed has to be low especially for viscous solutions, in order to avoid the formation of micro-bubbles which have to be avoided for the measurements.

Particular attention is reserved to JR 400/SDP samples, since the pH-dependence of the surfactant: at neutral pH, SDP is present in its hydrogen phosphate form with a single negative charge on its headgroup. Around $\text{pH} = 9$, a transition from hydrogen phosphate to phosphate with 2 negative charges is observed [193, 269], see fig. C.1. Samples either had a pH of 7 where the surfactant has a single charge or a pH of 12, where the surfactant headgroup bears two negative charges. The pH of the solutions was adapted by adding appropriate amounts of NaOH ($\geq 98\%$, Sigma-Aldrich) and controlled by Mettler Toledo pH-meter. It should also be noted that at neutral pH, a small fraction of the surfactant forms an insoluble salt complex [18], which gives the solutions a turbid appearance.

For neutron experiments the solvent used is D_2O and concentrations were adapted to its

higher density so as to keep the molar concentrations identical to the corresponding samples in H₂O.

Samples were prepared and characterized at room temperature unless specified otherwise.

3.3 Experimental Methods

The following sections describe the setting for each technique used to characterize the samples in this study.

3.3.1 DLS

In this project DLS measurements were performed at 25°C with a setup consisting of an ALV 7004 Correlator, an ALV CGS-3 Goniometer and a He-Ne Laser with a wavelength of 632.8 nm. Cylindrical sample cells were placed in an index matching vat filled with toluene. Autocorrelation functions were recorded under different angles between 50° and 150°. Samples were equilibrated for 15 min before to start the measurements.

3.3.2 Rheology

In this thesis viscosity measurements were performed using an Anton-Paar MCR 501 Rheometer in cone/plate geometry with a 50 mm cone diameter and 1° cone angle. During the measurements, a solvent trap was used to prevent water evaporation and subsequent changes in the solutions structure. To determine the shear rate dependence, the shear rate was increased from 0.01 s⁻¹ to 1000 s⁻¹ and the duration per point was 10 s. Oscillatory shear measurements were performed in the frequency range of 0.01-100 rad/s. The strain amplitude was chosen so as to remain in the linear viscoelastic regime. All measurements were carried out at 25 °C.

3.3.3 SANS

Different SANS experiments were carried out in this work:

- In chapter 4 SANS measurements were performed on the instrument D11 at the Institut Laue-Langevin (ILL, Grenoble, France) using a neutron wavelength of 5.0 Å and sample to detector distances of 1.4, 8 and 39 m, covering a Q -range from 0.022 to 4 nm⁻¹. The rheoSANS setup consists of an Anton-Paar Physica MCR 501 rheometer with a titanium Couette geometry of 30 mm diameter and 0.5 mm gap. SANS data were reduced using the software package BerSANS [147], using the direct beam

flux to obtain data in absolute scale. The anisotropy analysis of the data was performed using the software SASET [192].

Principal Component Analysis (PCA) was used to quantify anisotropy and determine the maximum scattering direction, by finding the vector onto which the projected data, weighed by their intensity, have a maximum variability. For the anisotropy analysis using PCA, only Q -values covering 2π azimuthally of the 8 m measurements were used. The resulting Q -range is 0.125–0.725 nm⁻¹. Additionally, 45° sector averages parallel (0°) and perpendicular (90°) to the direction of shear were taken.

- In chapter 5 and chapter 6 SANS measurements on JR 400/surfactant solutions were performed on the time-of-flight instrument V16 [267] at Helmholtz-Zentrum Berlin (HZB, Berlin, Germany). To cover a range of the magnitude of the scattering vector Q from 0.02 to 5 nm⁻¹, we used a neutron wavelength in the range $1.78 \text{ \AA} < \lambda < 3.75 \text{ \AA}$ for a sample-to-detector distance of 1.7 m and in a second range from $1.56 \text{ \AA} < \lambda < 9.22 \text{ \AA}$ for sample-to-detector distance of 11 m. Data reduction was performed with the software package MantidPlot [20].
- Neutron diffraction (ND) experiments on PE/surfactant precipitates in chapter 5 were performed on D16 [63] at Institut Laue-Langevin (ILL) in Grenoble, France. Measurements were done at a wavelength of $\lambda = 4.5 \text{ \AA}$ for a sample-to-detector distance of 955 mm, in order to cover a Q range from 0.2 to 12 nm⁻¹. The neutron data were corrected for the empty cell, the ambient room background, the nonuniform detector response, the transmission and the thickness of the sample. The scattering intensities were normalized in absolute units with a standard water calibration. Data analysis was performed using the ILL in-house LAMP software [222].

3.3.4 NSE

In this thesis different NSE experiments were performed on the instrument IN15 [88] at the Institut Laue-Langevin (ILL, Grenoble, France):

- In chapter 5, to cover a Q -range from 0.3 to 1.6 nm⁻¹, four different configurations were used, namely detector angles of 3.5°, 6.5° and 9.5° at a wavelength of 10 Å reaching a maximum Fourier time of 194 ns and a detector angle of 8° at a wavelength of 6 Å reaching a maximum Fourier time of 42 ns.
- In chapter 6 were used 4 different configurations with detector angles θ of 7, 4.5, 7.5 and 3.5° using neutrons with wavelengths (longest Fourier time t in parentheses) of

6 Å (42 ns), 10 Å (190 ns), 10 and 13.5 Å (477 ns) covering a Q -range from 0.21 to 1.46 nm⁻¹.

3.3.5 MD Simulations

3.3.5.1 MD Simulations of SOS, SDS, and STS interacting with PE

Atomistic molecular dynamics (MD) simulations of SOS, SDS, and STS interacting with polyelectrolytes were performed using the GROMACS 5.2 package [2] and the GROMOS 53a6 force field framework [203]. Positively charged polyelectrolytes in the form of the polypeptides PLL and PLG, see fig. 5.8 A, were used as generic mimics of JR 400. Stretched, quasi-infinitely long polyelectrolyte chains were represented by cyclically connected, periodically repeated units of $N_{AA} = 30$ amino acids in combination with periodic boundary conditions. The simulation box contained one or two parallel polyelectrolyte chains, 60 surfactant molecules, a number of Na⁺ and/or Cl⁻ as counterions (Gromos 53a6/ions.itp), in addition to the water molecules, which were atomistically represented by the SPC-E water model [33]. The box size was initially 6 nm × 6 nm in xy -direction. In the z -direction (along the polyelectrolyte) the box size was set as $L_z = N_{AA}l_{AA} = 10.8$ nm, according to the average length per amino acid in stretched configuration, $l_{AA} = 0.36$ nm [232]. The simulation time step was $\Delta t = 2$ fs, Lennard-Jones interactions were cut off at 0.9 nm, and electrostatics were treated using the particle-mesh-Ewald method [86] with a 0.9 nm real-space cut-off. Temperature was kept constant at 300 K with a V-rescale thermostat [43] with coupling time constant 0.1 ps. The pressure of 1 bar was controlled using the Berendsen barostat [33] with pressure coupling in xy -direction with a time constant of 0.5 ps and compressibility of 4.5×10^{-10} Pa⁻¹, while keeping L_z constant. Each system was first equilibrated in constant volume and temperature conditions (NVT ensemble) for 10 ps and subsequently in constant pressure and temperature conditions (NPT ensemble) for 100 ps. Production runs had a duration of 100 ns, of which only the last 50 ns were used for the analysis to ensure sufficient equilibration. Starting configurations for SDS micelles were generated with the online tool Micelle Maker [156]. SOS micelle configurations were generated by using SDS micelle coordinates for all those atoms that exist in SOS (i.e., up to the 8th C atom in the tail). For STS, initial configurations were generated via a stepwise alchemic transformation as described in section B.5.1. Simulations were carried out for 2 PE types (PLL and PLG), 2 numbers of PE chains (1 and 2), 3 surfactant types (SOS, SDS, and STS), 2 counterion conditions, see chapter 5, and 2 initial surfactant distributions, amounting to approximately 5 μ s of simulation time in total. Radial distri-

bution functions and sizes of surfactant aggregates were computed with the Gromacs tools `gmx-rdf` and `gmx-clustsize` [233], respectively.

3.3.5.2 Constant-Force Pulling (CFP) MD Simulations

As starting point of CFP simulations, simulated structures formed by two PLL chains and 60 surfactants are used, much like to those shown in fig. 5.9. These aggregates are not unique representations of the mixed aggregates that occur in the experiments, because they may involve more than 2 PE chains on average (from SANS analysis it was found that $N_{\text{PE chains}}$ per aggregate is between 3 and 4, see section 5.2.3). Moreover, the average number of surfactants per mixed aggregate may differ from the experimental situation as well. Nevertheless, this model system is used with the aim to identify robust qualitative trends. In a network, a parallel configuration is one extreme scenario for the contact between two bound chains. In general, two chains can intersect at locally any angle, orthogonal being the other extreme. Both configurations are therefore investigated as schematically illustrated in fig. 7.1.

Chapter 4

Investigation of the Mechanism Responsible of the Shear Thinning behavior of PESCs Solution

This chapter is based on the text of one of the published manuscripts¹.

4.1 Introduction

As stated in chapter 1, PESCs show an extremely rich self aggregation behavior [55, 57, 99, 130] and these systems have attracted the interest of researchers for a few decades now [100]. However, despite recent reviews [90, 107, 151] are available, some aspects of their behavior are still not fully understood. One of these concerns the mechanism behind their shear thinning behavior. To shed light on this mechanism, rheo-SANS measurements were performed on aqueous mixtures of JR 400 and SDS, see figs. 3.1 and 3.2 for chemical structure .

Rheo-SANS allows to monitor structural changes using small angle neutron scattering while samples are under shear. This method has been used to great success for wormlike micelles and other colloidal systems [45, 79, 84, 91, 157, 221, 226, 248]. Aqueous mixtures of 1 wt% JR 400/SDS show a remarkable increase in viscosity by several orders of

¹On the mechanism of shear-thinning in viscous oppositely charged polyelectrolyte surfactant complexes (PESCs). *J.Phys.Chem.B*,124:909-913, 2020. Del Sorbo et al. [74]

magnitude relative to the pure PE solution at the same PE concentration [100]. A graph of the zero shear viscosity, η_0 , as a function of the charge ratio Z , can be found in the Appendix A, fig. A.1. A noticeable increase of the viscosity is observed for charge ratios of about $Z = 10$ (corresponding to 1 mM surfactant for a 1 wt% JR 400 solution) and less up to the onset of the two phase region around $Z = 2.5$. Combining SANS and NSE spectroscopy, it was shown that this increase in viscosity is due to the formation of rodlike aggregates with a diameter similar to a surfactant micelle and a length of about 50 nm [123]. This is different from wormlike micellar systems or stiff, strongly anisotropic colloids [160, 161] in that no overlap between the aggregates themselves is needed to obtain viscous samples as they only act as cross-links between PE chains and therefore relatively small surfactant concentrations of 3 mM and less are sufficient to obtain viscous samples, while surfactant concentrations in viscous wormlike micellar solutions are typically on the order of some 10 mM [252, 260].

JR 400/SDS solutions display shear thinning behavior beyond a critical shear rate $\dot{\gamma}_{crit}$, see fig. A.2, and here rheo-SANS has been used to investigate the underlying mechanism leading to this behavior. This is not only an interesting question from fundamental science but also highly relevant for applications, as such mixtures are frequently employed in formulations from detergency, cosmetics, shampoos etc., where they are applied under shearing conditions. In principle, two different scenarios are thinkable:

1. Under shear, PE chains are torn out of the aggregates, reducing their number per aggregate and consequently reducing the aggregate's efficiency as cross-linker, which ultimately leads to a situation comparable to what is observed at low PE concentrations. In this scenario, the radially averaged scattering intensity would decrease noticeably in the Q -range where the aggregates are observed (see the Appendix A, figs. A.3 and A.4)
2. Knowing from NSE, that the PE chains are not frozen in the aggregates and assuming that they can move mostly along the long axis of the aggregates, it would be sufficient if the aggregates align along the direction of shear. In this scenario, the radially averaged intensity of the radial rheoSANS data would remain identical but the scattering pattern would become anisotropic.

4.2 Results and Discussion

SANS and rheo-SANS experiments are detailed in section 3.3.3, complementary offline rheology measurements in section 3.3.2.

SANS data treatment is explained in Appendix A, section A.2.1.

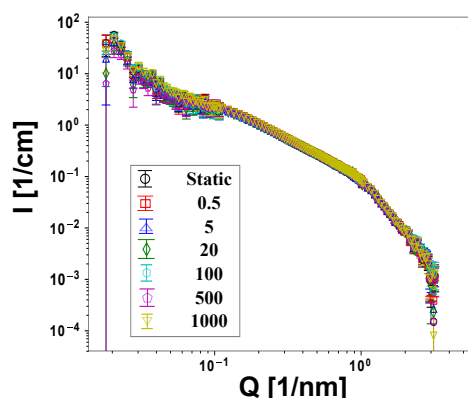


Figure 4.1: SANS curves for sample with $Z = 3$ at different shear rates indicated in the graph. The SANS intensity remains unchanged, while a reduction of the number of chains per aggregate should result in a small but noticeable difference as shown in figs. A.3 and A.4.

Sample preparation is illustrated in section 3.2.

4.2.1 Rheo-SANS

Performing rheo-SANS measurements on viscous, shear thinning PESCs allows to differentiate between the two proposed scenarios. While a reduction of the cross-linking efficiency of the rodlike aggregates by the reduction of the number of PE chains in the aggregates would reduce the scattering intensity, an alignment of the aggregates would only result in an anisotropic scattering pattern, leaving the radially averaged intensity unchanged. As can be seen in figs. A.5 and 4.1 the radially averaged intensity is independent of the applied shear rate at shear rates significantly above the critical shear rate (0.9 1/s for $Z = 3$), even though a small, yet noticeable difference should be observed, if the number of chains per aggregate would be reduced. Specifically, the intensity should be reduced in the intermediate Q -range and somewhat increased in the high Q -range because of the decrease of the volume fraction of mixed aggregates and an increase of the volume fraction of free PE chains (see figs. A.3 and A.4 for the theoretical curves in which the fraction of JR 400 in the mixed aggregates x_{PE} has been varied, and fig. A.5 for a magnification of the mid Q -range of fig. 4.1). From this it is possible to exclude the first scenario, where shear thinning is caused by the disruption of the cross-linking mixed aggregates. At first glance, no anisotropy is visible in the 2D detector images, see fig. 4.2. Taking 45° sector averages on the other hand with different angles relative to the direction of shear shows no difference at rest, see fig. A.6, and a small but significant difference under shear, see fig. A.7, which shows that the anisotropy is induced by shearing the sample. These anisotropic scattering patterns were now analysed in a quantitative fashion using principal component analysis

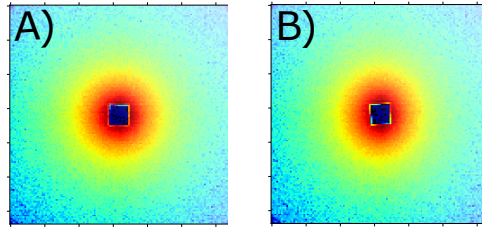


Figure 4.2: 2D detector images for sample with $Z = 3$ A) at rest and B) at $\dot{\gamma} = 500$ 1/s. No pronounced anisotropy can be seen.

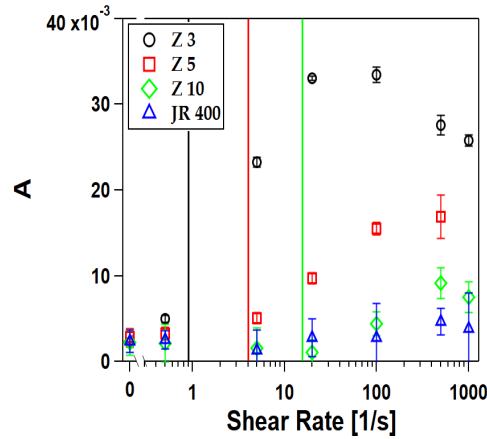


Figure 4.3: Anisotropy parameter A from PCA for samples indicated in the graph using the mid- Q configuration (8 m sample to detector distance). The more viscous samples with $Z = 3$ and $Z = 5$ show an increase of anisotropy with the shear rate. The critical shear rates $\dot{\gamma}_{crit}$ of the samples as determined from viscometry, see fig. A.2, are indicated in the graph as vertical lines. The onset of the increase of A roughly corresponds to $\dot{\gamma}_{crit}$.

(PCA) [36, 192]. PCA is an established method from pattern recognition that consists in finding a succession of orthogonal vectors accounting for the highest variability in a data set. Applied to 2D intensity data, the main component indicates the direction and breadth of maximum dispersion in the intensities, i.e., the main axis of anisotropy and its amplitude. It yields an anisotropy parameter A with $A = 0$ for a completely isotropic scattering pattern and $A = 1$ for scattering only along one direction. Performing PCA on the data at mid- Q where the rodlike aggregates are seen, shows that a weak anisotropy forms as the shear rate is increased. The effects are negligible for pure JR 400 and the sample with $Z = 10$ which have a rather low viscosity. It becomes far more pronounced for the more viscous samples with $Z = 5$ and $Z = 3$, see fig. 4.3. It can also be seen that the onset of the increase in anisotropy is at significantly lower shear rates for $Z = 3$ than for $Z = 5$ which is in agreement with the significantly lower $\dot{\gamma}_{crit}$ at $Z = 3$ (0.9 vs 4 1/s). The onset of anisotropy and the critical shear rate are in good agreement, which indicates that this structural change is at the origin of the macroscopic change of the flow behavior.

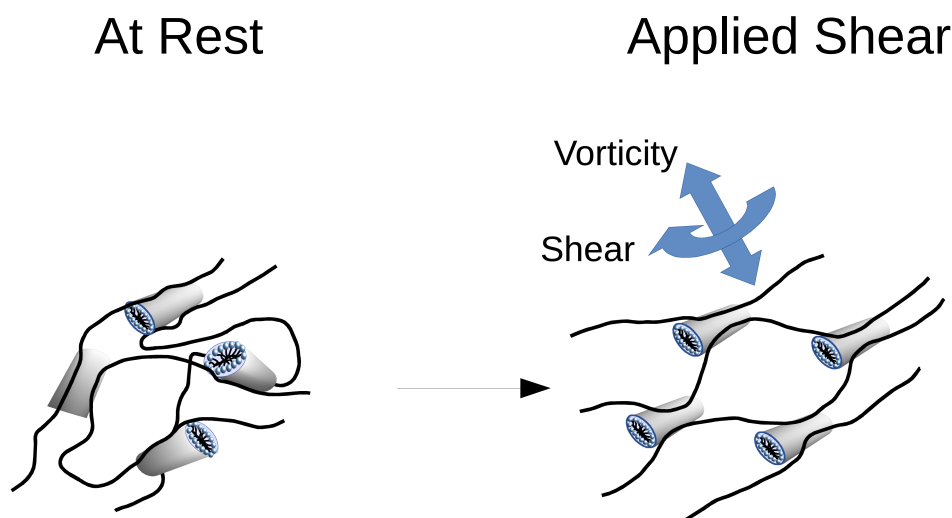


Figure 4.4: Rheo-SANS measurements support scenario (II): Applying shear, the fraction of free PE chains does not increase. The reason for the shear thinning behavior of the solutions is an alignment of the rodlike aggregates in the direction of flow which allows the PE chains to move along the flow direction more easily.

4.3 Conclusion

In summary, using rheo-SANS it is possible to rule out that shear thinning in JR 400/SDS system is related to the rupture of the mixed rodlike aggregates which were found to be responsible for the increase in viscosity previously. In fact, it is observed that a slight orientation of the rodlike aggregates is sufficient. This matches with previous NSE results of Hoffmann et al. [125], where it was found that the PE retains some of its freedom of movement even in the aggregates. This motion might be mostly along the long axis of the aggregates and orienting them in the direction of shear allows for an easier relaxation of shear stress and this orientation of aggregates makes the system shear thinning. An interesting detail can be seen when inspecting fig. 4.3 more carefully. For $Z = 3$ at the two highest shear rates a slight decrease in the anisotropy can be seen. This might indicate that beyond a certain shear rate, the decrease of viscosity is governed by an increase of mobility of the PE chains in the aggregates. In principle, rheo-NSE measurements [146] might be able to clarify this point in the future.

Chapter 5

The Influence of the Surfactant Tail Length on PESCs Viscosity

This chapter is based on the text of one of the published manuscripts¹.

5.1 Introduction

As stated in section 1.4.1, previous studies on mixtures of JR 400, see fig. 3.1, and SDS, see fig. 3.2, revealed that in surfactant excess, the PE is decorated with spherical micell-like surfactant aggregates, while in PE excess mixed rod-like aggregates are found [55, 125, 128, 168]. These rod-like surfactant/PE aggregates are responsible for a high degree of interconnection between PE chains, resulting in a pronounced increase in solution viscosity near the phase boundary on the PE-rich side of the phase diagram [125, 126, 128]. Surprisingly, a qualitatively similar but weaker increase of solution viscosity with the addition of anionic surfactant followed by a decrease upon addition of more surfactant has also been observed for mixtures of surfactant and weakly charged gelatin [92] or non-ionic polyethylenoxide (PEO) [253], where it was observed that the maximum viscosity increases with increasing length of the surfactant tail. It was concluded early on by Schwuger [236] from the lack of adsorption of cationic alkyl trimethylammonium surfactants and the pH dependence of the adsorption of SDS that the adsorption of ionic

¹Influence of the surfactant tail length on the viscosity of oppositely charged polyelectrolyte/surfactant complexes. *Macromolecules*, 2021. Del Sorbo et al. [73]

surfactants on PEO was not purely due to hydrophobic interactions and based on the dependence of the binding of anionic surfactant on the cation of added salt. Dubin et al. [81] concluded that binding of SDS is mediated by the cation, which is bound by PEO, making the situation comparable to the oppositely charged PESCs studied here. However so far, the vast majority of studies on PESCs with anionic surfactants have used SDS as surfactant [100, 109, 122, 168], while still little is known about the influence of the surfactant tail length on the viscosity of oppositely charged PESC solutions. Although there are studies that investigated the influence of the surfactant tail length on the macroscopic behavior of PESC solutions [5, 24, 256, 294, 297], the dynamics and the mesostructure of the aggregates has remained unexplored, so far.

Here, the PESC's mesoscopic structure and dynamics have been investigated in order to provide an explanation for the influence of surfactant alkyl tail length on the macroscopic flow behavior. For this purpose, mixtures of JR 400 and alkyl sulphates with two different tail lengths have been studied: sodium octyl sulphate (SOS, 8 carbon atoms) and sodium tetradecyl sulphate (STS, 14 carbon atoms), see fig. 3.2, for various mixing ratios, Z , of charges of polyelectrolyte to surfactant. In this study different experimental techniques have been used: Rheology, SANS, NSE and complementary solvent-explicit atomistic molecular dynamics (MD) simulations.

While rheology measurements provide information on the macroscopic flow behavior, SANS and NSE shed light on the mesoscopic structure and dynamics of the system. Finally, the MD simulations were aimed at elucidating additional atomistic details of the interaction of PE chains with monoalkylsulfate surfactants. To this end, the simulations involved generic stretched PEs with adjustable charge density exposed to SOS, SDS, and STS.

5.2 Results and Discussion

SANS and diffraction experiments are detailed in section 3.3.3. Rheology measurements in section 3.3.2 while NSE tests in section 3.3.4.

DLS measurements are shown in Appendix B and detailed in section 3.3.1.

Sample preparation is illustrated in section 3.2.

5.2.1 Phase behavior

At first, the phase behavior of SOS/JR 400 and STS/JR 400 mixed solutions as a function of Z is established by visual inspection. For STS/JR 400 precipitation is observed near

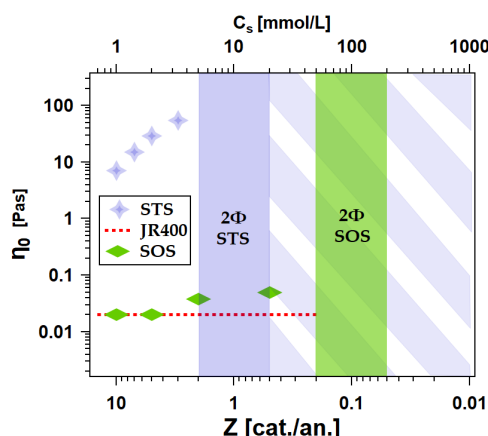


Figure 5.1: Zero shear viscosity of JR 400, SOS and STS as function of Z (bottom) and surfactant concentration (top). In the picture are also shown: 1) 2 phase region of SOS (in green), 2) 2 phase region of STS where the precipitate is a mix of JR 400/STS (blue) and 3) 2 phase region of STS where the precipitate is only surfactant (oblique rectangles in light blue).

charge equilibrium ($Z = 1$), while SOS/JR 400 exhibits a shift of the two phase region to lower Z values (i.e., higher surfactant concentrations), see fig. 5.1. These observations are in agreement with the solubility diagrams of these solutions reported by Goddard and Hannan [97] and consistent with earlier reports on SDS/JR 400 [107, 125], SDBS/JR 400, and SDES/JR 400 [55, 124]. According to Goddard and Hannan [97] such a shift of the phase boundary is expected for surfactants with high CAC. For both SOS and STS, solutions are clear when JR 400 is in excess (i.e., high values of Z). For STS it is necessary to increase the temperature to 35 °C in order to obtain a clear solution in the surfactant excess regime ($Z \lesssim 0.1$). In contrast, the precipitates observed close to charge equilibrium cannot be dissolved by heating the samples. Neutron diffraction data obtained with the instrument D16 of ILL show that aggregates at high surfactant concentrations exhibit the same peaks as pure STS powder, see fig. B.7, whereas the precipitates at charge equilibrium do not exhibit any peaks. These findings suggest that the formation of clear monophasic solutions in the surfactant excess regime in STS/JR 400 is hampered by the poor solubility of STS at room temperature rather than by its inability to redissolve the precipitates.

5.2.2 Rheological behavior

STS/JR 400 samples in the PE excess regime exhibit a remarkable increase in viscosity, while SOS/JR 400 samples behave water-like over the whole range of compositions studied here. To quantify this effect, steady and oscillatory shear measurements were performed in the PE excess regime of the phase diagram with both SOS/JR 400 and STS/JR 400. Figure 5.1 shows the zero-shear viscosity, η_0 , of the two systems as a function of Z . While for

Table 5.1: Parameters obtained from Oscillatory Shear Rheology of STS/JR 400 mixtures.

Z /	ω_{cross} [rad/s]	τ_{cross} [s]	G_0 [Pa]	ϵ [m ⁻³]	ξ [nm]
10	2.68	2	24	5.9×10^{21}	55
7	1.93	3	39	9.5×10^{21}	47
5	1	6	57	1.3×10^{22}	42
3	0.52	12	58	1.4×10^{22}	41

SOS/JR 400 the viscosity is the same order of magnitude of the pure JR 400 solution, for JR 400/STS an increase of the viscosity is observed by three orders of magnitude when approaching the phase boundary. Typical flow curves for JR 400/STS at various Z are shown in fig. B.1. In all cases, the observed shear-thinning is reversible for increasing or decreasing the shear rate $\dot{\gamma}$, with a Newtonian region at low $\dot{\gamma}$ values. Upon increasing the STS concentration (i.e., reducing Z), the solutions become more viscous and the critical shear rate $\dot{\gamma}_{\text{crit}}$, which marks the onset of shear thinning, shifts to lower values, see fig. B.3. The shear-thinning behavior can be attributed to modifications in macromolecular organisation as the shear rate changes, presumably similar to SDS/JR 400 where it was found that cylindrical aggregates slightly align under shear [74]. To obtain additional information on the PE-surfactant micro-structural network, oscillatory shear measurements were performed. The profiles of the storage modulus G' and loss modulus G'' obtained from those experiments are shown in fig. B.2. These measurements reveal that all the samples exhibit viscoelastic behavior, as found previously for other PESCs [124, 126, 144, 179, 265]. At low frequencies, the viscous response G'' prevails over the elastic response G' , while at high frequencies G' is larger than G'' . As the frequency increases, a cross-over point is reached ($G' = G''$) and the solution behavior switches from viscous to elastic, depending on Z ; with decreasing Z it shifts toward lower frequencies. The inverse of the frequency at the crossover defines the structural relaxation time τ_{cross} which increases as more surfactant is added [126], see fig. B.4.

Based on the theory by Green and Tobolsky [108, 246], the plateau value of G' , termed G_0 , see section 2.2.1 for more details, is related to the network junction density via:

$$G_0 = g\epsilon k_B T \quad (5.2.1)$$

with the network junction density ϵ , the absolute temperature T , Boltzmann's constant k_B and a factor g to account for the strength of the junctions in units of $k_B T$, which is initially set to 1 for the calculation of the values in table 5.1. The same holds semi-quantitatively for the value at the maximum oscillation frequency if the plateau is not reached. This allows

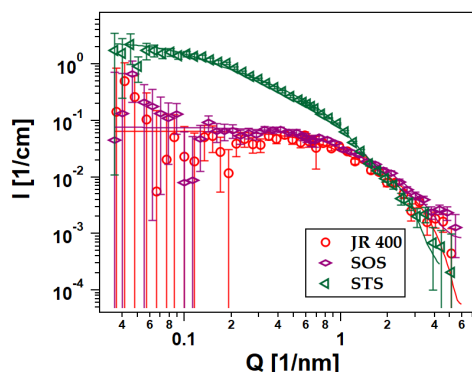


Figure 5.2: Comparison of the SANS curves of 1 wt% JR 400 with SOS and STS, both at charge ratio $Z = 5$ and pure JR 400. While the curve of STS/JR 400 shows the formation of rodlike aggregates, hardly any structural changes compared to the pure PE can be seen for SOS/JR 400.

to calculate the mesh size $\xi = \epsilon^{-1/3}$ which turns out to be roughly on the order 50 nm, with only a weak dependence on the choice of g ($\xi \propto g^{1/3}$). All rheological parameters are summarised in table 5.1. In conclusion, a decrease in Z coincides with a decrease in the mesh size and at the same time with an increase in the relaxation time. Taken together this indicates that lower Z values result in more pronounced PE/surfactant networks to which the higher viscosities seen in fig. 5.1 may be attributed.

5.2.3 SANS

In order to understand the micro-structural organisation of these solutions, SANS measurements were performed on samples with 1% of JR 400 and variable concentrations of SOS and STS on both sides of the phase diagram. The pure JR 400 solution shows the typical scattering pattern of a semi-dilute PE solution with a Q^{-1} slope at high Q down to about 0.8 nm^{-1} , see fig. 5.2. The curve shows a weak PE peak, which is neglected when modelling the data as thin cylinders, see eq. (B.2.1). The fit results for the radius ($R_{\text{PE}} = 0.8 \text{ nm}$) and the persistence length of the free PE segments ($L_{\text{PE}} = 6 \text{ nm}$) are in good agreement with previous results [125] and are used as fixed parameters for the fits of data from samples with added surfactant.

Adding an excess of either SOS or STS to JR 400 beyond the limit of the respective two phase region, see fig. 5.1, and heating the sample above 35°C for STS results in a scattering pattern corresponding to charged spherical micelles, see fig. B.6. Comparing samples of 1 wt% JR 400 and STS or SOS at the same charge ratio, $Z = 5$, in the PE excess regime, see fig. 5.2, it can be seen that the sample with STS forms elongated aggregates, as evidenced by the Q^{-1} slope at $0.2 < Q < 1 \text{ nm}^{-1}$, while no such aggregates can be observed in the sample with SOS, whose scattering pattern is almost identical to that of pure

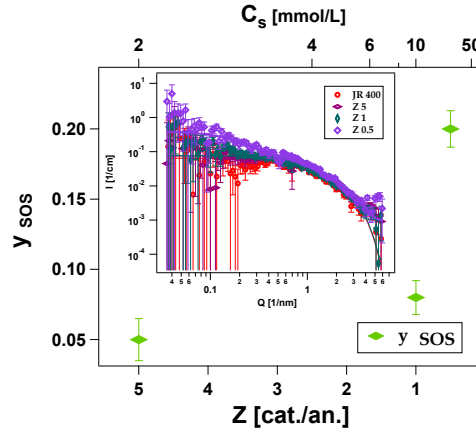


Figure 5.3: y_{SOS} as a function of charge ratio (bottom) and surfactant concentration (top). Inset: SANS curves of JR 400, and of SOS/JR 400 1 wt % at $Z = 5$, $Z = 1$ and $Z = 0.5$.

PE. This observation suggests that the increase in viscosity observed for 1 wt% JR 400 and STS in the PE excess regime is related to the formation of aggregates while no increased viscosity is observed for SOS/JR 400 since no aggregates are formed. Samples with SOS in the PE-excess regime do not exhibit any significant structural changes relative to the pure PE except a slight increase in intensity and the disappearance of the (weak) PE peak [48, 49, 194, 196]. In fact, the same would also result from the addition of a simple salt [196]. This behavior indicates that SOS molecules adsorb onto the PE chain predominantly as individuals, without forming aggregates. An upper limit for the amount of adsorbed SOS can be given by describing the SANS curves with the same structure as the pure JR 400, only adapting the volume fraction and scattering length density of the cylinders with adsorbed SOS so that

$$\phi_{SOS/PE} = \phi_{PE} + y_{SOS}\phi_{SOS} \quad (5.2.2)$$

and

$$SLD_{SOS/PE} = \frac{\phi_{PE}}{\phi_{SOS/PE}} SLD_{PE} + \frac{y_{SOS}\phi_{SOS}}{\phi_{SOS/PE}} SLD_{SOS} \quad (5.2.3)$$

where y_{SOS} is the fraction of the surfactant bound to the PE chains. The values obtained for y_{SOS} are close to zero for up to 10 mmol/L SOS and only at 20 mmol/L ($Z = 0.5$) a significant fraction of the surfactant is adsorbed on the PE chain, which shows that at 1% JR 400 the concentration at which the surfactant adsorption starts is between 15 and 20 mmol/L, see fig. 5.3. Accordingly, the shift in the two phase region can be attributed to the high CAC of the SOS/JR 400 system [151]. At $Z = 0.5$ the SOS/JR 400 complex has still an excess of PE charges meaning that the amount of the surfactant is still not able to saturate all the charged sites of the polymer chain to reach the charge neutralisation

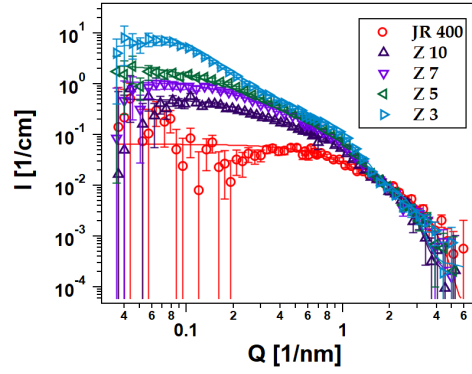


Figure 5.4: SANS curves of STS/JR 400 1 wt % at different charge ratios

concentration, responsible of the precipitation. Highly viscous samples with STS in the PE-excess region of the phase diagram exhibit the formation of aggregates in SANS, see fig. 5.4. The aggregates have a cylindrical shape as can be seen by the Q^{-1} slope between $Q \approx 0.2 \text{ nm}^{-1}$ and $Q \approx 1 \text{ nm}^{-1}$. With $R_{\text{agg}} \approx 2 \text{ nm}$ their radius is significantly larger than that of the pure PE, as can be seen by the kink in the scattering curves between 1 and 2 nm^{-1} , and similar to the one reported earlier for JR 400 samples loaded with SDS [123–125]. The fact that the position of the kink at high Q as well as the onset of the plateau at low Q are relatively constant with the composition of the sample indicates that the structure of the aggregates remains largely independent of Z . Only the sample at the lowest charge ratio in this regime ($Z = 3$) displays a shallow peak at low Q , probably due to interactions between the aggregates, that is not observed for the other samples. Comparing the intensities of the samples with $Z = 10$ and $Z = 5$ at low Q it becomes clear that the aggregates do not only consist of STS but are mixed aggregates. The intensity in the low Q limit for $Z = 10$ is $I_0 \approx 0.4 \text{ nm}^{-1}$ while for $Z = 5$ $I_0 \approx 2 \text{ nm}^{-1}$. In other words, the intensity increases by a factor five while the surfactant concentration is only doubled. Since the shape of the curve remains virtually unchanged, this requires that an increasing amount of JR 400 is incorporated in the aggregates with increasing surfactant concentration.

In order to model the SANS data, as shown in Appendix A, it is therefore necessary to assume that a fraction x_{PE} of the JR 400 is integrated in the aggregates so that their volume fraction, ϕ_{agg} , is given by eq. (A.2.1) and ΔSLD_{agg} by eq. (A.2.4). The aggregates can be described as cylinders, see eq. (2.3.9). However, neglecting the scattering of the PE chains in the aggregates leads to an underestimation of the scattering intensity at high Q . Therefore, instead of simply using the form factor of a cylinder, the scattering of the mixed

aggregates according to Beaucage [29] is described as

$$\begin{aligned}
I_{\text{agg}}(Q) = & {}^1N_{\text{agg}} \int f(R, R_{\text{agg}}, \sigma) P_{\text{cyl}}(Q, R, \Delta SLD_{\text{agg}}, L_{\text{agg}}) dR \\
& + \text{erf}\left(\left(Q R_{\text{agg}} / \sqrt{12}\right)^2\right) \frac{\phi_{\text{PE}} x_{\text{PE}}}{\int f(R, R_{\text{PE}}, \sigma) V_p(R, L_{\text{PE}}) dR} \\
& \times \int f(R, R_{\text{PE}}, \sigma) P_{\text{cyl}}(Q, R, SLD_{\text{PE}} - SLD_{\text{surf}}, L_{\text{PE}}) dR \quad (5.2.4)
\end{aligned}$$

where the second term describes the scattering of the individual PE chains in the aggregates and the error function erf provides a cut-off towards low Q to avoid that the PE chains in the aggregates are counted twice when calculating the low Q scattering. The precise value of the cut-off has little influence on the outcome of the fit as long as it ensures that the intensity of the second term quickly vanishes when reducing Q below the first form factor minimum of the aggregates. The only free fit parameters are the radius and length of the aggregates R_{agg} and L_{agg} and x_{PE} . The scattering of the PE chains in the aggregates is slightly overestimated by assuming that the PE is entirely embedded in a surfactant matrix compared to a situation where the PE is at least partially exposed to the solvent surrounding the aggregate since ΔSLD between PE ($3.68 \times 10^{-4} \text{ nm}^{-2}$) and STS ($0.272 \times 10^{-4} \text{ nm}^{-2}$) is slightly larger than that between PE and D_2O ($6.33 \times 10^{-4} \text{ nm}^{-2}$) and for SDS/JR 400 it was found [125] that the PE chains are preferentially located on the outside of the aggregates where they are partially exposed to the solvent. Scattering from free PE is taken into account using eq. (B.2.1), expressing the volume fraction of the free PE through eq. (A.2.2) and the overall intensity is given by eq. (A.2.3).

The sample with $Z = 3$ exhibits a structure peak at low Q , see fig. 5.4, which makes it impossible to determine the length of the aggregates from the SANS data. The peak is described phenomenologically by multiplying eq. (A.2.3) with a Lorentzian:

$$I_{\text{S}}(Q) = I(Q) S_{\text{lor}}(Q) \quad (5.2.5)$$

with

$$S_{\text{lor}}(Q) = \frac{A_{\text{lor}} \sigma_{\text{lor}}}{(Q - 2\pi/R_{\text{lor}})^2 + \sigma_{\text{lor}}^2} + 1 \quad (5.2.6)$$

where A_{lor} represents the peak height, σ_{lor} is the width, and R_{lor} the peak position and for fitting L_{agg} is fixed at a value large compared to the minimal Q accessible. The fit results reveal that, as more surfactant is added to the sample, the aggregates grow slightly in length and the fraction of PE in the aggregates grows (see table B.1 and fig. 5.5). Assuming that the aggregates are homogeneous along their length, it is possible to estimate the number of PE chains per aggregate, see fig. 5.5, through eq. (A.2.5) here reported:

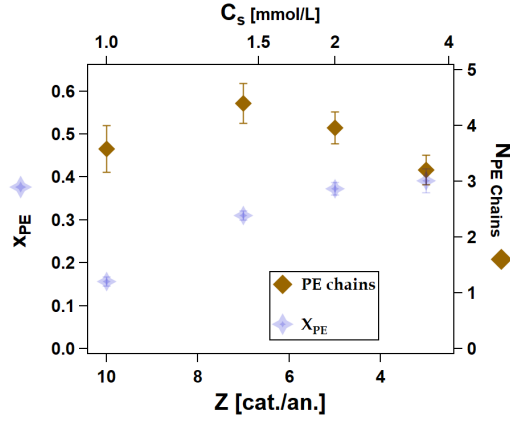


Figure 5.5: Fraction of PE in the aggregates x_{PE} , left axis. Average number of PE chains per aggregate, right axis. Both as a function of charges ratio (bottom) and STS concentration (top).

$$N_{PE \text{ chains}} = \frac{x_{PE} \phi_{PE} R_{agg}^2}{\phi_{agg} R_{PE}^2}. \quad (5.2.7)$$

It is found that $N_{PE \text{ chains}}$ is relatively constant with Z , see fig. 5.5. The numerical value, between 3 and 4, is comparable to what was reported earlier for SDS/JR 400 [125]. This result leads to the conclusion that the increase in viscosity for STS/JR 400 is due to the formation of aggregates interconnecting several PE chains, whereas the viscosity of SOS/JR 400 remains low because such aggregates are absent. Converting x_{PE} into the charge ratio of JR 400 and STS in the aggregates, C_{PE}/C_{STS} , reveals that the value is close to unity near the phase boundary and the neutral aggregates precipitate when further increasing the surfactant concentration, see fig. B.8. For $Z = 3$ a value of $R_{lor} = 80$ nm is obtained, which is on a similar order of magnitude as ξ estimated from rheology for the same sample, see table 5.1. From the discrepancy between those 2 values it is possible to make an admittedly crude estimate for the strength of the junctions: $g = (R_{lor}/\xi)^3 \approx 10^1$, which means that significantly more energy than $1 k_B T$ is needed to break a cross-link.

5.2.4 NSE

NSE measurements were performed to investigate the mesoscopic dynamics of mixed JR 400/surfactant systems. A preliminary analysis of the NSE data using eq. (2.4.1) reveals a linear increase of the apparent diffusion coefficient D_{app} with Q for pure JR 400, see fig. 5.6. While adding SOS has almost no effect on D_{app} , samples with STS show diffusive behavior ($D_{app} \propto Q^0$) for $Q < 1.1 \text{ nm}^{-1}$. For larger Q , D_{app} exhibits the same Q -dependence as for the pure PE. One may therefore assume that the diffusive behavior of JR 400/STS systems belongs to the PE/surfactant aggregates, while at higher Q the scat-

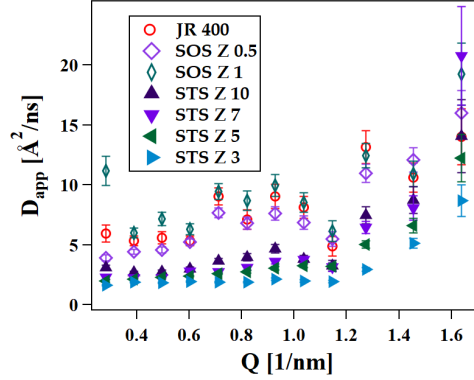


Figure 5.6: Apparent diffusion coefficient of 1 wt% JR 400 and mixtures of 1 wt% JR 400 and SOS or STS at charge ratios Z indicated in the graph.

tering signal is dominated by the free PE chains. SOS, on the other hand, does not form such aggregates and individual SOS molecules adsorbed onto the PE chains have only little influence on the behavior of the PE. These findings are fully consistent with the SANS results discussed before. Fitting the data for pure JR 400 using the model by Dubois-Violette and De Gennes [82] (see Appendix B, eq. (B.4.1) and fig. B.13 for details) yields good agreement. The parameters obtained in this fit are used in the following as fixed input parameters for the fits of mixed STS/JR 400 systems. $D_{\text{app}} \approx 2 \text{ Å}^2/\text{ns}$, as obtained for the samples containing STS, corresponds to a hydrodynamic radius of about 10 nm (see eq. (2.4.2)) or a length of about 50 nm using eq. (2.4.3) with a radius of 2 nm. This value is comparable to the size of the aggregates found in SANS and the mode is diffusive ($D_{\text{app}} \propto Q^0$) except at high Q where the scattering of the free PE becomes significant. The intermediate scattering function $S(Q, t)$ of mixed systems consisting of rod-like aggregates and free PE can be modelled as a linear combination of the intermediate scattering functions of diffusing rods ($S_{\text{rod}}(Q, t)$, see eq. (2.4.5)) and free polymer chains ($S_{\text{Zimm,D}}(Q, t)$, see eq. (B.4.4)):

$$S(Q, t) = \frac{1}{S(Q, 0)} \left(\frac{\phi_{\text{surf}} + x_{\text{PE}} \phi_{\text{PE}}}{V_{\text{agg}}} P_{\text{agg}} \cdot S_{\text{rod}}(Q, t) + \frac{(1 - x_{\text{PE}}) \phi_{\text{PE}}}{V_{\text{PE}}} P_{\text{PE}} \cdot S_{\text{Zimm,D}}(Q, t) \right) + S_{\text{el}}(Q), \quad (5.2.8)$$

where P_{agg} and P_{PE} are the form factors of the rod-like aggregates and the free chains, respectively, which are both known from SANS. $S_{\text{Zimm,D}}$ is known from fitting the NSE data of pure JR 400 solution and set constant for the fits of the samples with STS and JR 400. With that, the only unknown parameters are the length of the rod-like aggregates L and a weak Q -dependent elastic background S_{el} due to the formation of large clusters [127]. Upon parameter optimisation eq. (5.2.8) reproduces the experimental data reasonably well,

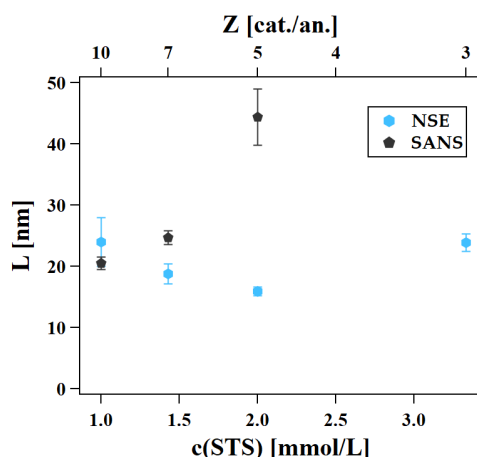


Figure 5.7: Values obtained for the length of the rodlike aggregates of STS/JR 400 (1 wt%) as a function of Z by NSE, see eq. (5.2.8), and SANS, see eq. (5.2.4); good agreement between both methods is obtained, the lengths are relatively constant with Z and the values are similar to those found for SDS/JR 400 and SDBS/JR 400 [125].

see fig. B.14 for an example. The lengths L obtained for small amounts of surfactant (high Z) are in good agreement with the values found by SANS, see fig. 5.7. While for $Z = 5$, SANS detects a significant increase of the length compared to smaller STS concentrations, the value obtained from NSE stays rather constant and even at $Z = 3$, where the length could not be measured by SANS due to the appearance of a correlation peak, NSE gives a value of only 24 nm. These findings suggest that the SANS measurement at $Z = 5$ might already be influenced by a correlation peak at low Q and the length of the rodlike aggregates remains constant with surfactant concentration. The lengths obtained here are about 10 nm shorter than those obtained for mixtures of JR 400, SDS and SDBS [123, 125] which seems surprising at first glance since STS should be able to form elongated aggregates more easily than SDS due to its smaller packing parameter [136]. However, no elastic contribution was included in the fits of the NSE data for SDS, which should lead to a longer apparent length of the aggregates. This also explains the longer length obtained from simply fitting eq. (2.4.1) and calculating the length with eq. (2.4.3).

5.2.5 MD Simulations

Building on earlier coarse-grained simulation studies [106, 268, 270, 271] and in order to gain complementary insights into the interaction of PE with monoalkylsulfate surfactants and the structures observed in the scattering experiments, atomistic molecular dynamics (MD) simulations were carried out as described in section 3.3.5.1. Apart from the surfactants (SOS, SDS, or STS), these simulations involve water molecules, ions, and either one stretched PE chain, which is quasi-infinitely long because of the periodic boundary condi-

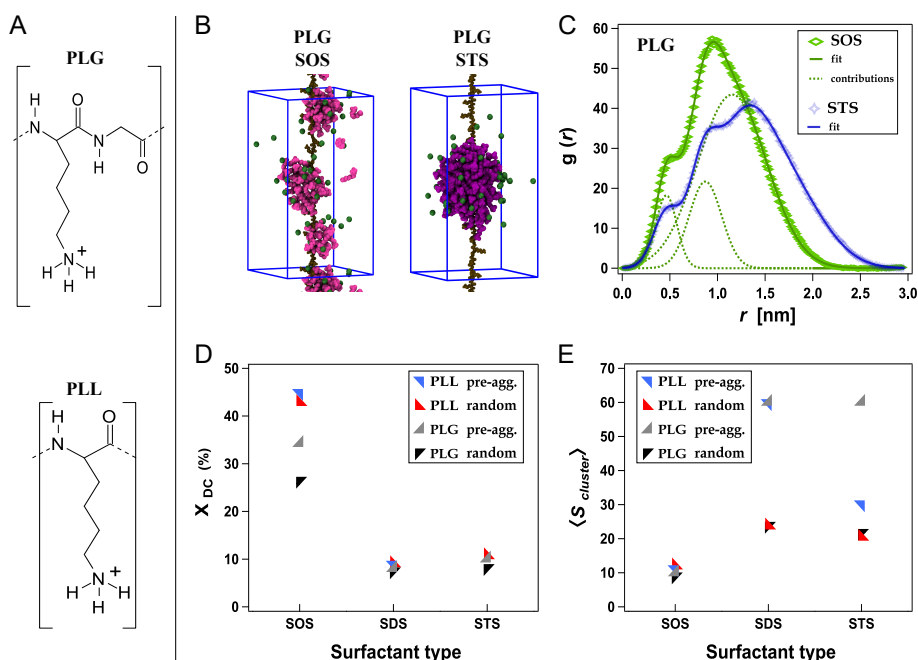


Figure 5.8: (A) Chemical structures of PLG and PLL. (B) Representative simulation snapshots of SOS (left) and STS (right) aggregates interacting with a single PLG chain. The simulation box is indicated with blue cuboids. (C) RDFs of SOS and STS methyl groups around PLG together with fits of a superposition of several Gaussian distributions (solid lines). Dotted lines indicate the contributions of individual Gaussian distributions. (D) Fraction of surfactants in direct contact with PLG and PLL backbone, x_{DC} . (E) Average size $\langle S_{cluster} \rangle$ of surfactant clusters attached to the PE chain for all PE types, surfactant types, and starting conditions.

tions, see fig. 5.8 B, or two such PE chains in a parallel configuration, see fig. 5.9 A. Note that the PE and surfactant concentrations in the simulation box by construction are not meant to correspond to their average concentrations in the experimental samples. For the PE chains, the positively charged polypeptides poly[lysine] (PLL) and poly[lysine-glycine] (PLG) were used, see fig. 5.8 A, which can be considered generic representations of JR 400, for which no validated force field has been available. PLL is highly charged (one positive charge per 0.36 nm) while PLG has a charge density comparable to that of JR 400 (one positive charge per 0.72 nm). The stretched configuration was chosen to represent the comparatively long persistence length of the PE used in the experiments, see above. Of primary interest were the structures of surfactant aggregates formed upon their interaction with a single PE chain, but also the structure of network-forming PESCs involving more than one PE chain. It must be emphasized that, for this purpose, good conformational sampling is essential. Results of simulations starting from pre-aggregated surfactant micelles are therefore compared with results of simulations in which the same number of surfactant molecules were initially randomly placed in the simulation box. Regarding the micelles, an aggregation number of 60 was used for all surfactant types. This choice was

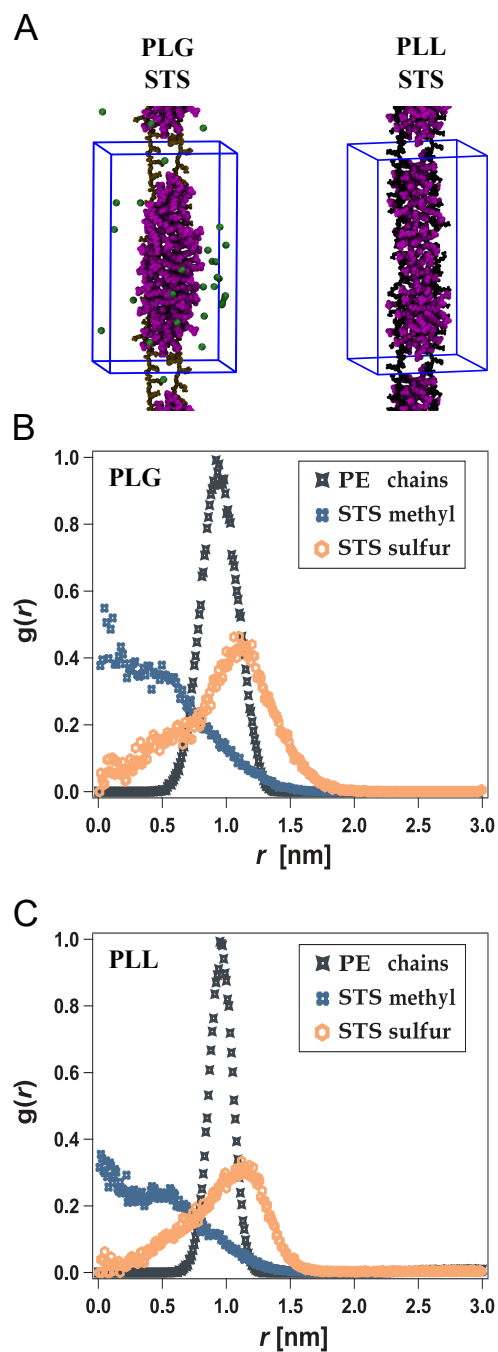


Figure 5.9: (A) Representative simulation snapshots of 60 STS molecules interacting with two parallel PE chains; left: PLG; right: PLL. (B and C) Cylindrical RDFs of STS sulfur, STS methyl, and PE backbone atoms around the aggregate's center of mass, for two PLG chains (B) and for two PLL chains (C).

made because 60 is a consensus number for SDS [41] and also roughly consistent with the size of STS micelles determined by SANS in the present study, see fig. B.5. For SOS the initially assumed aggregation number is less relevant because the aggregates rapidly reorganise due to the comparatively high solubility of SOS. Since it is difficult to predict the local ion concentration in the surroundings of a PESC, it is useful to compare the standard low-salt simulation scheme (minimum counter-ions, where ions are merely added to achieve overall neutrality of the simulated system) with an alternative high-salt scenario (detailed counter-ions, where a counter-ion is added for each charged group). Depending on the PE to surfactant charge ratio in the simulation box, this high salt scenario corresponds to NaCl bulk concentrations of $\approx 125 - 500$ mM. As shown in Appendix B, see fig. B.17, the influence of the salt concentration is minor or at most moderate. In the following, it is therefore limited the presentation of the results obtained under conditions of minimum counterions, which are considered somewhat more applicable with respect to the experimental situation.

5.2.5.1 Surfactants Interacting with a Single PE Chain

Figure 5.8 B shows representative snapshots of SOS (left) and STS (right) aggregates interacting with stretched PLG, for PLL see fig. B.18. Top views of the snapshots along the PE axis are shown in fig. B.21. It is seen that the surfactant aggregates are firmly attached to the oppositely charged PE chain. Although in both cases the initial configuration has been a single pre-arranged micelle separated from the PE chain, a qualitatively different configuration is established for the different surfactant types after equilibration. While SOS splits up in numerous small aggregates along the PE, STS (and SDS, see fig. B.16) remain rather spherical upon adsorption to the PE. To analyze the organization of the three surfactant types around the PE chains in a quantitative manner, radial distribution functions (RDFs) of the surfactants' methyl and sulfur groups around the PE backbone in a cylindrical geometry were computed. In fig. 5.8 C the result is shown exemplarily for SOS and STS methyl groups around PLG. It can be seen that the distribution of methyl groups is much more narrowly distributed for SOS than for STS (and SDS, not shown). Closer inspection reveals that the distributions exhibit three distinct maxima. The first two of them (at $r \approx 0.5$ nm and at $r \approx 0.9$ nm) are associated with surfactants that are in direct contact with the PE, either through hydrophobic or electrostatic interaction. Fitting the distributions with a superposition of several Gaussian distributions allows quantification of the fraction x_{DC} of surfactants in direct contact with the backbone. Here, x_{DC} is defined as the area under the first two Gaussian distributions divided by the area under the entire distribution. In fig. 5.8 D, x_{DC} is shown for all surfactant types, PE types, and starting conditions (pre-aggregated or randomly placed surfactants). Clearly, x_{DC} is much higher

for SOS than for the two longer-tail surfactants, reflecting that SOS adsorbs in the form of individual molecules rather than as large aggregates, in good agreement with the SANS analysis. The fact that SOS aggregates of considerable size nonetheless exist in the simulations, see again fig. 5.8 B, must be attributed to the much higher local SOS concentration in the simulations compared to the experimental situation.

Another way of looking at the surfactant distribution around a single PE chain is quantifying the average size $\langle S_{\text{cluster}} \rangle$ of surfactant clusters, i.e., the average number of surfactants in contiguous groups with direct contact. Here, two surfactant molecules were considered in contact if the shortest distance between any of their constituent atoms is below 0.44 nm (see Appendix B, fig. B.15 for a justification of this choice). In fig. 5.8 E, $\langle S_{\text{cluster}} \rangle$ is shown for all surfactant types, PE types, and starting conditions. Again a clear trend is observed: while the longer-tail surfactants SDS and STS interact with the PE mainly in the form of only one or two well-defined large clusters, SOS forms many small clusters distributed along the PE. The known high CAC of SOS is also manifest in the simulations, as seen from a considerable number of clusters of size 1 in the size distributions shown in fig. B.20. Note that the fixed finite number of surfactants in the simulation box for approximately equal-sized clusters only allows for a discrete cluster size associated with each integer number of clusters. Due to this finite-size effect, the obtained cluster numbers and sizes should be interpreted on a qualitative level only. At this point it should also be noted that the details of this analysis are limited by the configurational sampling, especially for the longer-chain surfactants, because aggregate breakup and fusion is associated with considerable free energy barriers. This conclusion follows from the observation that $\langle S_{\text{cluster}} \rangle$ exhibits some dependence on the starting configuration (pre-aggregated or randomly placed surfactants) when the average is taken over simulation times of the order of 100 ns, see fig. 5.8 E. Even though some transitions in the cluster number and size take place also on the probed time scales, much longer simulation times would be required to fully exclude the influence of the starting configuration. Nevertheless, because large average cluster sizes in are obtained for SDS and STS irrespective of the extremely different starting configurations, the trend regarding the influence of the tail length can be considered robust. It is seen to be independent of the PE charge density and consistent with the SANS analysis.

5.2.5.2 Surfactants Interacting with two Parallel PE Chains

To explore the formation and structure of PESCs involving more than one PE, as seen by SANS for STS in the present work, simulations with two parallel stretched PLG or PLL chains were carried out. The two chains are free to diffuse along the xy -plane and exhibit overall repulsive interaction in the absence of the surfactants due to electrostatic repulsion,

see fig. B.19. In the presence of STS and irrespective of the initial configuration (pre-aggregated or randomly placed surfactants) large elongated aggregates involving both PE chains and all surfactant molecules, see fig. 5.9 A, are rapidly formed. In other words, the PE chains are essentially "glued" together by aggregated oppositely charged surfactants, resulting in PESCs, in agreement with the experimental observations. Interestingly, only one single STS cluster is always formed independent of the PE type and of the initial configuration (pre-aggregated or randomly placed surfactants), suggesting that the presence of an additional PE chain catalyses aggregate fusion and thereby speeds up the formation of an equilibrated conformation. The structural details of the formed PE/STS aggregates are nearly independent of the PEs' charge density, as exemplified by the cylindrical RDFs of STS sulfur, STS methyl, and PE backbone atoms around the xy -projection of the aggregate's center of mass, presented in fig. 5.9 for two PLG chains (panel B) and for two PLL chains (panel C). The fact that there are hardly any differences in the RDFs of PLL and PLG justifies the at least qualitative comparison between the experimental results from SANS and NSE on one side and the MD simulations on the other side. While the radii of the aggregates obtained from MD and SANS are quantitatively different (≈ 1.5 nm in MD as opposed to ≈ 2 nm from SANS) there is qualitative agreement in the sense that in both cases the small radii suggest a strongly interdigitating structure of the surfactant tails because radii significantly above 2 nm were found even for simple SDS micelles [44, 119] with 2 carbon atoms less than STS and simple STS micelles show a radius of 2.1 nm, see fig. B.6, even without the bulky JR 400 chain. Comparing the RDFs of the PE chains to those of the sulfur atoms, see fig. 5.9, panels B and C reveals that the PE chains are penetrating deeply into the surfactant core of the aggregates in agreement with the SANS data and as observed previously for SDS/JR 400 [125]. The MD simulations might provide an explanation for both these findings on a molecular level. The fact that both electrostatic contacts (surfactant head on PE) and hydrophobic contacts (methyl group on PE) coexist might impose both a strongly interdigitating structure of the surfactant chains and results in strong intermixing of the PE chains with the surfactant tails in the aggregate. The quantitative difference in the radii from SANS and MD may be either due to the JR 400 chain being bulkier than PLG and PLL or due to the MD simulations overestimating the number of direct contacts between the PE and the surfactant methyl group, which would mean that JR 400 is less hydrophobic than the model PEs used in the MD simulations.

5.3 Conclusions

By combining rheology, SANS, NSE, and MD simulations aqueous solutions of the cationic cellulose-based polyelectrolyte JR 400 and the anionic surfactants SOS and STS at vari-

ous charge ratios Z have been investigated. While STS/JR 400 upon increasing the surfactant concentration starts precipitating around charge equilibrium ($Z = 1$), phase separation only occurs at higher surfactant concentrations (lower Z) for SOS/JR 400, see fig. 5.1. SANS measurements show that this is due to the high CAC of SOS, see fig. 5.3. STS/JR 400 solutions exhibit a pronounced increase of viscosity near the phase boundary in PE excess by almost four orders of magnitude relative to the pure JR 400 solution, see fig. 5.1. SANS measurements show that the increase in STS/JR 400 is due to the formation of mixed rod-like aggregates, similar to those formed in SDS/JR 400 [125]. The viscosity of SOS/JR 400 remains almost constant and no such aggregates can be observed in SANS, see fig. 5.2. The STS/JR 400 aggregates have a radius of about 2 nm, see table B.1, they incorporate 3 to 4 PE chains on average, see fig. 5.5, which is similar to SDS/JR 400 but slightly less than in SDBS/JR 400 (4 to 5) [125]. The observation that STS/JR 400 is significantly more viscous than SDS/JR 400 at the same Z (e.g., 60 Pas vs. 3 Pas at $Z = 3$) despite the same number of PE chains bound, implies that hydrophobic interactions between surfactant molecules determine the viscosity of the system. To gain further insights into the PESC's mesoscopic structure, MD simulations were performed with SOS, SDS and STS as surfactants and PLG and PLL as generic PEs with different charge densities. The fraction of surfactants in direct contact with a single stretched PE backbone is found to be significantly higher for SOS than for STS and SDS, see fig. 5.8 D, suggesting that the shorter-tail surfactants adsorb on the PE as individual molecules rather than in the form of large aggregates, which is in agreement with the SANS results. While PESC's can on average comprise a different number of surfactants than imposed in the simulations, robust qualitative conclusions can nevertheless be drawn: The consumption of all available surfactants into one continuous PESC for STS indicates the formation of extended PESC's, in line with the experiments for this surfactant. In contrast, the split up of the aggregates in many small clusters for SOS indicates that this surfactant gets more dispersed along the PE, in line with the experiments. Simulations involving two parallel stretched PE were performed to qualitatively mimic PESC's comprising more than one PE. For both PLL and PLG, i.e., independently of the PE's charge density, large elongated STS aggregates are formed which firmly interconnect the PE chains, in agreement with the SANS analysis. The cylindrical RDFs of the PE chains around the aggregate's centre of mass exhibit relatively broad peaks which means that the PE chain penetrates deeply into the hydrophobic surfactant core. This is even more true for PLG, see fig. 5.9 B and C, which has a comparably low charge density, as JR 400. This result is in good agreement with the SANS data of STS/JR 400 in this article and SDS/JR 400 [125] which show that no pronounced core-shell structure exists in the aggregates. In summary it has shown that the increase in viscosity in PESC's is related to the formation of bridging aggregates which

are present in PESCs with surfactants with sufficiently long tails (C_{12}, C_{14}) while no such aggregates form with short tail surfactants (C_8). The good qualitative agreement with MD simulations demonstrates the potential of experiment/simulation combined investigations for the rational design of PESC formulations.

Chapter 6

Stimuli-Responsive PESCs for the Reversible Control of the Solution Viscosity

This chapter is based on the text of the submitted manuscript¹.

6.1 Introduction

From what has been stated in previous chapters, it is evident that PESCs can be used to tune the rheological properties of aqueous solutions in which they are present. In particular in chapter 5 it has been shown that for JR 400/alkyl surfactants mixtures high viscosity coincides with the presence of rod-like mixed aggregates that are only formed when the surfactants have long-enough alkyl tails (C_{12} or C_{14}) and are thus sufficiently hydrophobic, in line with earlier reports on C_{12} surfactants [55, 125, 126, 128]. Specifically, from these mixed rod-like aggregates depend the viscoelastic properties of the solutions. Like PESC solutions, also worm-like micelle (WLMs) can exhibit viscoelastic behavior [35, 47, 79, 228, 250, 287]. Under certain conditions, WLMs can form an entangled network leading to increased zero-shear viscosity and shear thinning behavior [3, 61, 293]. These supramolecular structures have earned the name *smart* WLMs since they are able to change their properties in response to external stimuli, such as UV/visible light, temperature changes, or pH variations [148, 175]. Similarly, smart polymeric materials have

¹Stimuli-Responsive Polyelectrolyte Surfactant Complexes for the Reversible Control of Solution Viscosity

gained enormous interest due to their potential in micro-electromechanical or optical applications, as coatings, or for drug delivery and biosensing [177, 251]. A wide range of different stimuli responsive polymers can be synthesised [255, 275], among them the thermoresponsive poly(N-isopropylacrylamide) (PNIPAM) [4, 142, 154, 285] which has a lower critical solution temperature (LCST) close to body temperature [207, 231, 251] making it particularly interesting for drug delivery. However, smart materials based on either WLMs or polymers alone suffer from distinct disadvantages. Polymeric materials require custom synthesis, while for WLMs relatively high surfactant concentrations, typically in excess of 10 mM [159], 30 mM [46, 64], 40 mM [234, 260] or even 60 mM [215] are used to significantly increase the solution viscosity. While this does not pose a problem as long as standard surfactants, such as hexadecyltrimethylammonium bromide (CTAB), but can become problematic if large quantities of a rather exotic stimuli responsive surfactant are needed. In contrast, PESCs with stimuli-responsive surfactants should offer a possibility to avoid these shortcomings. Viscous PESCs can use polymers that are commercially available in large quantities such as JR 400, see fig. 3.1. And PESCs based on this polymer have previously been shown to increase the solution viscosity by two-three orders of magnitude by adding as little as 2 mM of surfactant [73, 100, 125]. Finally, surfactants sensitive to external stimuli such as temperature [95, 202, 249], light [54, 266], or pH [30, 58, 277] are nowadays available. In principle, they allow to impart their stimuli responsiveness on polymeric systems as demonstrated for PNIPAM microgels and polyelectrolytes with photo sensitive azobenzene-containing surfactants [289, 290]. Here, mixtures of JR 400 with the pH-sensitive surfactant sodium mono dodecyl phosphate (SDP), see fig. 3.2, are analyzed. The surfactant ionic groups can be protonated or deprotonated by changing the solution pH, which offers the unique possibility to tune the self-assembly of PESCs. For details on its pH-dependence see Appendix C, section C.1.

To investigate the changes of the mesoscopic structure and dynamics associated to pH variations at different PE/surfactant charge ratios, Z , rheology, SANS and NSE measurements were performed. It has been found that PESCs with SDP^- form mixed rodlike PE/surfactant aggregates, which interconnect on average 3 PE chains, thereby increasing the system's viscosity. These aggregates are dissolved when increasing the pH enough to obtain SDP^{2-} and consequently the viscosity is reduced.

6.2 Results and Discussion

SANS experiments are detailed in section 3.3.3. Rheology and NSE measurements in section 3.3.2 and section 3.3.4 respectively.

Sample preparation is illustrated in section 3.2.

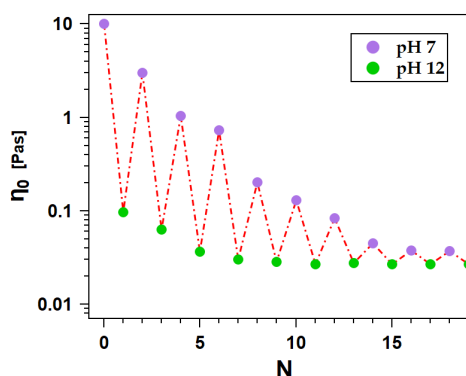


Figure 6.1: Zero shear viscosity η_0 of SDP as function of the solution pH. Adding either HCl or NaOH the solution pH was changed between 7 and 12 for a certain number of cycles, N .

6.2.1 Rheological behavior

As already demonstrated for the effect of surfactant tail length [73], also the charge of the head group plays a crucial role for the macroscopic flow behavior of PESCs. In alkaline solution where the surfactant is double-charged, samples exhibit simple Newtonian behavior with a viscosity comparable to that of the pure JR 400 solution, while PESCs with SDP^- show a remarkable increase in viscosity. As seen in the flow curves of PE/SDP^- , see fig. C.3, solutions are shear-thinning. Shear-thinning starts at a critical shear rate $\dot{\gamma}_{\text{crit}}$ which decreases with decreasing Z (increasing the SDP^- concentration), similar to what was observed in PESCs with JR 400 and SDS or sodium dodecyl benzenesulphonate (SDBS) [125, 128] which both have a single negative charge. For JR 400/SDS, it was found that the shear-thinning is related to a slight alignment of mixed PE/surfactant aggregates [74]. The zero-shear viscosity, η_0 , of the system, see fig. C.2, increases by three orders of magnitude relative to the pure JR 400 solution when adding 5 mM SDP^- ($Z = 2$) and the structural relaxation time τ_{cross} seen by oscillatory measurements, see fig. C.4, increases by two orders of magnitude when increasing the surfactant concentration from 1.4 mM to 5 mM (decreasing Z from 7 to 2), as found in previous works [124, 126, 144, 265]. Figure 6.1 shows the zero shear viscosity of a sample at $Z = 3$ where the solution pH was changed back and forth multiple time between 7 and 12 by adding concentrated NaOH or HCl. It is possible to switch between high and low viscosity almost instantaneously. The switching process can be repeated about five times before the viscosity at low pH decreases by a factor 10 relative to the initial solution. This decay is presumably due to gradual chemical decomposition of the compounds under harsh basic conditions.

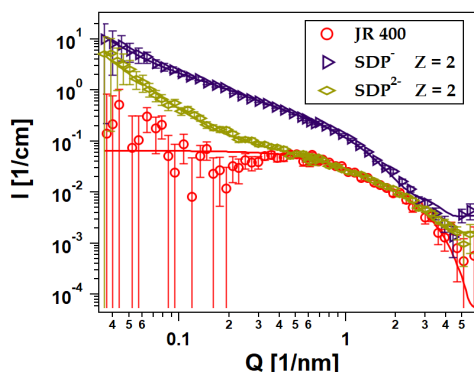


Figure 6.2: Comparison of the SANS curves of 1 wt% JR 400 with SDP^- and SDP^{2-} , both at charge ratio $Z = 2$ and pure JR 400. While the curve of $\text{SDP}^-/\text{JR 400}$ shows the formation of rodlike aggregates, hardly any structural changes compared to the pure PE can be seen for $\text{SDP}^{2-}/\text{JR 400}$.

6.2.2 Mesoscopic Structure and Dynamics

Having shown that PESCs with SDP can be used as stimuli responsive materials changing the solution viscosity with pH, in the following it is elucidate the mesoscopic structure and dynamics of these systems at both high and low pH using SANS and NSE.

SANS and NSE measurements on samples with 1% of JR 400 and various surfactant concentrations were performed in order to elucidate the changes in the mesoscopic structure that occur upon pH variation. Based on previous studies [73, 123, 125] the scattering curve of JR 400 is described with the form factor of small rods with a radius, R_{PE} , of 0.8 nm and a length, L_{PE} , of 6 nm, as shown in section 5.2.3. Figure 6.2 shows a comparison between the SANS curves of solutions of JR 400/SDP at the same surfactant concentration, namely 5 mM ($Z = 2$) at different pH and the scattering curve of the pure JR 400 solution. It can be seen that at high Q ($Q > 0.5 \text{ nm}^{-1}$) the scattering curves for pure JR 400 and the PESC at pH 12 where SDP bares 2 negative charges are almost identical while the PESC at pH 7 shows a significant increase in scattering intensity. At $Q < 0.5 \text{ nm}^{-1}$ both PESCs show an increase in scattering intensity relative to the pure JR 400 solution, partly because of some insoluble surfactant dimers and partly because of larger clusters [128]. Figure 6.3 shows a gradual increase of the high Q scattering intensity with surfactant concentration, which implies that the extra scattering intensity is due to surfactant aggregates that form at pH 7. At pH 12, the high Q scattering intensity remains almost unchanged and only at low Q an increase of the scattering intensity due to the presence of some insoluble surfactant dimers is observed, see fig. C.6. The fact that there is no change in scattering intensity at high Q for samples with SDP^{2-} means that the double-charged surfactant does not form aggregates and if it absorbs on the PE it only does so in the form of single molecules. The apparent diffusion coefficient D_{app} , see fig. 6.4, of the pure JR 400 solution determined

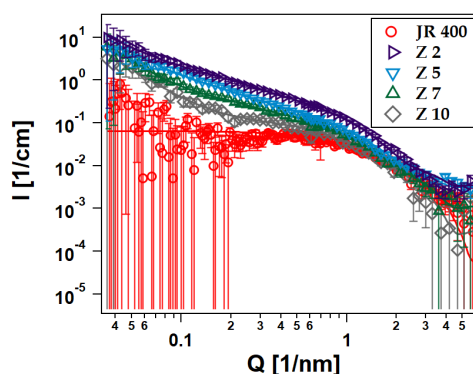


Figure 6.3: Comparison of the SANS curves of 1 wt% JR 400 with SDP^{2-} at different Z values and pure JR 400. Rising the surfactant concentration (i.e., reducing Z), an increasing of the scattering intensity is observed at high- Q , because of the mixed aggregates.

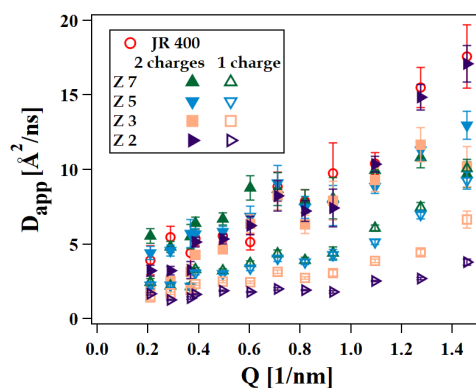


Figure 6.4: Apparent diffusion coefficient obtained from fitting eq. (2.4.1) to the NSE intermediate scattering functions of pure JR 400 and PESCs with SDP^{2-} (closed symbols) and SDP^{2-} (open symbols) at different surfactant concentrations; while SDP^{2-} has only rather little influence on D_{app} , addition of SDP^{2-} results in the formation of a slower diffusive mode due to the formation of aggregates.

from NSE shows a linear increase with Q as expected for a polymer in solution. Addition of SDP^{2-} has hardly any effect on D_{app} while addition of SDP^{2-} results in the emergence of a slow diffusive component at $Q < 1 \text{ nm}^{-1}$, due to the surfactant aggregates already observed in SANS. The observations made by SANS and NSE are qualitatively similar to what has been found for PESCs with JR 400 and either the relatively hydrophobic surfactant STS or the less hydrophobic SOS [73], see chapter 5. Therefore, PESCs with SDP^{2-} which form aggregates are fitted with the same procedure that was used there. The kink in the scattering curves at about 2 nm^{-1} indicates a radius of the cylindrical aggregates of $R_{\text{agg}} \approx 1.6 \text{ nm}$, which is similar to that of JR 400/SDS complexes [123–125]. All the curves show a strong increase in intensity at $Q < 0.1 \text{ nm}^{-1}$ due to the presence of both a small quantity of non-dissolved material and large scale clusters [128]. The data can be modelled as a superposition of free PE (I_{PE}), aggregates (I_{agg}) and a power law (I_{power}) to

take into account the intensity increase at low Q , so that:

$$I(Q) = I_{\text{agg}}(Q) + I_{\text{PE}}(Q) + I_{\text{power}}(Q) \quad (6.2.1)$$

The free PE is modelled as thin cylinder, see eq. (B.2.1), with the same size as found for the pure PE. The macroscopic volume fraction of surfactant in solution, ϕ_{surf} , is not sufficient to account for the volume fraction of the aggregates ϕ_{agg} , whose value is given by eq. (A.2.1) (the aggregates consist of both surfactant and PE) and the volume fraction of free PE reduces to eq. (A.2.2).

From the fits it can be deduced that the aggregates have a radius of $R_{\text{agg}} \approx 1.6$ nm independent of the surfactant concentration. With increasing surfactant concentration more PE is incorporated in the PE/SDP⁻ complexes, see fig. C.7. Assuming a homogeneous composition along the long axis of the rodlike aggregates, eq. (A.2.5) can be used to calculate the number of PE chains in an aggregate (see fig. C.7, right axis) and it can be seen that the aggregates contain roughly 3 PE chains, so that the aggregates interconnect PE chains and are responsible for the macroscopically observed increase in viscosity, similar to what was found for SDS/JR 400 [125] and STS/JR 400 [73]. The length of the aggregates cannot be determined from SANS as the power law scattering at low Q covers the low Q part of the aggregates from which the length could be deduced. However, this information can be obtained from NSE by identifying the diffusive mode that was observed in samples with SDP⁻ as the diffusion of the rodlike aggregates. Modelling of the intermediate scattering function is done as a superposition of rodlike aggregates, free PE and an elastic contribution (see eq. (5.2.8) and figs. C.8 to C.10). The length of the aggregates and the elastic contribution S_{el} are the only free parameters and the lengths obtained for the aggregates are on the order of 15 nm, see fig. C.11.

For more details on SANS and NSE data treatment, see Appendix C, section C.3.1 and section C.4.1.

6.3 Conclusions

Here, it has been shown that by combining the pH-sensitive surfactant SDP and the polyelectrolyte JR 400 it is possible to control the solution viscosity by adjusting its pH. While hardly any increase in viscosity upon surfactant addition is observed at pH 12, where SDP bares 2 charges, an increase by up to three orders of magnitude relative to the pure JR 400 solution is observed at pH 7 where SDP has only a single charge. Using SANS and NSE it is found that the increase in viscosity at pH 7 is due to the formation of mixed, rodlike PE/surfactant aggregates which interconnect approximately 3 PE chains on average. These

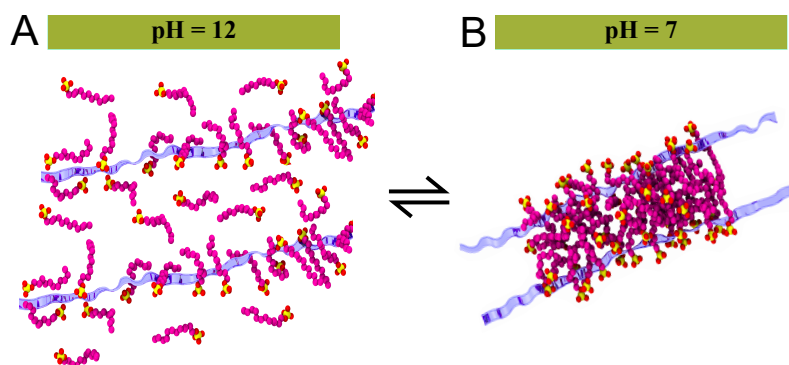


Figure 6.5: Schematic description of the pH effect on the SDP/JR 400 solution viscosity. At pH 12 (A) the surfactant bears 2 charges, adsorbing on the PE chains as single molecules. At pH 7 (B) SDP has only a single charge, leading to the formation of mixed, rodlike PE/SDP[−] aggregates.

aggregates are dissolved at pH 12, where the surfactant is less prone to aggregate due to the second headgroup charge, see fig. 6.5.

While the system SDP/JR 400 is of limited practical use due to the relatively small number of times it can be switched back and forth, it nicely demonstrates the feasibility of a modular approach to stimuli responsiveness. The bulk of the system consists of the commercially available PE JR 400, which is not pH-responsive but has a tendency to increase the viscosity of solutions when mixed with small amounts of negatively charged surfactant. The responsiveness comes from a small amount of surfactant which can in principle be exchanged for another surfactant which reacts to another stimulus such as light or temperature, so that it becomes easy to create tailor-made stimuli-responsive solutions.

Chapter 7

Mechanical Stability of Mixed Aggregates

In the previous chapters, the presence of rod-like mixed PE/surfactant aggregates was found to be correlated with a high viscosity of PE/surfactant mixtures. This correlation was attributed to the formation of PE networks in which individual PE chains are cross-linked or “glued together” by the mixed aggregates.

In the following, constant-force pulling (CFP) MD simulations are used to take a closer look at the capability of such aggregates of keeping two PE chains bound together. CFP is one of the basic techniques of steered molecular dynamics simulation, a method for studying force-induced response in a given system . For this purpose, CFP MD simulations are employed in order to mechanically challenge the stability of the bond.

The pulling simulations carried out in this thesis are performed by applying a constant force between the center of mass (COM) of two stretched PE chains which are pulled away from each other. In the parallel geometry, see section 3.3.5.2, the two PEs are free to diffuse along the z -direction of the simulation box, see fig. 7.1 A, with the applied constant force pulling in the xy plane. In the orthogonal geometry the PE chains are extended along x and y direction of simulation box, see fig. 7.1 B, with the applied constant force pulling only along the z -component. In both cases the starting configuration of the CFP is obtained as the output of a classical MD simulation (whose protocol is described in section 3.3.5.1), starting from pre-aggregated micelle and detailed counterions where the used model for JR 400 is the positively charged PLL, see fig. 5.8 A. It should be considered that the parallel geometry is probably the closest scenario to what is seen in SANS. However, under sufficient tension most of the parallel PE chains turn into non parallel configurations.

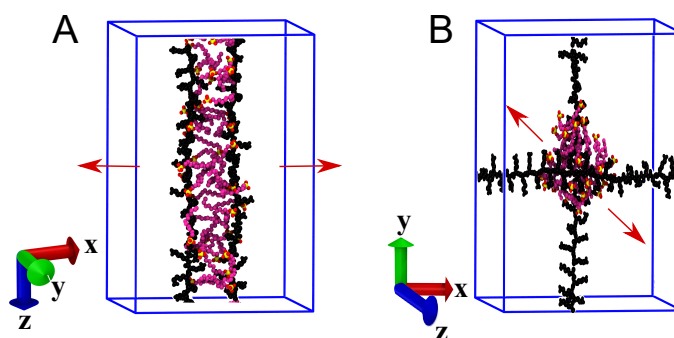


Figure 7.1: Different pulling geometry of two PLL chains. PLL chains in parallel (A) and orthogonal (B) configuration. Red arrows indicate the direction of the pulling force.

To quantify the PE chains distance at each pulling force, the Gromax tool *gmx - distance* has been applied to the CFP trajectories, calculating as function of time the gap between PEs center of mass in the *xy* plane and in *z* for parallel and orthogonal pulling, respectively. To better evaluate the response of the system to the pulling forces, a wide range of forces has been applied, ranging from 10 kJ/(mol nm) to 150 kJ/(mol nm) which corresponds to cover forces from 16.61 pN to 249.15 pN.

Figure 7.2 shows exemplarily the time evolution of the distance between two orthogonal PE chains for selected pulling forces and both surfactants. In the absence of force ($F = 0$) the distance between PE chains is larger in presence of STS than in presence of SOS. This result reflects a different tendency of the surfactants in distribution in the system. While the shorter tail surfactant is more distributed along the two PEs, STS aims to be preferentially located in the contact point. From fig. 7.2 is also possible to detect the effect of the different applied forces on the system:

- with a moderate force in the first couple of nanoseconds the distance saturates and fluctuates around a plateau value until the end of the simulation. This plateau value increases systematically with the force. An example is given by $F = 50$ kJ/(mol nm) and $F = 80$ kJ/(mol nm) in fig. 7.2 C and D;
- in parallel geometry at the highest applied force a plateau is reached before 20 ns but after the breaking occurs (which can be assumed to be stochastically distributed) as seen for $F = 150$ kJ/(mol nm) in fig. 7.2 A and B ;
- in orthogonal geometry when the highest force is applied the distance increases rapidly and diverges (immediate rupture), as for $F = 60$ kJ/(mol nm) and $F = 100$ kJ/(mol nm) in fig. 7.2 C and D.

In all CFP simulations the stability of the system is arbitrarily defined as "bond survival over 100 ns". In general, this choice is not unique, but nevertheless useful for an investi-

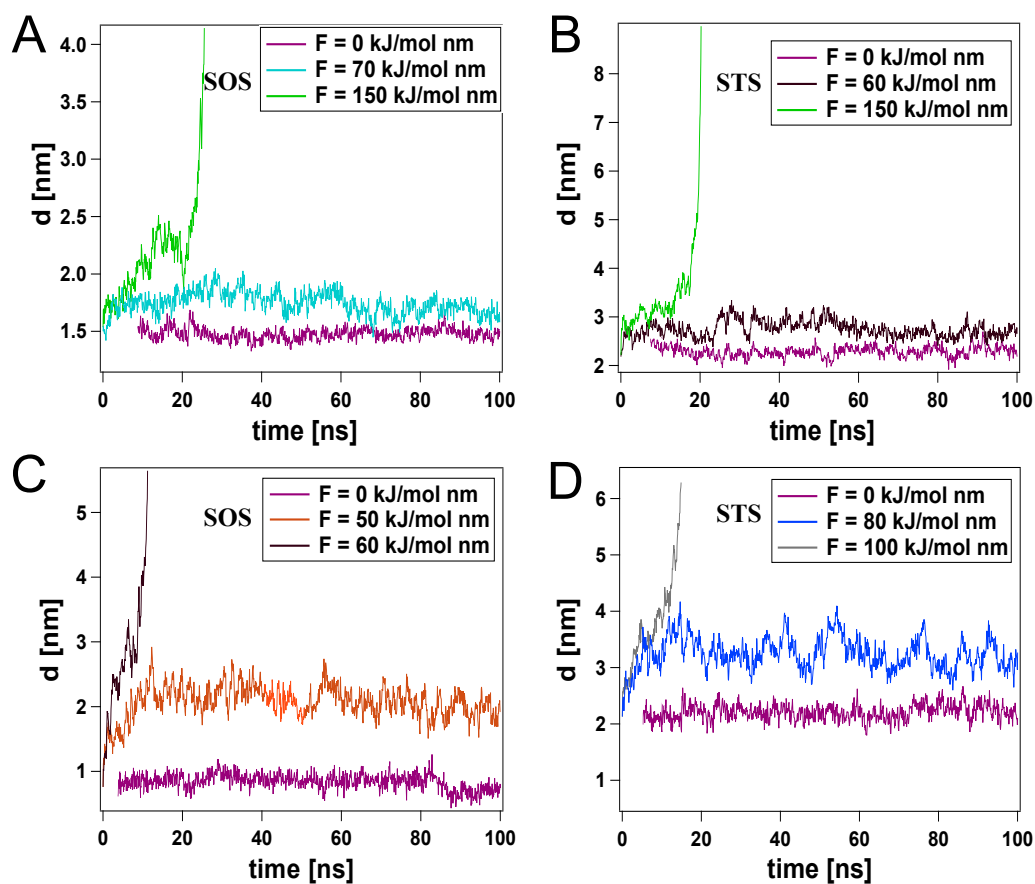


Figure 7.2: Top panel: PE-PE distance in parallel geometry over the simulation time at specific pulling forces applied, for PE/SOS (A) and for PE/STS (B). Bottom panel: PE-PE distance in orthogonal geometry over the simulation time at specific pulling forces applied, for PE/SOS (C) and for PE/STS (D)

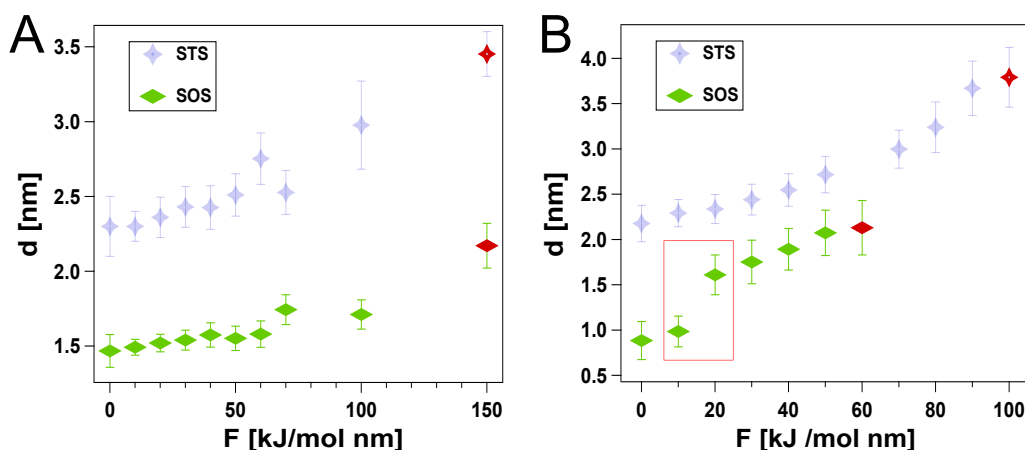


Figure 7.3: Distance between the PLL chains as function of the applied pulling force for parallel (A) and orthogonal geometry (B). Red symbols indicate the distance when the breaking of surfactant bridge between PLL chains occurs. Green rectangle in (B) underlines the shape transition that SOS undergoes above a critical pulling force: above $F > \sim 10$ kJ/(mol nm) SOS is mostly located at the contact point between PEs rather than distributed along them, resulting in a similar configuration generally preferred by STS and determining a jump of the distance.

gation of qualitative trends. Here it was dictated by practical reasons, like MD accessible time and length scales. Ideally one should perform several independent repetitions for all CFP simulations, because rupture events are stochastic processes. But this is currently computationally still almost unaffordable. However, already one run per force is suitable to roughly estimate the maximum force that can be sustained over 100 ns, because rupture rates are well known to have a highly non-linear force dependence [141]. Either way, a possible manner to improve the stability characterization could be to perform force-ramping simulation and applying Bell-Evans theory to obtain barrier height and critical breaking length [32, 87, 224].

In fig. 7.3 is shown the trend of the time-averaged distance (calculated within the plateau of distance vs time) between the PE chains, for both PE/SOS and PE/STS in parallel (A) and orthogonal (B) geometry, as a function of all the constant forces applied. For both surfactants and geometries is registered an increase of the plateau distance with increasing applied force. Red symbols correspond to simulations at maximal pulling force, F_{\max} , where rupture occurred after an initial plateau but within 100 ns. With parallel PE chains F_{\max} is similar for both surfactants since even SOS can glue the two PEs together with many small aggregates along the linear contact zone between them. Differently, in the orthogonal scenario F_{\max} is significantly higher for STS than for SOS, see table 7.1. This difference occurs because in the latter the contact zone is quasi-point-like, also one large and strongly cohesive aggregate is more stable and it can involve larger parts of the oppositely-charged PE chains. Another important aspect of the stability is the maximal extension between PE

Table 7.1: CFP parameters for PE/SOS and PE/STS in both geometries.

	PARALLEL	ORTHOGONAL
F_{\max} SOS [kJ/(mol nm)]	150	60
F_{\max} STS [kJ/(mol nm)]	150	100
Δd_{\max} SOS [nm]	0.7	1.24
Δd_{\max} STS [nm]	1.15	1.62
E_b SOS [kT]	25.4	10.6
E_b STS [kT]	40	35.2

chains, $\Delta d_{\max} = d(F_{\max}) - d(F = 0)$, see again table 7.1. For both configurations Δd_{\max} is higher for STS than for SOS because the former forms larger aggregates which are also more deformable before rupture.

Another way of estimating the surfactant gluing capability is to consider the binding energy, E_b , of both systems. E_b is estimated considering the work, W , required to break the PE-PE connection, that is:

$$W = \int_0^{\Delta d_{\max}} F(\Delta d) d\Delta d \quad (7.0.1)$$

with $\Delta d = d(F) - d(F = 0)$. In this analysis the W values were obtained from numerical integration of the linearly interpolated $F(\Delta d)$ curves, represented in fig. 7.4, where W is graphically represented by the areas under curve. Comparing the two geometries, it can be noticed that for parallel PEs the areas under curve are rather similar for SOS and STS, while for orthogonal chains PE/STS shows a significantly higher area compared to PE/SOS. This results in higher difference of E_b values between the two surfactants in orthogonal geometry, being E_b of STS increased by a factor three from that of SOS, see table 7.1, following directly from higher F_{\max} and Δd_{\max} .

For what has been stated above the orthogonal case turns out to be more relevant, because:

- for a random encounter of two vectors the probability density goes as $\sin \theta$, which means that higher angles have higher contribution;
- the contact zone is essentially point-like already for small angles.

At this point, it can safely said that CFP simulations clearly indicate that STS should lead to much more stable and stronger networks, in line with the experimental observation.

Further information on the rupture process can be extracted looking at the representative simulation snapshots of aggregates rupture, see fig. 7.5 for parallel and fig. 7.6 for orthogonal geometry. The breaking of the surfactant bridge as force-induced response occurs rather symmetrically for both SOS and STS, resulting in the surfactant hydrophobic interactions disruption along the pulling pathway. In simple words, the aggregate breaks in the middle and not by ripping off the head groups, which means that the hydrophobic

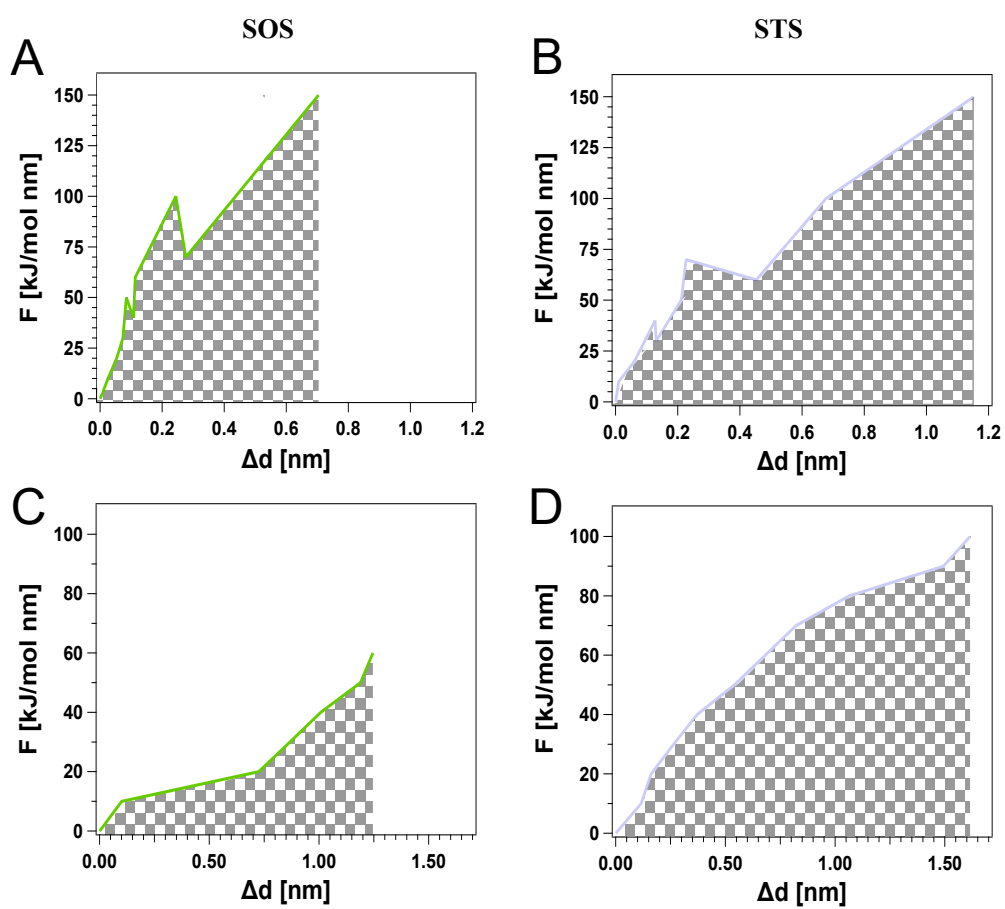


Figure 7.4: Applied pulling forces vs Δd for PE/SOS (A) and PE/STS (B) in parallel geometry, for PE/SOS (C) and PE/STS (D) in orthogonal geometry . The selected areas give the work required to break the surfactant bridge.

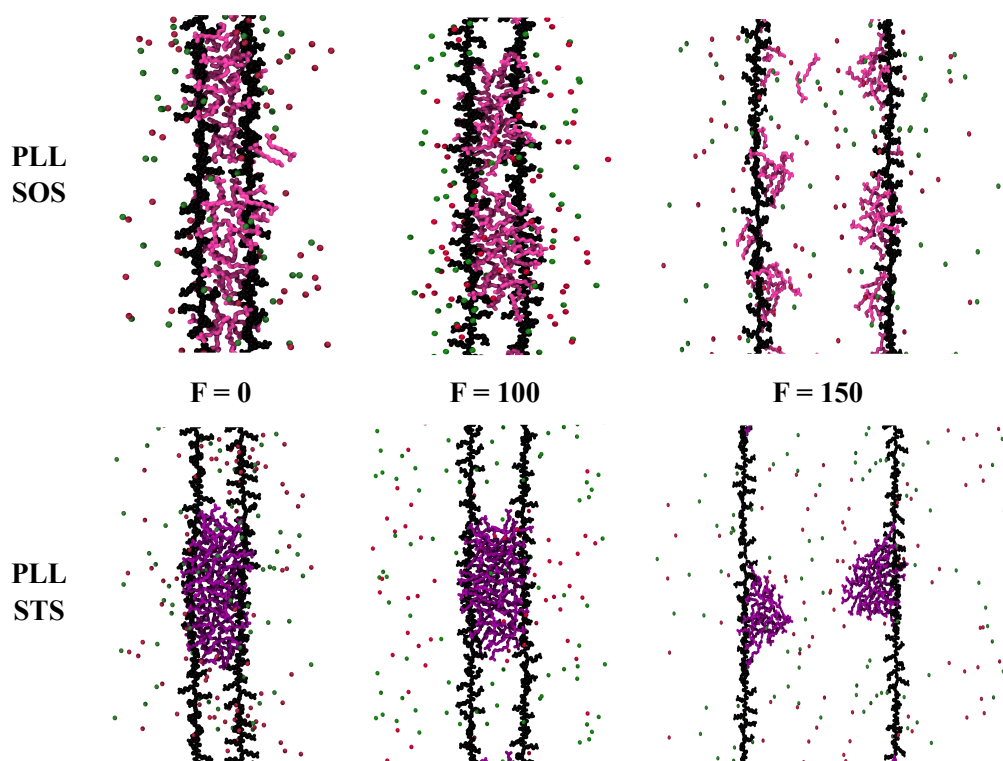


Figure 7.5: CFP representative simulation snapshots in parallel geometry for PE/SOS and PE/STS at $F = (0, 100, 150)$ kJ/(mol nm). For both system at $F = 150$ kJ/(mol nm) the surfactant bridge is broken.

moiety is the weakest part. This result implies that the biggest contribution to the strength of the surfactant bridge is given by the internal hydrophobic cohesion of the aggregates while the headgroup/PE binding is less important. These findings are in good agreement with chapter 6 where it has been proven that double charging the surfactant headgroup, that is increasing the electrostatic surfactant/PE interaction, a drop in viscosity is registered. Therefore, this result demonstrate that the key for viscous PE/surfactant mixtures is a greater hydrophobicity in the system.

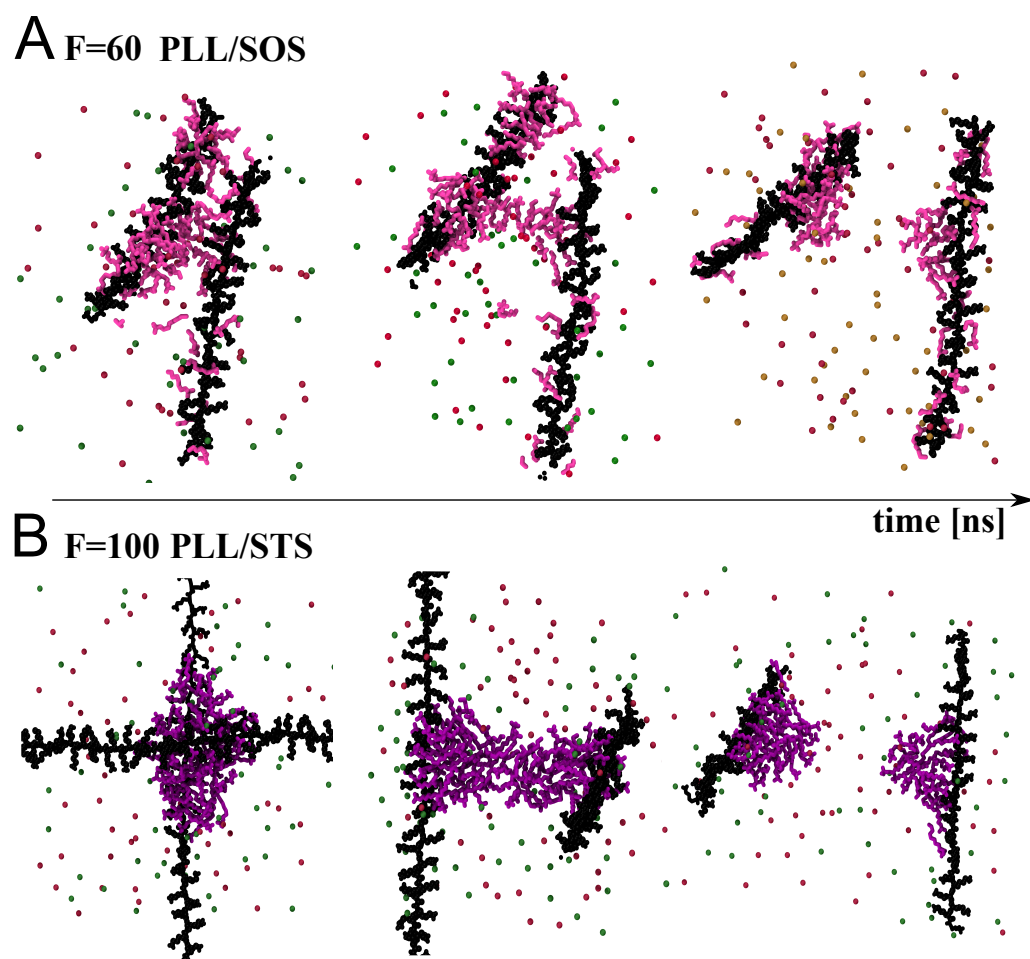


Figure 7.6: CFP representative simulation snapshots in orthogonal geometry for PE/SOS at $F = 60$ kJ/(mol nm) (A) and for PE/STS at $F = 100$ kJ/(mol nm) (B). The snapshots are taken at the breaking force, showing that the rupture process occurs in the middle of the aggregate.

Chapter 8

Conclusions

8.1 Project Overview

This PhD thesis focuses on the mechanism behind the changes of the macroscopic flow behavior in oppositely charged mixtures of JR 400 and various anionic surfactants: SOS, SDS, STS and SDP. The first three surfactants differ in the chain length (C_8 for SOS, C_{12} for SDS, C_{14} for STS) while SDP (C_{12}), depending on the solution pH, can bear one or two negative charges on its headgroup. For these mixtures, polyelectrolyte-surfactant complexes (PESCs) are formed at concentration below the critical micelle concentrations (CMC) of the pure surfactant solution. For example, for JR 400/SOS the concentration at which the surfactant adsorption begins is between 15 and 20 mmol/L, see chapter 5, while the CMC of SOS alone is 134 mmol/L [217]. The macroscopic phase behavior of these solutions can be represented with a phase diagram in which in excess of both components a monophasic region is formed where clear solutions appear and a two phases region in between where precipitation occurs.

As the first of this project, light has been shed on the mechanism at the basis of the shear thinning behavior of 1 wt% JR 400/SDS solutions. Previous works have revealed that for this mixture the increase in viscosity (an enhancement of three orders of magnitude relative to the pure PE solution) observed in the PE excess near the phase boundary to the two phase region is related to the presence of mixed rod-like aggregates [123]. These aggregates interconnect roughly 3 PE chains each [125], acting as cross-links in solution. Moreover, rheology measurements revealed that these mixtures have a Newtonian behavior

at low shear rates, while at high shear rates a shear thinning is registered. Here JR 400/SDS solutions at different charge ratios Z , where $Z = [\text{PE charges}]/[\text{surfactant charges}]$, have been studied with Rheo-SANS (i.e., small angle neutron scattering experiments performed simultaneously with the application of deformational forces on the sample) to resolve the structural origin of the shear thinning behavior. Experiments clarified that the shear thinning is related to a slight orientation of PESCs along the direction of the applied shear. The result is consistent with previous works where it was found that the PE retains some of its freedom of movement even in the aggregate [125].

In the second part, the effect of the surfactant tail length on the PESCs, mesoscopic structure and solution flow behavior have been investigated. Mixtures of JR 400/SOS and JR 400/STS have been analyzed, where the two surfactants only differ in the tail length: 8 carbon atoms for SOS and 14 for STS. Rheology measurements revealed that JR 400/SOS exhibits a water-like behavior over all the Z values. JR 400/STS, instead, displays viscoelastic properties with an increase in viscosity near the phase boundary in PE excess by almost four orders of magnitude relative to the pure JR 400 solution. These findings reflect a different PE/surfactant interaction. Using SANS and NSE the differences in the mesoscopic structures and the dynamics of the systems were inspected. Results revealed that, while the shorter-tail surfactant adsorbs onto the PE chain through the non-cooperative binding (SOS adsorbs as individual molecules on the chains), STS follows the cooperative ones, leading to the formation of rod-like aggregates. STS/JR 400 aggregates have a radius of about 2 nm and incorporate 3 to 4 PE chains on average. These findings suggest that hydrophobic interactions between surfactant molecules dictate the viscosity of the system. For a detailed investigation on the PESCs' mesoscopic structure, experimental results were compared with molecular dynamics (MD) simulations involving two positively charged polypeptides as generic representation of JR 400 (namely PLL and PLG) and SOS, SDS, STS as surfactants. The simulation boxes contained one or two parallel stretched PE with different starting configurations: pre-aggregated or randomly placed amphiphilic molecules. Results are in agreement with SANS analysis since they consistently show that the binding of the short-tail surfactants is less cooperative, while for longer-chain surfactants is cooperative.

To complete the investigation on the role of the surfactant chemistry in the PESCs mesostructure, the effect of the charge on its head group has been explored in the third part. Mixtures of JR 400 and SDP have been studied at different pH. The hydrophobicity of the surfactant can be controlled by the solution's pH since at $\text{pH} > 12$ its headgroup bears two charges, so that SDP^{2-} species are present, while at $\text{pH} 7$ bearing only one charge SDP^- species are present. In alkaline solutions no increase in viscosity is observed when approaching the two phase region in PE excess, while in presence of SDP^- the viscosity increases by up to

three orders of magnitude relative to the pure JR 400 solution. This result is quantitatively comparable with the increase in viscosity for JR 400/SDS mixtures [125]. SANS and NSE experiments showed that, as for JR 400/STS, the enhancement in viscosity is due to the presence of mixed rod-like aggregates which act as cross links in solution, interconnecting on average 3 PE chains. Moreover, rheology measurements have demonstrated that the change in viscosity can be reversible and the switching process can be repeated several times before the chemical decomposition of the surfactant seems to occur eventually.

Finally, in the fourth part the mechanical stability of the mixed rod-like aggregates was explored with constant-force pulling (CFP) simulations on PE/SOS and PE/STS systems. Simulations were performed with two PE chains in two different extreme configurations: parallel and orthogonal geometries. Applying a wide range of pulling forces, the analysis showed that the surfactant bridge (which binds the two PEs) is resistant up to a certain strength of the force. From the study of the maximal pulling force, F_{\max} , tolerated by the system and the relative deformation, one can estimate the binding energy, E_b . In the parallel geometry, force and energy values are comparable between the two surfactant. In contrast, when in the orthogonal configuration STS provides to the system higher F_{\max} and E_b . This difference can be explained considering that in the latter configuration the contact zone between PEs is quasi-point-like and the binding through a large and more cohesive aggregate (which occurs with STS) is stronger compared to that through few less cohesive surfactants at the contact point. Moreover, larger aggregates go through a bigger deformation before rupture, resulting in a higher mechanical work to reach that point. These findings are in agreement with the experiments, which show a viscosity increase only with surfactants with sufficiently long tails (C_{12}, C_{14}).

MD simulations also show that rupture of the surfactant bridge occurs in the hydrophobic region of the aggregates, for both systems. This results underlines that the internal cohesion of the aggregates is predominantly based on the hydrophobic interactions in the system. This result is consistent with the experimental results described in chapter 6, where in presence of 2 charges on the surfactant headgroup, i.e., an enhancement of electrostatic interactions in the system, hardly any increase in viscosity upon surfactant addition is observed.

The results achieved during this PhD project offer a better understanding on the physico-chemical mechanisms underlying the unique rheological properties of PESCs. The acquired knowledge offers the possibility to design PESCs with specific properties, like tailor-made stimuli-responsive solutions or solution with preselected viscosity.

8.2 Outlook

Although the thesis provides insight into the viscosity changes in polyelectrolyte/anionic surfactant mixtures, future research could resolve some additional unexplored points. Possible future step could be to understand with rheo-NSE measurements [146] if the viscosity is also influenced by an increase of mobility of the PE chains in the aggregates. After investigating the effect of the surfactant characteristics in determining the PESC's mesostructure, one could think to study the effect of the PE structure. New results could be achieved varying the PE charge density, its intrinsic backbone rigidity or the spacer length between charges to discover how these parameters affect the rheological behavior in solution. Furthermore, a future work could consist in two new MD simulations studies. (I) To Perform CFP simulations where two polyelectrolyte chains are sheared next to each other rather than pulling them apart. In this way a more relevant investigation on the viscosity could be achieved. (II) To Develop and validate specific force fields for JR 400. In this way more quantitative comparison between MD and experiments could be possible to get a more realistic overview in gain insights into the interaction of PE and surfactants.

Appendices

Appendix A

content related to chapter 4

A.1 Rheology

A.1.1 Rheology Measurements on JR 400/SDS Samples

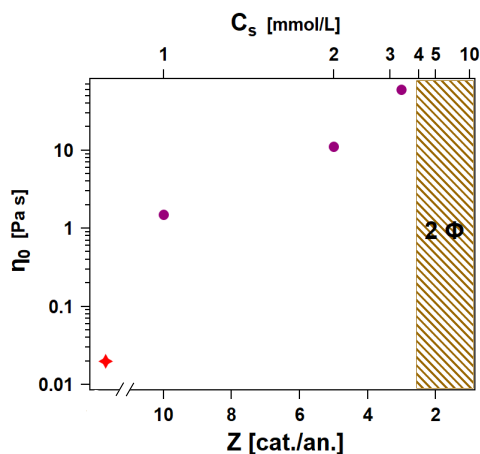


Figure A.1: Zero shear viscosity η_0 as a function of charge ratio Z (bottom) and surfactant concentration (top) for samples with 1 wt% JR 400/SDS (10 mM of charges); the red value after the axis split is the value for a pure JR 400 solution; the shaded area at low values of Z indicates the onset of the 2-phase region.

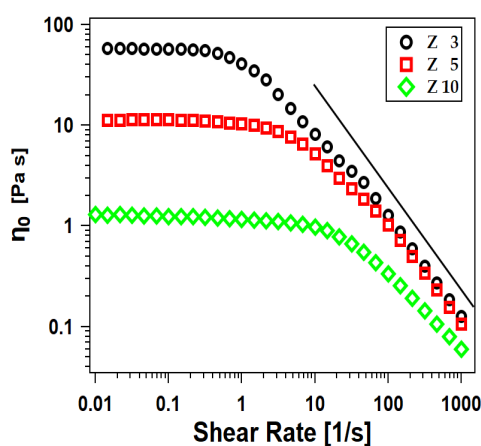


Figure A.2: Viscosity as a function of shear rate for samples with 1 wt% JR 400 and charge ratio Z indicated in the graph. The samples are shear thinning with a critical shear rate $\dot{\gamma}$ which decreases with increasing surfactant concentration. Black line is $\eta \sim \dot{\gamma}^{-1}$, fitting the high shear rate part with a power law yields exponents of -1.01 ($Z = 3$), -0.96 ($Z = 5$) and -0.75 ($Z = 10$).

A.2 SANS

A.2.1 Modelling the SANS Data

The radially averaged intensity of rodlike particles can be modelled as a linear combination of the intensity from the aggregates and the intensity from free PE chains. The aggregates consist of all of the surfactant in the sample and a fraction of the PE x_{PE} , so that their volume fraction ϕ_{agg} is given by:

$$\phi_{\text{agg}} = \phi_{\text{surf}} + \phi_{\text{PE}}x_{\text{PE}}, \quad (\text{A.2.1})$$

where ϕ_{surf} and ϕ_{PE} are the volume fraction of surfactant and PE, respectively. The volume fraction of the free PE is expressed through the macroscopic volume fraction ϕ_{PE} and the aggregate-incorporated fraction x_{PE} as

$$\phi_{\text{PE}}^{\text{free}} = \phi_{\text{PE}}(1 - x_{\text{PE}}) \quad (\text{A.2.2})$$

and the intensity reads

$$I(Q) = \frac{\phi_{\text{agg}}}{V_{\text{agg}}}P_{\text{agg}}(Q) + \frac{\phi_{\text{PE}}(1 - x_{\text{PE}})}{V_{\text{PE}}}P_{\text{PE}}(Q), \quad (\text{A.2.3})$$

with V_{agg} and V_{PE} are the volume of an aggregate and a PE segment and P_{agg} and P_{PE} are the form factors of aggregate and PE. It is possible to model both the PE and the aggregates as cylinders, the form factor of which is given by eq. (2.3.9), with eq. (2.3.10) where R and L are radius and length of the cylinder and ΔSLD is the difference in scattering length density between the cylinder and the solvent. For the aggregates, ΔSLD_{agg} depends on the amount of PE which they contain:

$$\Delta SLD_{\text{agg}} = \frac{\phi_{\text{surf}}}{\phi_{\text{agg}}}SLD_{\text{surf}} + \frac{\phi_{\text{PE}}x_{\text{PE}}}{\phi_{\text{agg}}}SLD_{\text{PE}} - SLD_{\text{solv}}, \quad (\text{A.2.4})$$

where SLD denotes the scattering length density of a component and the subscripts *surf*, *PE* and *solv* represent surfactant, PE and solvent. As in the samples are used all hydrogenated components in a deuterated solvent, resulting in a high contrast between aggregates and solvent and a low internal contrast it is sufficient to model the aggregates as homogeneous cylinders. Assuming a homogeneous structure of the aggregates along their long axis, we can calculate the average number of PE chains per aggregate $N_{\text{PE chains}}$ by relating the volume fractions of surfactant and PE in the aggregates to the radii of the whole

aggregate and individual PE chains:

$$N_{\text{PE chains}} = \frac{x_{\text{PE}}\phi_{\text{PE}}}{x_{\text{PE}}\phi_{\text{PE}} + \phi_{\text{surf}}} \frac{R_{\text{agg}}^2}{R_{\text{PE}}^2} \quad (\text{A.2.5})$$

where R_{agg} is the radius of the mixed aggregates and R_{PE} is the radius of an individual PE chain. Previously, it has been seen that at values of $N_{\text{PE chains}} < 2$ no pronounced increase in viscosity can be observed as the aggregates do not act as efficient cross links anymore [125].

A.2.2 SANS Measurements on JR 400/SDS Samples

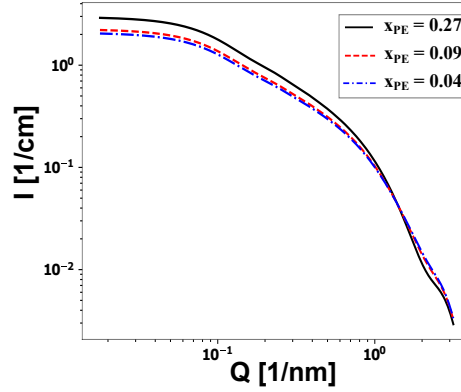


Figure A.3: Theoretical curves calculated from eq. (A.2.3) using parameters obtained for SDS/JR 400 $Z = 3$ from Hoffmann et al. [125] and macroscopic volume fractions ($R_{\text{agg}} = 1.8$ nm, $R_{\text{PE}} = 0.8$ 1/nm, $\phi_{\text{surf}} = 0.001$, $\phi_{\text{PE}} = 0.007$ and $x_{\text{PE}} = 0.27$) together with two lower values of x_{PE} corresponding to roughly 3, 2 and 1 PE chains per aggregate. A reduction of x_{PE} would result in a noticeable change in intensity.

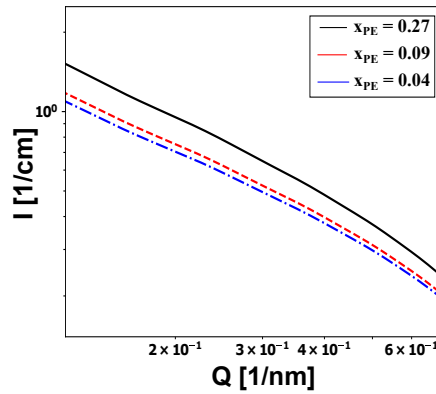


Figure A.4: Same data as fig. A.3 but in the mid Q range from 0.12 to 0.7 1/nm.

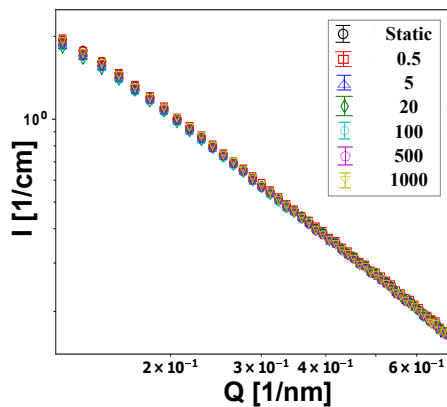


Figure A.5: Magnification of the data in fig. 4.1 in the Q range from 0.12 to 0.7 1/nm. No change in intensity with shear rate is observed.

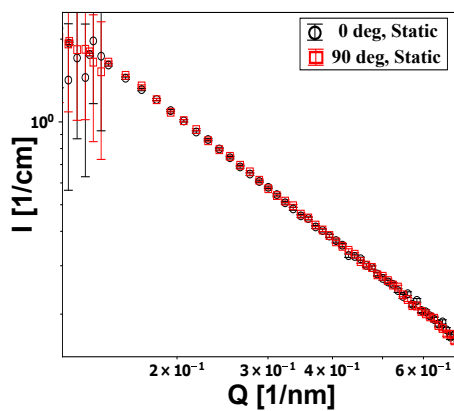


Figure A.6: 45° sector averages parallel (0°) and perpendicular (90°) to the direction of shear in the Q range from 0.12 to 0.7 1/nm of the sample with 1 wt% JR 400 and $Z = 3$ at rest. No difference can be seen and the scattering is isotropic.

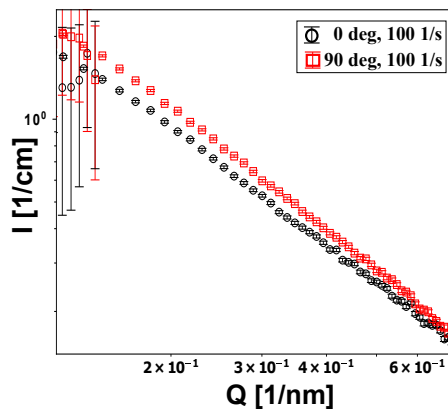


Figure A.7: 45° sector averages parallel (0°) and perpendicular (90°) to the direction of shear in the Q range from 0.12 to 0.7 1/nm of the sample with 1 wt% JR 400 and $Z = 3$ at $\dot{\gamma} = 100$ 1/s. The sector perpendicular to the direction of shear shows a somewhat higher intensity, meaning that the rodlike aggregates are aligned in the direction of shear.

Appendix B

content related to chapter 5

B.1 Rheology

B.1.1 Rheology Measurements on JR 400/STS Samples

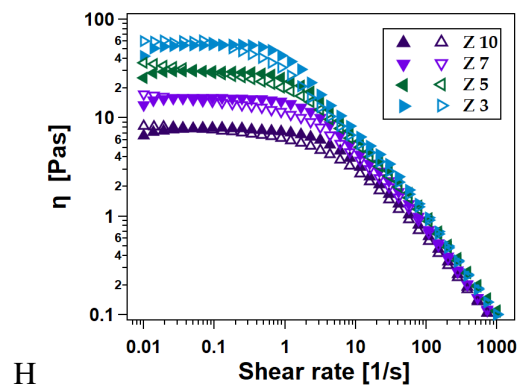


Figure B.1: Viscosity as a function of $\dot{\gamma}_{crit}$ of STS/JR 400 1 wt. % mixtures for different Z. Open symbols: decreasing, closed symbols: increasing shear rate,

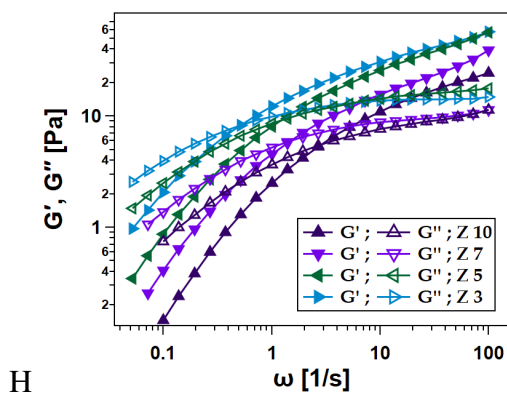


Figure B.2: Elastic modulus G' and viscous modulus G'' as a function of angular frequency for STS/JR 400 mixtures

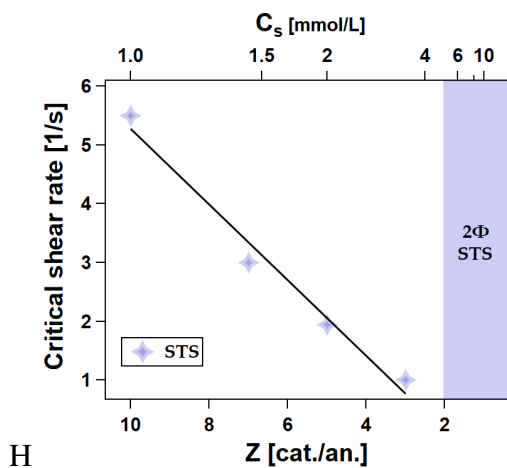


Figure B.3: Critical shear rate of JR 400/STS as a function of the charges ratio (bottom) and STS concentration (top).

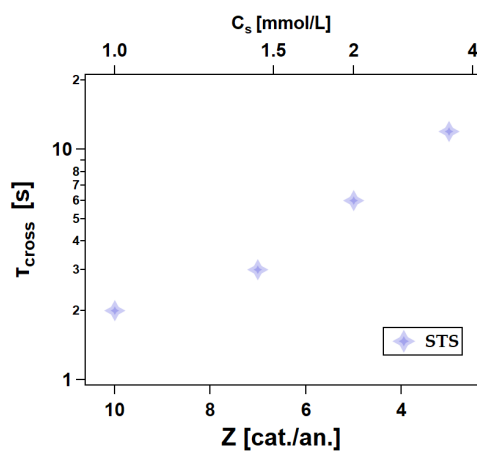


Figure B.4: Structural relaxation time τ_{cross} of STS/JR 400 as a function of Z (bottom) and surfactant concentration (top).

B.2 SANS

B.2.1 Modeling the SANS Data

The PE curve is modelled as thin cylinder,so that:

$$I_{\text{PE}}(Q) = {}^1N_{\text{PE}} \int f(R, R_{\text{PE}}) P_{\text{cyl}}(Q, R, \Delta SLD_{\text{PE}}, L_{\text{PE}}) dR, \quad (\text{B.2.1})$$

with the scattering length density difference ΔSLD_{PE} between PE and D_2O and the particle number density of free PE segments

$${}^1N_{\text{PE}} = \frac{\phi_{\text{PE}}}{\int f(R, R_{\text{PE}}, \sigma) V(R, L) dR}. \quad (\text{B.2.2})$$

and the P_{cyl} given by eq. (2.3.9).

To describe the interactions between the charged micelles in the surfactant excess for both SOS/JR 400 and STS/JR 400 ,see fig. B.6, it has been used the structure factor for charged colloids by Baba-Ahmed, Benmouna and Grimson [23], see section 2.3.3.

B.2.2 SANS Measurements on JR 400/SOS and JR 400/STS Samples

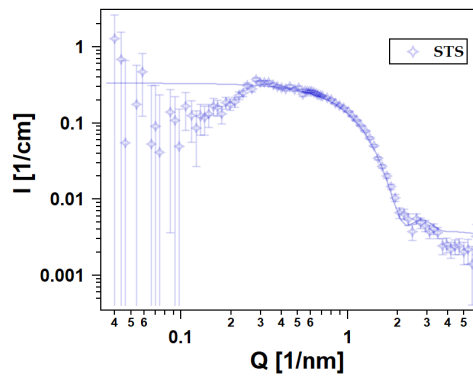


Figure B.5: SANS curves of the pure STS at 35 °C. From the radius 2.12 nm of the micelle, it was found an aggregation number, $N = 76$.

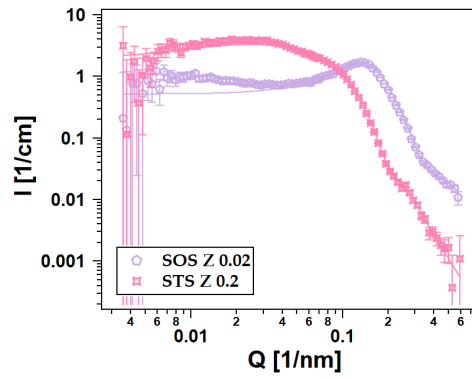


Figure B.6: SANS curves of SOS/JR 400 and STS/JR 400 in surfactant excess ($Z = 0.02$ for SOS at room temperature and $Z = 0.2$ for STS at 35 °C)

Table B.1: SANS Fit Parameters of JR 400/STS (1 wt %) mixtures.

Sample	Z	R [nm]	L [nm]	ϕ_{agg}	ϕ_{surf}
JR 400	/	0.8	6	0.006	/
JR 400/STS	10	1.96	20	0.0014	0.00035
JR 400/STS	7	2.10	25	0.0027	0.00053
JR 400/STS	5	2.04	44	0.0033	0.00077
JR 400/STS	3	1.93	/	0.0038	0.00116

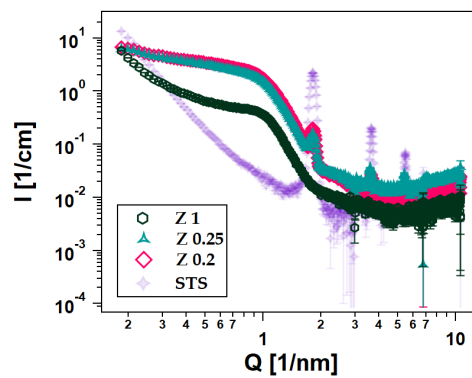


Figure B.7: WANS curves of the pure STS precipitate and STS/JR 400 at $Z = 1$ ($C_{STS} = 10$), $Z = 0.25$ ($C_{STS} = 40$) and $Z = 0.2$ ($C_{STS} = 50$).

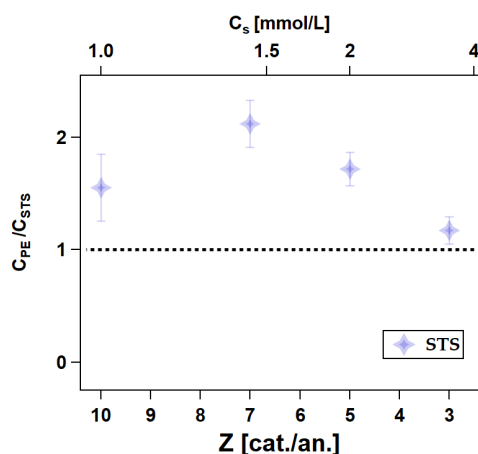


Figure B.8: Ratio of PE-STs charges in the aggregates as a function of charges ratio (bottom) and STS concentration (top); dashed line represents the charge neutrality.

B.3 DLS

B.3.1 DLS Measurements on JR 400/STS Samples

The decay time of the slow mode is related to τ_{fast} , τ_{crit} and η as $\tau_{slow}(q) = (t_{crit}^{-\eta}(q))^{1/(1-\eta)}$, see section 2.1.1 for more details.

While the fast time shows diffusive q^{-2} behavior, the q dependence of τ_{slow} is proportional to $q^{-2/(1-\eta)}$, as follows from inserting the q^{-2} dependence into the expression for τ_{slow} .

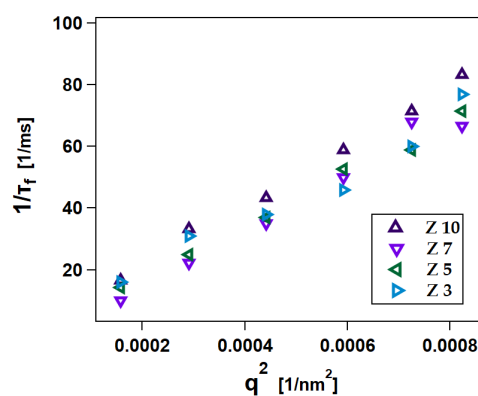


Figure B.9: $1/\tau_{fast}$ of STS/JR 400 (1 wt %) mixtures as a function of q^2 ; the fast mode behaves diffusive.

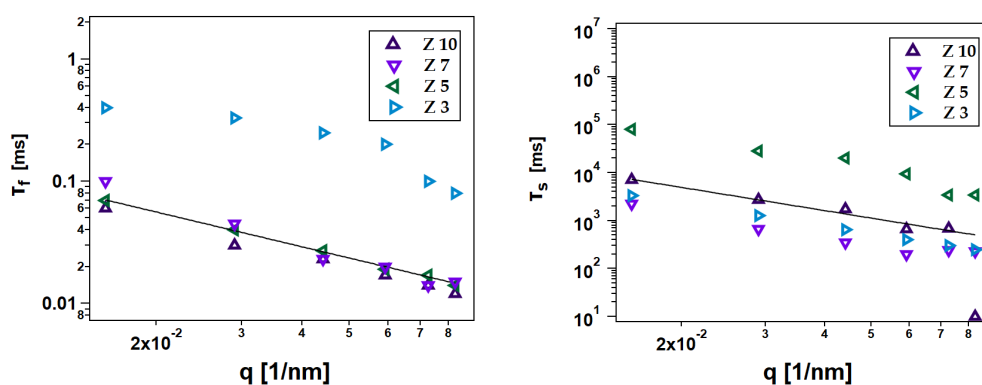


Figure B.10: Fast mode τ_{fast} and Slow mode τ_{slow} of STS/JR 400 (1 wt %) mixtures as a function of q . The strong q dependence of slow modes shows its non-diffusive character and it originates from the presence of large objects in the network solution.

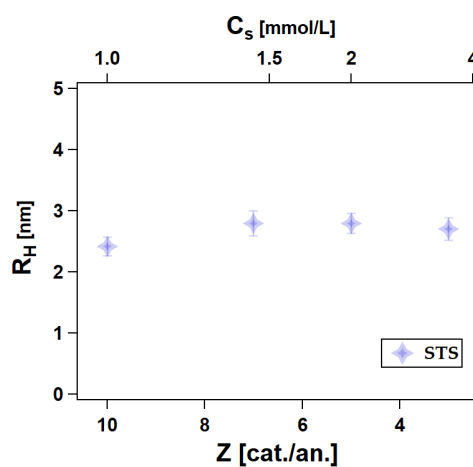


Figure B.11: Hydrodynamic radius R_H calculated from the fast mode τ_{fast} of STS/JR 400 (1 wt %) mixtures as a function of charges ratio (bottom) and surfactant concentration (top). R_H remains almost unchanged.

B.3.2 DLS Measurement on the pure JR 400 Solution

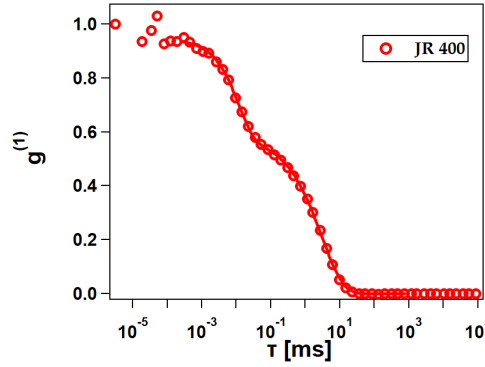


Figure B.12: $g^{(1)}$ of 1 wt% JR 400 at scattering angle of 110° fitted with an exponential and a stretched exponential (solid line).

B.4 NSE

B.4.1 NSE Measurement on the Pure JR 400 Solution

At intermediate length scales between the size of the overall polymer and the size of individual segments the behaviour of a polymer in solution is governed by hydrodynamic interactions and D_{app} depends linearly on Q and the slope a is related to the solvent viscosity [7, 82, 223] so that $D_{\text{app}}(Q) = D_0 + aQ$. In a more elaborate approach, Dubois-Violette and De Gennes [82] developed an expression for the intermediate scattering function of an infinitely long polymer in solution based on a Rouse-Zimm chain [300]:

$$S_{\text{Zimm}}(Q, t) = (\Gamma_{\text{Zimm}} t)^{2/3} \int_0^\infty \exp\left(-(\Gamma_{\text{Zimm}} t)^{2/3} u [1 + h(u)]\right) du \quad (\text{B.4.1})$$

$$S_{\text{Zimm}}(Q, 0) = 1$$

$$h(u) = \frac{4}{\pi} \int_0^\infty \frac{\cos(y^2)}{y^3} \left[1 - \exp(-y^3 u^{-3/2})\right] dy \quad (\text{B.4.2})$$

and

$$\Gamma_{\text{Zimm}} = \frac{\sqrt{3} Q^3 k_B T}{6^{3/2} \eta_{\text{solv}}}, \quad (\text{B.4.3})$$

and the solvent viscosity η_{solv} is the only property of the sample entering in eq. (B.4.1). To account for translational diffusion, eq. (B.4.1) is modified as follows:

$$S_{\text{Zimm}}^{\text{diff}}(Q, t) = \exp(-D_0 Q^2 t) [(1 - A(Q)) + A(Q) S_{\text{Zimm}}(Q, t)], \quad (\text{B.4.4})$$

where $A(Q)$ is the amplitude of the internal motions of the polymer and D_0 accounts for the translational diffusion of the polymer. Using these equations to fit the NSE data of a pure JR 400 solution yields good results, see fig. B.13,

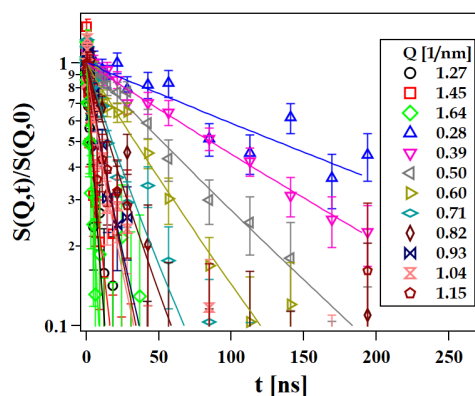


Figure B.13: Intermediate scattering function of 1 wt% JR 400 with fits using eq. (B.4.1); the fit yields a viscosity above the solvent viscosity due to internal friction effects.

and a solvent viscosity of 3 mPas is obtained, which is significantly above the viscosity of pure D_2O . This can be attributed to internal friction effects as observed in intrinsically disordered proteins [12, 27] and underlines the fact that JR 400's cellulose backbone is relatively stiff.

B.4.2 NSE Measurement on the JR 400/STS Solutions

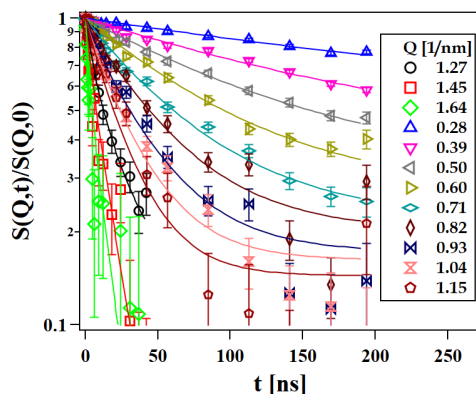


Figure B.14: Fit of the NSE data for STS/JR 400 (1 wt%), $Z = 3$ using eq. (5.2.8) with only the length of the aggregates and elastic background as free parameters. All other parameters are known from SANS.

B.5 MD Simulations

B.5.1 Detailed Description of STS Micelle Simulation Protocol

To obtain STS micelle we used a stepwise alchemic transformation.

We first removed all STS atomic partial charges to obtain a totally unpolar versions of STS that hydrophobically assemble into oil-like droplets. Subsequently, we stepwise increased the partial charges until the original and chemically realistic partial charges were recovered. For each step, we allowed the system to equilibrate into a configuration with the increasingly polar headgroups pointing outwards. The number of counterions was adjusted in each step to compensate the total charge of the aggregate of STS molecules with fractional partial charges.

B.5.2 How to Define the Largest Distance to be Considered in a Cluster

To define the cutoff value *cut* in the GMX-clustsize tool we analyzed the trajectory of a single micelle of SOS, SDS, STS. For SDS and STS micelles it has been found that the minimum *cut* values to have over the last 50 ns of simulation 1 single cluster are 0.41 and

0.42 nm respectively. For SOS due to the short lifetime of the micelle we analyzed the first ns of the simulation resulting in $cut = 0.44$ nm (see fig. B.15). To compare SOS, SDS and STS with the same cut , it has been fixed at 0.44 nm.

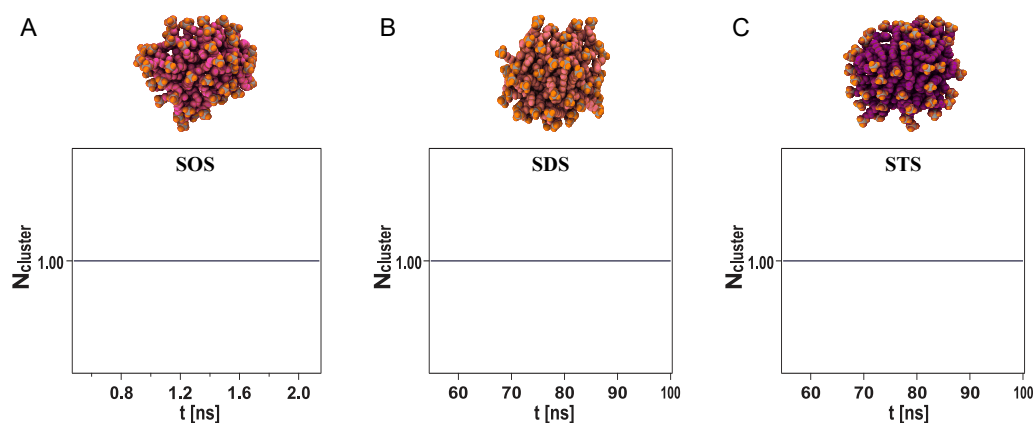


Figure B.15: Number of cluster over simulation time (bottom line) and snapshots of micelles (top line) for A) SOS, B) SDS and C) STS. In the snapshots are also shown the surfactant polar head groups (in orange) oriented outside the aggregate.

B.5.3 PLG/SDS Aggregate

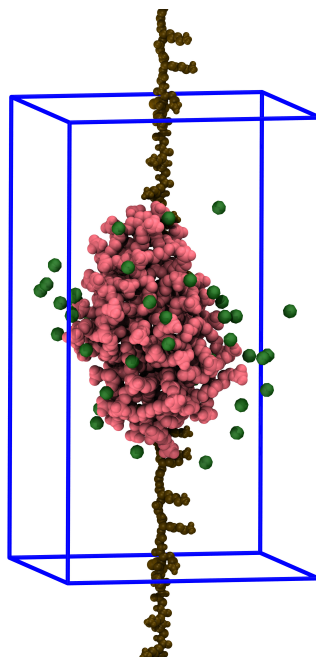


Figure B.16: Representative snapshots of SDS aggregates interacting with a single PLG chain starting from pre-aggregated micelle. The simulation box is indicated with blue coboids.

B.5.4 Minimum vs Detailed Counterions

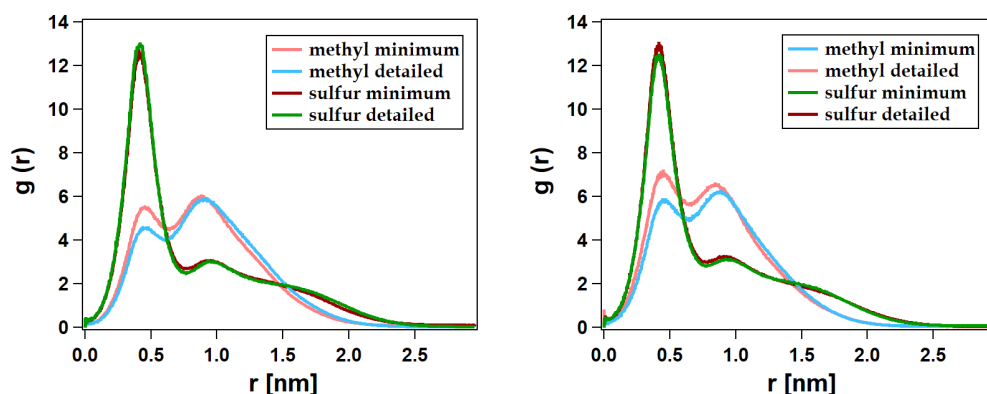


Figure B.17: Minimum vs Detailed counterions. RDFs of methyl and sulfur atoms for SOS/PLG starting from randomly placed surfactants molecules (left) and pre-aggregated micelle (right). The influence of the salt configuration is negligible.

B.5.5 PLL/SOS and PLL/STS from Pre-aggregated Micelle

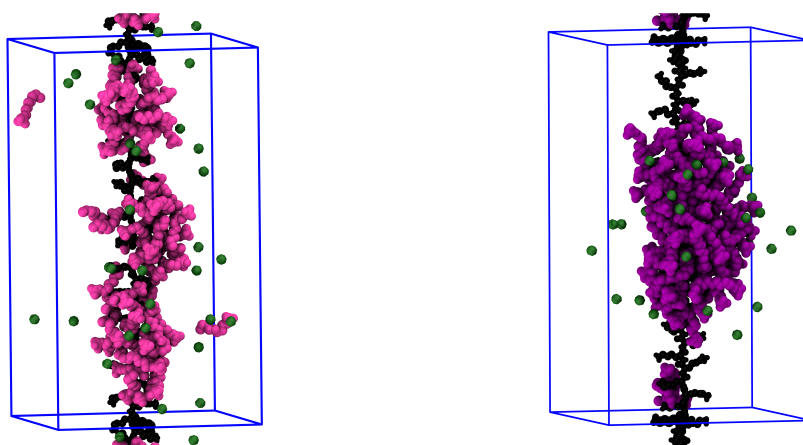


Figure B.18: Representative snapshots of SOS (left) and STS (right) aggregates interacting with a single PLL chain starting from pre-aggregated micelle. The simulation box is indicated with blue coboids

B.5.6 Cluster Analysis

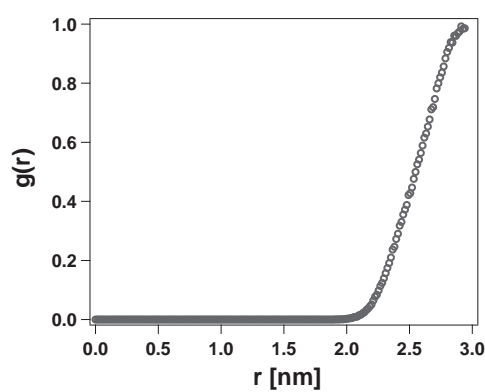


Figure B.19: Cylindrical rdf of two parallel PE chains in water with counterions without surfactants.

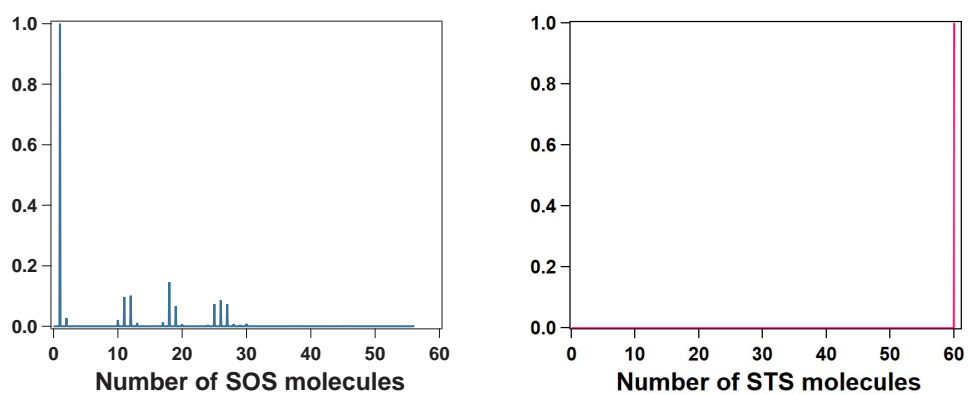


Figure B.20: Cluster distribution in the trajectory for SOS/PLG (left) and STS/PLG (right) starting from pre-aggregated micelles, minimum counterions.

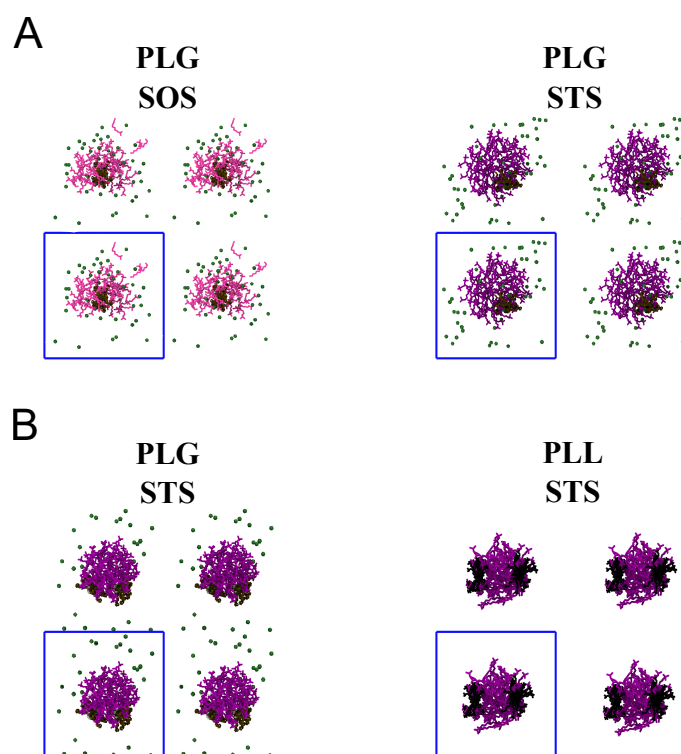


Figure B.21: (A) Top views of snapshots of SOS and STS aggregates interacting with a single PLG chain. (B) Top views of snapshots of STS aggregates interacting with two parallel PLG and PLL chains. The simulation box is indicated with blue rectangle.

Appendix C

content related to chapter 6

C.1 Materials

C.1.1 SDP Titration Curve

To understand how the monoanionic and dianionic species of SDP are distributed as a function of pH, the titration curve was determined, fig. C.1.

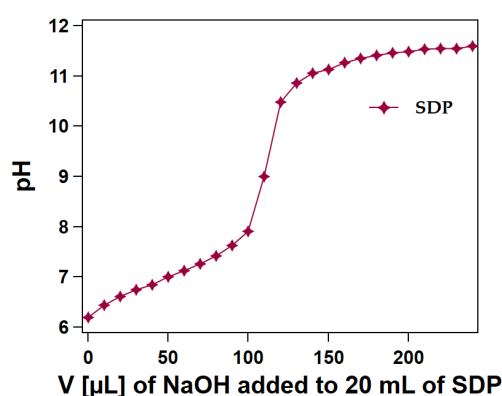


Figure C.1: Titration curve for SDP, 20 mM, at room temperature, in water as function of added volume of NaOH 0.1 M.

The curve shows two different regions: the first one in a pH range of 6-8 and a second in a range of 11-12. According with Nakayama et al. [193] at higher pH values the surfactant head groups are completely ionized (SDP^{2-}), while in solutions closed to neutrality mono

charged species are present (SDP^-). The charge of the head group, which depends on the pH, dictates the aggregation behaviour of the pure surfactant solution. Large size aggregates are formed by protonated SDP molecules, while smaller size is constructed in alkaline solution due to the electrostatic head group repulsion which are bearing two negative charges [193, 269].

C.2 Rheology

C.2.1 Rheology Measurements on JR 400/SDP Samples

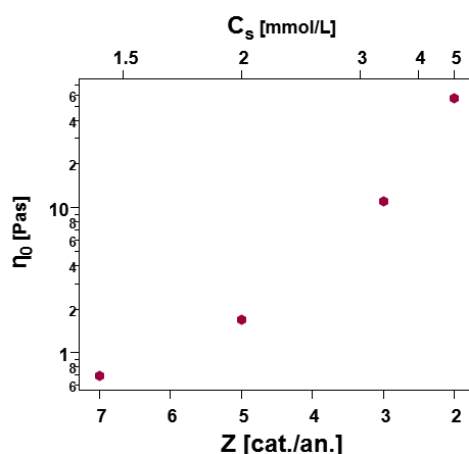


Figure C.2: Zero shear viscosity of JR 400/SDP⁻ mixtures as function of Z (bottom) and surfactant concentration (top).

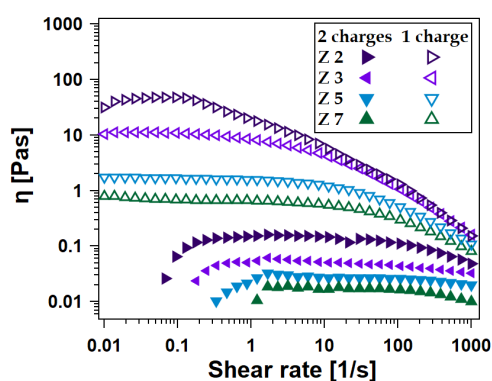


Figure C.3: Viscosity as a function of $\dot{\gamma}_{crit}$ of JR 400 with SDP²⁻ (closed symbols) and with SDP⁻ (open symbols) at different Z values.

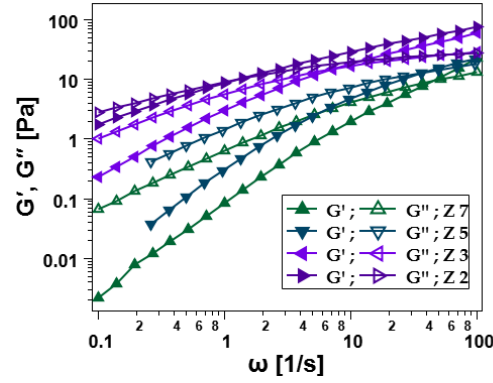


Figure C.4: Elastic modulus G' and viscous modulus G'' as a function of angular frequency for JR 400/SDP⁻ mixtures.

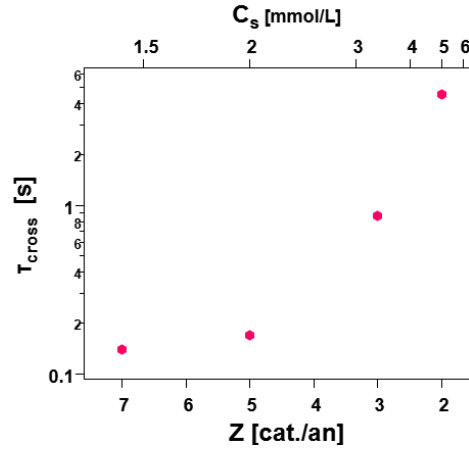


Figure C.5: Structural relaxation time τ_{cross} of JR 400/SDP⁻ as a function of Z (bottom) and surfactant concentration (top).

According to Green and Tobolsky [108, 246], the plateau value of G' , termed G_0 , is related to the network junction density via eq. (5.2.1):

$$G_0 = g\epsilon k_B T \quad (\text{C.2.1})$$

with the network junction density ϵ , the absolute temperature T , Boltzmann's constant k_B and a factor g to account for the strength of the junctions in units of $k_B T$, which is initially set to 1 for the calculation of the values in table 5.1.

Table C.1: Parameters obtained from Oscillatory Shear Rheology of JR 400/SDP⁻ mixtures.

Z /	ω_{cross} [rad/s]	τ_{cross} [s]	G_0 [Pa]	ϵ [m ⁻³]	ξ [nm]
7	45	0.14	22	5.49×10^{21}	57
5	36	0.17	56	1.35×10^{22}	42
3	7.2	0.87	60	1.47×10^{22}	40
2	1.39	4.52	77	1.87×10^{22}	38

C.3 SANS

C.3.1 Modelling the SANS Data

The SANS signal of an ensemble of monodisperse, non interacting particles is generally given as eq. (2.3.4). The form factor of randomly oriented cylinders with radius R and length L is given by eq. (2.3.9), where the integral over x takes into account the orientational average and $F_{\text{cyl}}(q, x)$ is the scattering amplitude given by eq. (2.3.10), comprising the first order Bessel function J_1 .

If the sample is polydisperse with regard to the radius, eq. (2.3.4) takes the form of eq. (2.3.5), see section 2.3.1 for more details.

The curve of pure PE can be described by the equation eq. (B.2.1):

$$I_{\text{PE}}(Q) = {}^1N_{\text{PE}} \int f(R, R_{\text{PE}}) P_{\text{cyl}}(Q, R, \Delta SLD_{\text{PE}}, L_{\text{PE}}) dR, \quad (\text{C.3.1})$$

with the scattering length density difference ΔSLD_{PE} between PE and D₂O and the particle number density of free PE segments:

$${}^1N_{\text{PE}} = \frac{\phi_{\text{PE}}}{\int f(R, R_{\text{PE}}, \sigma) V(R, L) dR}. \quad (\text{C.3.2})$$

The SANS curves of PE/SDP²⁻, see fig. C.6,

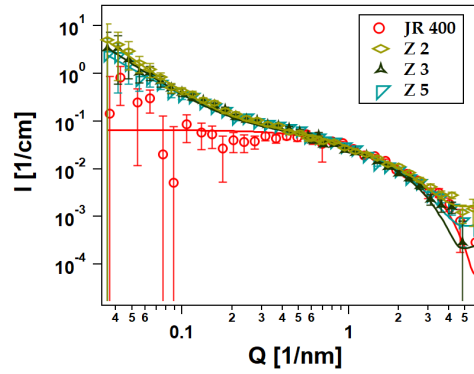


Figure C.6: SANS curves of JR 400/SDP²⁻ 1 wt % at different charge ratios.

can be described with the same model used for the pure PE, only adapting the volume fraction and the scattering length density, so that

$$\phi_{\text{PE/SDP}^{2-}} = \phi_{\text{PE}} + y_{\text{SDP}^{2-}} \phi_{\text{SDP}^{2-}} \quad (\text{C.3.3})$$

and

$$SLD_{\text{PE/SDP}^{2-}} = \frac{\phi_{\text{PE}}}{\phi_{\text{PE/SDP}^{2-}}} SLD_{\text{PE}} + \frac{y_{\text{SDP}^{2-}} \phi_{\text{SDP}^{2-}}}{\phi_{\text{PE/SDP}^{2-}}} SLD_{\text{SDP}^{2-}} \quad (\text{C.3.4})$$

To describe the PE/SDP⁻ mixed aggregates, see fig. 6.3, it has been used the same equation for PE/STS [29, 73], that is eq. (5.2.4):

$$\begin{aligned} I_{\text{agg}}(Q) = & {}^1N_{\text{agg}} \int f(R, R_{\text{agg}}, \sigma) P_{\text{cyl}}(Q, R, \Delta SLD_{\text{agg}}, L_{\text{agg}}) dR \\ & + \text{erf} \left(\left(Q R_{\text{agg}} / \sqrt{12} \right)^2 \right) \frac{\phi_{\text{PE}} x_{\text{PE}}}{\int f(R, R_{\text{PE}}, \sigma) V_{\rho}(R, L_{\text{PE}}) dR} \\ & \times \int f(R, R_{\text{PE}}, \sigma) P_{\text{cyl}}(Q, R, SLD_{\text{PE}} - SLD_{\text{surf}}, L_{\text{PE}}) dR \quad (\text{C.3.5}) \end{aligned}$$

with ΔSLD_{agg} given by eq. (A.2.4), here reported:

$$\Delta SLD_{\text{agg}} = \frac{\phi_{\text{surf}}}{\phi_{\text{agg}}} SLD_{\text{surf}} + \frac{\phi_{\text{PE}} x_{\text{PE}}}{\phi_{\text{agg}}} SLD_{\text{PE}} - SLD_{\text{solv}} \quad (\text{C.3.6})$$

Assuming the aggregates homogeneous along their length it is possible to calculate the number of PE chains per aggregate with eq. (A.2.5), that is:

$$N_{\text{PE chains}} = \frac{x_{\text{PE}} \phi_{\text{PE}}}{\phi_{\text{agg}}} \frac{R_{\text{agg}}^2}{R_{\text{PE}}^2}. \quad (\text{C.3.7})$$

where R_{agg}^2 is the radius of the mixed aggregates and R_{PE}^2 is the radius of an individual PE chain.

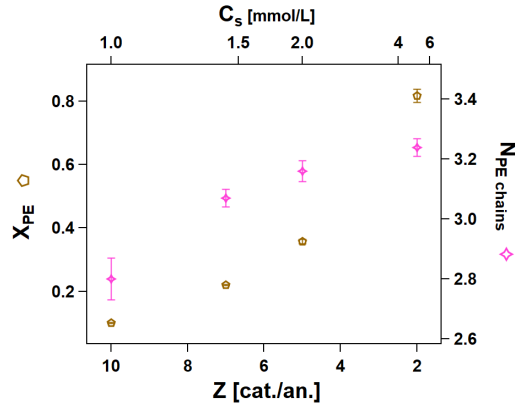


Figure C.7: Fraction of PE in the aggregates x_{PE} , left axis. Average number of PE chains per aggregate, right axis. Both as a function of charges ratio (bottom) and SDP⁻ concentration (top).

C.4 NSE

C.4.1 Modelling the NSE Data

At intermediate length scales, the behaviour of a polymer in solution is governed by hydrodynamic interactions. D_{app} depends linearly on Q and the slope a is related to the solvent viscosity [7, 82, 223] so that $D_{app}(Q) = D_0 + aQ$. Dubois-Violette and De Gennes [82] derived an expression for the intermediate scattering function of an infinitely long polymer in solution based on a Rouse-Zimm chain [300], eq. (B.4.1) here reported:

$$S_{Zimm}(Q, t) = (\Gamma_{Zimm}t)^{2/3} \int_0^\infty \exp\left(-(\Gamma_{Zimm}t)^{2/3}u [1 + h(u)]\right) du \quad (C.4.1)$$

$$S_{Zimm}(Q, 0) = 1$$

$$h(u) = \frac{4}{\pi} \int_0^\infty \frac{\cos(y^2)}{y^3} \left[1 - \exp(-y^3 u^{-3/2})\right] dy \quad (C.4.2)$$

where

$$\Gamma_{Zimm} = \frac{\sqrt{3}Q^3 k_B T}{6^{3/2} \eta_{solv}}, \quad (C.4.3)$$

and the solvent viscosity η_{solv} is the only property of the sample entering in eq. (B.4.1). To account for translational diffusion, eq. (B.4.1) is modified as follows:

$$S_{Zimm}^{diff}(Q, t) = \exp(-D_0 Q^2 t) [(1 - A(Q)) + A(Q) S_{Zimm}(Q, t)], \quad (C.4.4)$$

where $A(Q)$ is the amplitude of the internal motions of the polymer and D_0 accounts for the translational diffusion of the polymer. The intermediate scattering functions of samples

with single-charged surfactant can be described as superposition of S_{rod} (eq. (2.4.5)) and $S_{\text{Zimm}}^{\text{diff}}$ (eq. (B.4.4)) where the ratio between the two contributions is fixed through x_{PE} which is known from the SANS fits. In addition, as already shown in eq. (5.2.8) of chapter 5, at long Fourier times an elastic component becomes visible, which is accounted for by a constant term S_{el} :

$$S(Q, t) = \frac{1}{S(Q, 0)} \left(\frac{\phi_{\text{surf}} + x_{\text{PE}} \phi_{\text{PE}}}{V_{\text{agg}}} P_{\text{agg}} \cdot S_{\text{rod}}(Q, t) + \frac{(1 - x_{\text{PE}}) \phi_{\text{PE}}}{V_{\text{PE}}} P_{\text{PE}} \cdot S_{\text{Zimm}}^{\text{diff}}(Q, t) \right) + S_{\text{el}}(Q). \quad (\text{C.4.5})$$

In these fits, the only free parameters are the (Q -independent) length of the rods in $S_{\text{rod}}(Q, t)$ and $S_{\text{el}}(Q)$. All other parameters are either known from SANS or fits to the NSE data of the pure JR 400 solution.

C.4.2 Measurements on SDP^- Samples

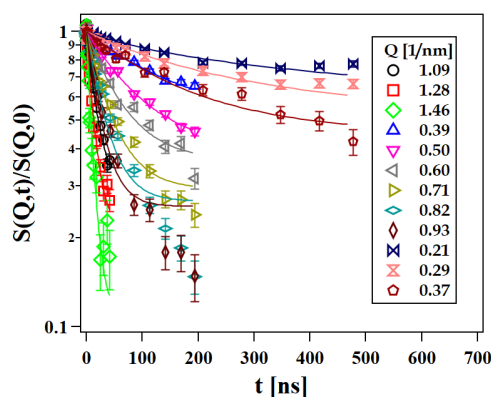


Figure C.8: NSE intermediate scattering functions of PESC samples with 1 wt% JR 400 and 5 mM SDP^- ($Z = 2$), fits according to eq. (5.2.8).

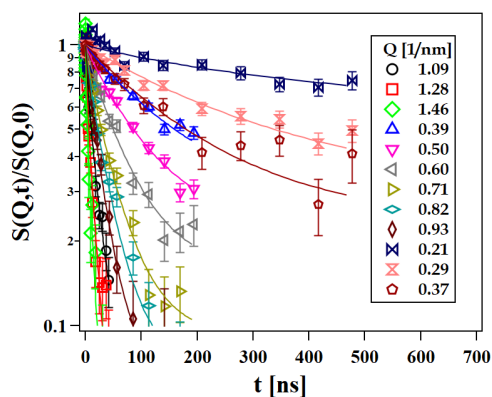


Figure C.9: NSE intermediate scattering functions of PESCs with 1 wt% JR 400 and 2 mM SDP^- ($Z = 5$), fits according to eq. (5.2.8).

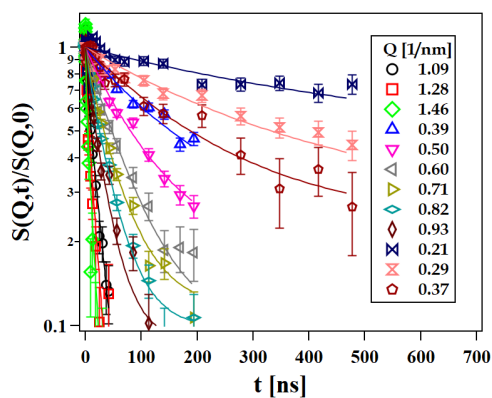


Figure C.10: NSE intermediate scattering functions of PESCs with 1 wt% JR 400 and 1.4 mM SDP^- ($Z = 7$), fits according to eq. (5.2.8).

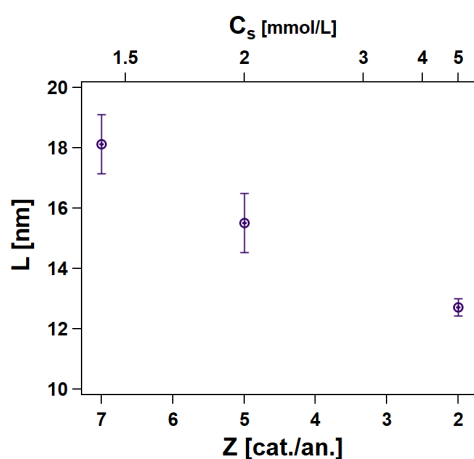


Figure C.11: Length of the mixed rodlike PE/surfactant aggregates for samples with 1 wt% JR 400 and SDP^- . The aggregates become slightly shorter as more surfactant is added.

Bibliography

- [1] ES Abdel-Halim. Chemical modification of cellulose extracted from sugarcane bagasse: Preparation of hydroxyethyl cellulose. *Arabian Journal of Chemistry*, 7(3):362–371, 2014.
- [2] Mark James Abraham, Teemu Murtola, Roland Schulz, Szilárd Páll, Jeremy C Smith, Berk Hess, and Erik Lindahl. Gromacs: High performance molecular simulations through multi-level parallelism from laptops to supercomputers. *SoftwareX*, 1:19–25, 2015.
- [3] Durga P Acharya and Hironobu Kunieda. Wormlike micelles in mixed surfactant solutions. *Advances in colloid and interface science*, 123:401–413, 2006.
- [4] Joseph Adelsberger, Amit Kulkarni, Abhinav Jain, Weinan Wang, Achille M Bivigou-Koumba, Peter Busch, Vitaliy Pipich, Olaf Holderer, Thomas Hellweg, Andre Laschewsky, et al. Thermoresponsive ps-b-pnipam-b-ps micelles: aggregation behavior, segmental dynamics, and thermal response. *Macromolecules*, 43(5):2490–2501, 2010.
- [5] S Aidarova, A Sharipova, J Krägel, and R Miller. Polyelectrolyte/surfactant mixtures in the bulk and at water/oil interfaces. *Advances in colloid and interface science*, 205:87–93, 2014.
- [6] Saeed Akbari, Syed Mohammad Mahmood, Hosein Ghaedi, and Sameer Al-Hajri. A new empirical model for viscosity of sulfonated polyacrylamide polymers. *Polymers*, 11(6):1046, 2019.

- [7] A. Akcasu, M. Benmouna, and C. C. Han. Interpretation of dynamic scattering from polymer solutions. *Polymer*, 21:866–890, August 1980.
- [8] Berni Julian Alder and Thomas Everett Wainwright. Phase transition for a hard sphere system. *The Journal of chemical physics*, 27(5):1208–1209, 1957.
- [9] Frank H Allen, Olga Kennard, David G Watson, Lee Brammer, A Guy Orpen, and Robin Taylor. Tables of bond lengths determined by x-ray and neutron diffraction. part 1. bond lengths in organic compounds. *Journal of the Chemical Society, Perkin Transactions 2*, (12):S1–S19, 1987.
- [10] Geoffrey Allen. Protein: A comprehensive treatise. 1997.
- [11] Mats Almgren, Per Hansson, Emad Mukhtar, and Jan Van Stam. Aggregation of alkyltrimethylammonium surfactants in aqueous poly (styrenesulfonate) solutions. *Langmuir*, 8(10):2405–2412, 1992.
- [12] Felix Ameseder, Aurel Radulescu, Olaf Holderer, Peter Falus, Dieter Richter, and Andreas M Stadler. Relevance of internal friction and structural constraints for the dynamics of denatured bovine serum albumin. *The journal of physical chemistry letters*, 9(10):2469–2473, 2018.
- [13] Hariprasad Ananth, Vinaya Kundapur, HS Mohammed, M Anand, GS Amarnath, and Sunil Mankar. A review on biomaterials in dental implantology. *International journal of biomedical science: IJBS*, 11(3):113, 2015.
- [14] KP Ananthapadmanabhan, G-Z Mao, ED Goddard, and M Tirrell. Surface forces measurements on a cationic polymer in the presence of an anionic??? *Colloids and surfaces*, 61:167–174, 1991.
- [15] Dan F Anghel, Françoise M Winnik, and Nicoleta Galatanu. Effect of the surfactant head group length on the interactions between polyethylene glycol monononylphenyl ethers and poly (acrylic acid). *Colloids and Surfaces A: Physicochemical and Engineering Aspects*, 149(1-3):339–345, 1999.
- [16] Markus Antonietti, Juergen Conrad, and Andreas Thuenemann. Polyelectrolyte-surfactant complexes: a new type of solid, mesomorphous material. *Macromolecules*, 27(21):6007–6011, 1994.
- [17] Haruhiko Arai, Moriyasu Murata, and Kozo Shinoda. The interaction between polymer and surfactant: The composition of the complex between polyvinylpyrrolidone and sodium alkyl sulfate as revealed by surface tension, dialysis, and solubilization. *Journal of Colloid and Interface Science*, 37(1):223–227, 1971.

- [18] Jun Arakawa and Brian A Pethica. Micellization in aqueous solutions of monoalkyl phosphate salts. *Journal of Colloid and Interface Science*, 75(2):441–450, 1980.
- [19] Michelle R Arkin, Yinyan Tang, and James A Wells. Small-molecule inhibitors of protein-protein interactions: progressing toward the reality. *Chemistry & biology*, 21(9):1102–1114, 2014.
- [20] Owen Arnold, Jean-Christophe Bilheux, JM Borreguero, Alex Buts, Stuart I Campbell, L Chapon, Mathieu Doucet, N Draper, R Ferraz Leal, MA Gigg, et al. Mantid—data analysis and visualization package for neutron scattering and μ sr experiments. *Nuclear Instruments and Methods in Physics Research Section A: Accelerators, Spectrometers, Detectors and Associated Equipment*, 764:156–166, 2014.
- [21] Julia Auernhammer, Tom Keil, Binbin Lin, Jan-Lukas Schäfer, Bai-Xiang Xu, Markus Biesalski, and Robert W Stark. Mapping humidity-dependent mechanical properties of a single cellulose fibre. *Cellulose*, 28(13):8313–8332, 2021.
- [22] Marc Baaden and Siewert J Marrink. Coarse-grain modelling of protein–protein interactions. *Current opinion in structural biology*, 23(6):878–886, 2013.
- [23] L Baba-Ahmed, M Benmouna, and MJ Grimson. Elastic scattering from charged colloidal dispersions. *Physics and Chemistry of Liquids an International Journal*, 16(3):235–238, 1987.
- [24] Guangyue Bai, Marieta Nichifor, Antonio Lopes, and Margarida Bastos. Thermodynamic characterization of the interaction behavior of a hydrophobically modified polyelectrolyte and oppositely charged surfactants in aqueous solution: effect of surfactant alkyl chain length. *The Journal of Physical Chemistry B*, 109(1):518–525, 2005.
- [25] Guangyue Bai, Luís MNBF Santos, Marieta Nichifor, António Lopes, and Margarida Bastos. Thermodynamics of the interaction between a hydrophobically modified polyelectrolyte and sodium dodecyl sulfate in aqueous solution. *The Journal of Physical Chemistry B*, 108(1):405–413, 2004.
- [26] Massimo Baiardo, Giovanna Frisoni, Mariastella Scandola, and Antonino Licciardello. Surface chemical modification of natural cellulose fibers. *Journal of Applied Polymer Science*, 83(1):38–45, 2002.
- [27] Livia Balacescu, Tobias E Schrader, Aurel Radulescu, Piotr Zolnierczuk, Olaf Holderer, Stefano Pasini, Jörg Fitter, and Andreas M Stadler. transition between protein-like and polymer-like dynamic behavior: internal friction in unfolded

- apomyoglobin depends on denaturing conditions. *Scientific reports*, 10(1):1–11, 2020.
- [28] E Bartsch, M Antonietti, W Schupp, and H Sillescu. Dynamic light scattering study of concentrated microgel solutions as mesoscopic model of the glass transition in quasiatonic fluids. *The Journal of chemical physics*, 97(6):3950–3963, 1992.
- [29] G Beaucage. Approximations leading to a unified exponential/power-law approach to small-angle scattering. *Journal of Applied Crystallography*, 28(6):717–728, 1995.
- [30] Reiner Beck, Michael Gradzielski, Klaus Horbaschek, S Sakhawat Shah, Heinz Hoffmann, and Pavel Strunz. Phase behavior, structure, and physical properties of the quaternary system tetradecyldimethylamine oxide, hcl, 1-hexanol, and water. *Journal of colloid and interface science*, 221(2):200–209, 2000.
- [31] Neda Beheshti, Giao TM Nguyen, Anna-Lena Kjøniksen, Kenneth D Knudsen, and Bo Nyström. Structure and dynamics of aqueous mixtures of an anionic cellulose derivative and anionic or cationic surfactants. *Colloids and Surfaces A: Physico-chemical and Engineering Aspects*, 279(1-3):40–49, 2006.
- [32] George I Bell. Models for the specific adhesion of cells to cells. *Science*, 200(4342):618–627, 1978.
- [33] Herman JC Berendsen, JPM van Postma, Wilfred F van Gunsteren, ARHJ DiNola, and Jan R Haak. Molecular dynamics with coupling to an external bath. *The Journal of chemical physics*, 81(8):3684–3690, 1984.
- [34] Bruce J Berne and Robert Pecora. *Dynamic light scattering: with applications to chemistry, biology, and physics*. Courier Corporation, 2000.
- [35] Jean-François Berret. Rheology of wormlike micelles: Equilibrium properties and shear banding transition. *arXiv preprint cond-mat/0406681*, 2004.
- [36] Christopher M Bishop. Pattern recognition. *Machine learning*, 128(9), 2006.
- [37] Francisco J Blanco, German Rivas, and Luis Serrano. A short linear peptide that folds into a native stable β -hairpin in aqueous solution. *Nature structural biology*, 1(9):584–590, 1994.
- [38] Brian Bolto and John Gregory. Organic polyelectrolytes in water treatment. *Water research*, 41(11):2301–2324, 2007.

- [39] David W Borhani and David E Shaw. The future of molecular dynamics simulations in drug discovery. *Journal of computer-aided molecular design*, 26(1):15–26, 2012.
- [40] S. Broersma. Rotational diffusion constant of a cylindrical particle. *J. Chem. Phys.*, 32:1626–1631, 1960.
- [41] Chrystal D Bruce, Max L Berkowitz, Lalith Perera, and Malcolm DE Forbes. Molecular dynamics simulation of sodium dodecyl sulfate micelle in water: micellar structural characteristics and counterion distribution. *The Journal of Physical Chemistry B*, 106(15):3788–3793, 2002.
- [42] Hugh D Burrows, Artur JM Valente, Telma Costa, Beverly Stewart, Maria J Tapia, and Ullrich Scherf. What conjugated polyelectrolytes tell us about aggregation in polyelectrolyte/surfactant systems. *Journal of Molecular Liquids*, 210:82–99, 2015.
- [43] Giovanni Bussi, Davide Donadio, and Michele Parrinello. Canonical sampling through velocity rescaling. *The Journal of chemical physics*, 126(1):014101, 2007.
- [44] B. Cabane, R. Duplessix, and T. Zemb. High resolution neutron scattering on ionic surfactant micelles : SDS in water. *J. Phys. France*, 46(12):2161–2178, 1985.
- [45] Michelle A Calabrese, Simon A Rogers, Ryan P Murphy, and Norman J Wagner. The rheology and microstructure of branched micelles under shear. *Journal of Rheology*, 59(5):1299–1328, 2015.
- [46] Michelle A Calabrese and Norman J Wagner. Detecting branching in wormlike micelles via dynamic scattering methods. *ACS Macro Letters*, 7(6):614–618, 2018.
- [47] SJ Candau and R Oda. Linear viscoelasticity of salt-free wormlike micellar solutions. *Colloids and Surfaces A: Physicochemical and Engineering Aspects*, 183:5–14, 2001.
- [48] Luigi Cannavacciuolo, Jan Skov Pedersen, and Peter Schurtenberger. Monte carlo simulation study of concentration effects and scattering functions for polyelectrolyte wormlike micelles. *Langmuir*, 18(7):2922–2932, 2002.
- [49] Jan-Michael Y Carrillo and Andrey V Dobrynin. Polyelectrolytes in salt solutions: Molecular dynamics simulations. *Macromolecules*, 44(14):5798–5816, 2011.
- [50] Achraf Chaker and Sami Boufi. Cationic nanofibrillar cellulose with high antibacterial properties. *Carbohydrate polymers*, 131:224–232, 2015.

- [51] Anjan Chakraborty, Debabrata Seth, Palash Setua, and Nilmoni Sarkar. Photoinduced electron transfer reaction in polymer-surfactant aggregates: Photoinduced electron transfer between n, n-dimethylaniline and 7-amino coumarin dyes. *The Journal of chemical physics*, 128(20):204510, 2008.
- [52] Tanushree Chakraborty, Indranil Chakraborty, and Soumen Ghosh. Sodium carboxymethylcellulose- ctab interaction: a detailed thermodynamic study of polymer- surfactant interaction with opposite charges. *Langmuir*, 22(24):9905–9913, 2006.
- [53] Surajit Chatterjee, Roopali Prajapati, Arpan Bhattacharya, and Tushar K Mukherjee. Microscopic evidence of “necklace and bead”-like morphology of polymer-surfactant complexes: a comparative study on poly (vinylpyrrolidone)–sodium dodecyl sulfate and poly (diallyldimethylammonium chloride)–sodium dodecyl sulfate systems. *Langmuir*, 30(32):9859–9865, 2014.
- [54] Shaoyu Chen, Romain Costil, Franco King-Chi Leung, and Ben L Feringa. Self-assembly of photoresponsive molecular amphiphiles in aqueous media. *Angewandte Chemie International Edition*, 60(21):11604–11627, 2021.
- [55] Leonardo Chiappisi, Ingo Hoffmann, and Michael Gradzielski. Complexes of oppositely charged polyelectrolytes and surfactants—recent developments in the field of biologically derived polyelectrolytes. *Soft Matter*, 9(15):3896–3909, 2013.
- [56] Leonardo Chiappisi, Dongcui Li, Norman J Wagner, and Michael Gradzielski. An improved method for analyzing isothermal titration calorimetry data from oppositely charged surfactant polyelectrolyte mixtures. *The Journal of Chemical Thermodynamics*, 68:48–52, 2014.
- [57] Leonardo Chiappisi, Sylvain Prévost, Isabelle Grillo, and Michael Gradzielski. Chitosan/alkylethoxy carboxylates: a surprising variety of structures. *Langmuir*, 30(7):1778–1787, 2014.
- [58] Leonardo Chiappisi, Miriam Simon, and Michael Gradzielski. Toward bioderived intelligent nanocarriers for controlled pollutant recovery and ph-sensitive binding. *ACS applied materials & interfaces*, 7(11):6139–6145, 2015.
- [59] Ioannis S Chronakis and Paschalis Alexandridis. Rheological properties of oppositely charged polyelectrolyte- surfactant mixtures: effect of polymer molecular weight and surfactant architecture. *Macromolecules*, 34(14):5005–5018, 2001.

- [60] Deh Ying Chu and JK Thomas. Effect of cationic surfactants on the conformation transition of poly (methacrylic acid). *Journal of the American Chemical Society*, 108(20):6270–6276, 1986.
- [61] Zonglin Chu, Cécile A Dreiss, and Yujun Feng. Smart wormlike micelles. *Chemical Society Reviews*, 42(17):7174–7203, 2013.
- [62] Ralph H Colby, DC Boris, WE Krause, and S Dou. Shear thinning of unentangled flexible polymer liquids. *Rheologica acta*, 46(5):569–575, 2007.
- [63] Viviana Cristiglio, Benjamin Giroud, Luc Didier, and Bruno Demé. D16 is back to business: more neutrons, more space, more fun. *Neutron News*, 26(3):22–24, 2015.
- [64] Vania Croce, Terence Cosgrove, Geoff Maitland, Trevor Hughes, and Göran Karlsson. Rheology, cryogenic transmission electron spectroscopy, and small-angle neutron scattering of highly viscoelastic wormlike micellar solutions. *Langmuir*, 19(20):8536–8541, 2003.
- [65] Kevin J Crowell and Peter M Macdonald. Characterization of cationic polyelectrolyte-induced domains in mixed popg- popc lipid bilayers via 2h nmr. *The Journal of Physical Chemistry B*, 101(7):1105–1109, 1997.
- [66] Erin E Dahlke and Donald G Truhlar. Assessment of the pairwise additive approximation and evaluation of many-body terms for water clusters. *The Journal of Physical Chemistry B*, 110(22):10595–10601, 2006.
- [67] S Dakhara and C Anajwala. Polyelectrolyte complex: A pharmaceutical review. *Systematic Reviews in Pharmacy*, 1(2):121, 2010.
- [68] Abhijit Dan, Soumen Ghosh, and Satya P Moulik. The solution behavior of poly (vinylpyrrolidone): its clouding in salt solution, solvation by water and isopropanol, and interaction with sodium dodecyl sulfate. *The Journal of Physical Chemistry B*, 112(12):3617–3624, 2008.
- [69] Sudipta Das, Baishali Ghosh, and Keya Sarkar. Nanocellulose as sustainable biomaterials for drug delivery. *Sensors International*, page 100135, 2021.
- [70] G Brent Dawe, Maria Musgaard, Mark RP Auroousseau, Naushaba Nayeem, Tim Green, Philip C Biggin, and Derek Bowie. Distinct structural pathways coordinate the activation of ampa receptor-auxiliary subunit complexes. *Neuron*, 89(6):1264–1276, 2016.

- [71] Pierre-Gilles De Gennes and Pierre-Gilles Gennes. *Scaling concepts in polymer physics*. Cornell university press, 1979.
- [72] Marco De Vivo, Matteo Masetti, Giovanni Bottegoni, and Andrea Cavalli. Role of molecular dynamics and related methods in drug discovery. *Journal of medicinal chemistry*, 59(9):4035–4061, 2016.
- [73] Giuseppe Rosario Del Sorbo, Viviana Cristiglio, Daniel Clemens, Ingo Hoffmann, and Emanuel Schneck. Influence of the surfactant tail length on the viscosity of oppositely charged polyelectrolyte/surfactant complexes. *Macromolecules*, 2021.
- [74] Giuseppe Rosario Del Sorbo, Sylvain Prévost, Emanuel Schneck, Michael Gradzielski, and Ingo Hoffmann. On the mechanism of shear-thinning in viscous oppositely charged polyelectrolyte surfactant complexes (PESCs). *J. Phys. Chem. B*, 124:909–913, 2020.
- [75] Lucie Delemotte, Mounir Tarek, Michael L Klein, Cristiano Amaral, and Werner Treptow. Intermediate states of the kv1. 2 voltage sensor from atomistic molecular dynamics simulations. *Proceedings of the National Academy of Sciences*, 108(15):6109–6114, 2011.
- [76] S Dhoot, ED Goddard, DS Murphy, and M Tirrell. Surface force measurements on cationic polymer/hyaluronic acid mixtures on mica. *Colloids and surfaces*, 66(2):91–96, 1992.
- [77] Birger Dittrich, Jens Lübben, Stefan Mebs, Armin Wagner, Peter Luger, and Ralf Flaig. Accurate bond lengths to hydrogen atoms from single-crystal x-ray diffraction by including estimated hydrogen adps and comparison to neutron and qm/mm benchmarks. *Chemistry–A European Journal*, 23(19):4605–4614, 2017.
- [78] R Dönges. Non-ionic cellulose ethers. *British polymer journal*, 23(4):315–326, 1990.
- [79] Cecile A Dreiss. Wormlike micelles: where do we stand? recent developments, linear rheology and scattering techniques. *Soft Matter*, 3(8):956–970, 2007.
- [80] Ron O Dror, Hillary F Green, Celine Valant, David W Borhani, James R Valcourt, Albert C Pan, Daniel H Arlow, Meritxell Canals, J Robert Lane, Raphaël Rahmani, et al. Structural basis for modulation of a g-protein-coupled receptor by allosteric drugs. *Nature*, 503(7475):295–299, 2013.

- [81] Paul L Dubin, James H Gruber, Jiulin Xia, and Huiwen Zhang. The effect of cations on the interaction between dodecylsulfate micelles and poly(ethyleneoxide). *Journal of Colloid and Interface Science*, 148(1):35–41, January 1992.
- [82] E. Dubois-Violette and P. G. De Gennes. Quasi-elastic scattering by dilute ideal polymer solutions .2. effects of hydrodynamic interactions. *Phys. (New York)*, 3:181, 1967.
- [83] Jacob D Durrant and J Andrew McCammon. Molecular dynamics simulations and drug discovery. *BMC biology*, 9(1):1–9, 2011.
- [84] Aaron PR Eberle and Lionel Porcar. Flow-sans and rheo-sans applied to soft matter. *Current opinion in colloid & interface science*, 17(1):33–43, 2012.
- [85] JA Epaarachchi. The effect of viscoelasticity on fatigue behaviour of polymer matrix composites. In *Creep and fatigue in polymer matrix composites*, pages 492–513. Elsevier, 2011.
- [86] Ulrich Essmann, Lalith Perera, Max L Berkowitz, Tom Darden, Hsing Lee, and Lee G Pedersen. A smooth particle mesh ewald method. *The Journal of chemical physics*, 103(19):8577–8593, 1995.
- [87] Evan Evans and Ken Ritchie. Dynamic strength of molecular adhesion bonds. *Biophysical journal*, 72(4):1541–1555, 1997.
- [88] B Farago, P Falus, I Hoffmann, M Gradzielski, F Thomas, and C Gomez. The in15 upgrade. *Neutron News*, 26(3):15–17, 2015.
- [89] Charl FJ Faul and Markus Antonietti. Facile synthesis of optically functional, highly organized nanostructures: dye–surfactant complexes. *Chemistry–A European Journal*, 8(12):2764–2768, 2002.
- [90] Guilherme A Ferreira and Watson Loh. Liquid crystalline nanoparticles formed by oppositely charged surfactant-polyelectrolyte complexes. *Current opinion in colloid & interface science*, 32:11–22, 2017.
- [91] S Förster, M Konrad, and P Lindner. Shear thinning and orientational ordering of wormlike micelles. *Physical review letters*, 94(1):017803, 2005.
- [92] H. Fruhner and G. Kretzschmar. The interaction of anionic surfactants with gelatin. *Colloid & Polymer Science*, 270(2):177–182, February 1992.

- [93] Hiroyuki Fukui, Iwao Satake, and Katumitu Hayakawa. Thermodynamic effects of alcohol additives on the cooperative binding of sodium dodecyl sulfate to a cationic polymer. *Langmuir*, 18(11):4465–4470, 2002.
- [94] RA Gelman. Hydrophobically modified hydroxyethylcellulose. In *TAPPI International Dissolving Pulps Conference, Geneva, Switzerland*, pages 159–165, 1987.
- [95] Otto Glatter, Gerhard Fritz, Helmut Lindner, Judith Brunner-Popela, Rainer Mittelbach, Reinhard Strey, and Stefan U. Egelhaaf. Nonionic micelles near the critical point: micellar growth and attractive interaction. 16(23):8692–8701, September 2000.
- [96] S Gnanakaran, Hugh Nymeyer, John Portman, Kevin Y Sanbonmatsu, and Angel E Garcia. Peptide folding simulations. *Current opinion in structural biology*, 13(2):168–174, 2003.
- [97] E. D. Goddard and R. B. Hannan. Polymer/surfactant interactions. *Journal of the American Oil Chemists' Society*, 54(12):561–566, 1977.
- [98] E Desmond Goddard and James V Gruber. *Principles of polymer science and technology in cosmetics and personal care*. CRC Press, 1999.
- [99] ED Goddard. Polymer—surfactant interaction part i. uncharged water-soluble polymers and charged surfactants. *Colloids and surfaces*, 19(2-3):255–300, 1986.
- [100] ED Goddard and RB Hannan. Cationic polymer/anionic surfactant interactions. *Journal of Colloid and Interface Science*, 55(1):73–79, 1976.
- [101] ED Goddard and PS Leung. Complexes of cationic polymers and anionic surfactants. In *Microdomains in Polymer Solutions*, pages 407–415. Springer, 1985.
- [102] ED Goddard, PS Leung, and KPA Padmanabhan. Novel gelling structures based on polymer/surfactant systems. *J. Soc. Cosmet. Chem*, 42(1):19, 1991.
- [103] ED Goddard, TS Phillips, and RB Hannan. Water soluble polyelectrolyte-il interaction—part i. *J. Soc. Cosmet. Chem.*, 26:461–475, 1975.
- [104] Marganit Goldraich, JR Schwartz, JL Burns, and Y Talmon. Microstructures formed in a mixed system of a cationic polymer and an anionic surfactant. *Colloids and Surfaces A: Physicochemical and Engineering Aspects*, 125(2-3):231–244, 1997.

- [105] James William Goodwin and Roy W Hughes. *Rheology for chemists: an introduction*. Royal Society of Chemistry, 2008.
- [106] Monojoy Goswami, Jose M Borreguero, Philip A Pincus, and Bobby G Sumpter. Surfactant-mediated polyelectrolyte self-assembly in a polyelectrolyte–surfactant complex. *Macromolecules*, 48(24):9050–9059, 2015.
- [107] Michael Gradzielski and Ingo Hoffmann. Polyelectrolyte-surfactant complexes (pescs) composed of oppositely charged components. *Current opinion in colloid & interface science*, 35:124–141, 2018.
- [108] Melville S Green and Arthur V Tobolsky. A new approach to the theory of relaxing polymeric media. *The Journal of Chemical Physics*, 14(2):80–92, 1946.
- [109] Francois Guillemet and Lennart Piculell. Interactions in aqueous mixtures of hydrophobically modified polyelectrolyte and oppositely charged surfactant. mixed micelle formation and associative phase separation. *The Journal of Physical Chemistry*, 99(22):9201–9209, 1995.
- [110] Samuel Guillot, Daragh McLoughlin, Nirmesh Jain, Michel Delsanti, and Dominique Langevin. Polyelectrolyte–surfactant complexes at interfaces and in bulk. *Journal of Physics: Condensed Matter*, 15(1):S219, 2002.
- [111] James Gumbart, Yi Wang, Alekseij Aksimentiev, Emad Tajkhorshid, and Klaus Schulten. Molecular dynamics simulations of proteins in lipid bilayers. *Current opinion in structural biology*, 15(4):423–431, 2005.
- [112] SK Hait, PR Majhi, A Blume, and SP Moulik. A critical assessment of micellization of sodium dodecyl benzene sulfonate (sdbbs) and its interaction with poly (vinyl pyrrolidone) and hydrophobically modified polymers, jr 400 and lm 200. *The Journal of Physical Chemistry B*, 107(15):3650–3658, 2003.
- [113] Per Hansson. A fluorescence study of divalent and monovalent cationic surfactants interacting with anionic polyelectrolytes. *Langmuir*, 17(14):4161–4166, 2001.
- [114] Per Hansson and Mats Almgren. Interaction of c n tab with sodium (carboxymethyl) cellulose: Effect of polyion linear charge density on binding isotherms and surfactant aggregation number. *The Journal of Physical Chemistry*, 100(21):9038–9046, 1996.
- [115] Akihito Hashidzume, Takeshi Ohara, and Yotaro Morishima. Coacervation of hydrophobically modified polyanions by association with nonionic surfactants in water. *Langmuir*, 18(24):9211–9218, 2002.

- [116] Puthusserickal A Hassan, Suman Rana, and Gunjan Verma. Making sense of brownian motion: colloid characterization by dynamic light scattering. *Langmuir*, 31(1):3–12, 2015.
- [117] Katumitu Hayakawa and Jan CT Kwak. Surfactant-polyelectrolyte interactions. 1. binding of dodecyltrimethylammonium ions by sodium dextransulfate and sodium poly (styrenesulfonate) in aqueous solution in the presence of sodium chloride. *The Journal of Physical Chemistry*, 86(19):3866–3870, 1982.
- [118] Katumitu Hayakawa, J Paul Santerre, and Jan CT Kwak. Study of surfactant-polyelectrolyte interactions. binding of dodecyl-and tetradecyltrimethylammonium bromide by some carboxylic polyelectrolytes. *Macromolecules*, 16(10):1642–1645, 1983.
- [119] John B. Hayter and Jeff Penfold. Self-consistent structural and dynamic study of concentrated micelle solutions. *J. Chem. Soc., Faraday Trans. 1*, 77:1851–1863, 1981.
- [120] Laura M Hillscher, Valentina J Liebich, Olga Avrutina, Markus Biesalski, and Harald Kolmar. Functional paper-based materials for diagnostics. *Chemtexts*, 7(2):1–22, 2021.
- [121] Jason Hodde. Naturally occurring scaffolds for soft tissue repair and regeneration. *Tissue engineering*, 8(2):295–308, 2002.
- [122] Erlend Hoff, Bo Nyström, and Björn Lindman. Polymer- surfactant interactions in dilute mixtures of a nonionic cellulose derivative and an anionic surfactant. *Langmuir*, 17(1):28–34, 2001.
- [123] I Hoffmann, B Farago, R Schweins, P Falus, M Sharp, and M Gradzielski. Structure and dynamics of polyelectrolytes in viscous polyelectrolyte-surfactant complexes at the mesoscale. *EPL (Europhysics Letters)*, 104(2):28001, 2013.
- [124] I Hoffmann, S Prévost, M Medebach, S Rogers, NJ Wagner, and M Gradzielski. Control of rheological behaviour with oppositely charged polyelectrolyte surfactant mixtures. *Tenside Surfactants Detergents*, 48(6):488–494, 2011.
- [125] Ingo Hoffmann, Bela Farago, Ralf Schweins, Peter Falus, Melissa Sharp, Sylvain Prévost, and Michael Gradzielski. On the mesoscopic origins of high viscosities in some polyelectrolyte-surfactant mixtures. *The Journal of chemical physics*, 143(7):074902, 2015.

- [126] Ingo Hoffmann, Peggy Heunemann, Sylvain Prévost, Ralf Schweins, Norman J Wagner, and Michael Gradzielski. Self-aggregation of mixtures of oppositely charged polyelectrolytes and surfactants studied by rheology, dynamic light scattering and small-angle neutron scattering. *Langmuir*, 27(8):4386–4396, 2011.
- [127] Ingo Hoffmann, Miriam Simon, Markus Bleuel, Peter Falus, and Michael Gradzielski. Structure, dynamics, and composition of large clusters in polyelectrolyte–surfactant systems. *Macromolecules*, 52(6):2607–2615, March 2019.
- [128] Ingo Hoffmann, Miriam Simon, Bela Farago, Ralf Schweins, Peter Falus, Olaf Holderer, and Michael Gradzielski. Structure and dynamics of polyelectrolyte surfactant mixtures under conditions of surfactant excess. *The Journal of chemical physics*, 145(12):124901, 2016.
- [129] Scott A Hollingsworth and Ron O Dror. Molecular dynamics simulation for all. *Neuron*, 99(6):1129–1143, 2018.
- [130] K. Holmberg, B. Jönsson, B. Kronberg, and B. Lindman. *Surfactants and Polymers in Aqueous Solution*. John Wiley & Sons, Ltd, Chichester, UK, October 2002.
- [131] Nathaniel Huebsch and David J Mooney. Inspiration and application in the evolution of biomaterials. *Nature*, 462(7272):426–432, 2009.
- [132] M Hulden. Hydrophobically modified urethane—ethoxylate (heur) associative thickeners 1. rheology of aqueous solutions and interactions with surfactants. *Colloids and Surfaces A: Physicochemical and Engineering Aspects*, 82(3):263–277, 1994.
- [133] Philippe H Hünenberger. Thermostat algorithms for molecular dynamics simulations. *Advanced computer simulation*, pages 105–149, 2005.
- [134] Oladeji O Ige, Lasisi E Umoru, and Sunday Aribo. Natural products: a minefield of biomaterials. *International Scholarly Research Notices*, 2012, 2012.
- [135] Wonpil Im and Benoît Roux. Ions and counterions in a biological channel: a molecular dynamics simulation of ompf porin from escherichia coli in an explicit membrane with 1 m kcl aqueous salt solution. *Journal of molecular biology*, 319(5):1177–1197, 2002.
- [136] Jacob N Israelachvili, D John Mitchell, and Barry W Ninham. Theory of self-assembly of hydrocarbon amphiphiles into micelles and bilayers. *Journal of the Chemical Society, Faraday Transactions 2: Molecular and Chemical Physics*, 72:1525–1568, 1976.

- [137] Nirmesh Jain, Siwar Trabelsi, Samuel Guillot, Daragh McLoughlin, Dominique Langevin, Pierre Letellier, and Mireille Turmine. Critical aggregation concentration in mixed solutions of anionic polyelectrolytes and cationic surfactants. *Langmuir*, 20(20):8496–8503, 2004.
- [138] Morten Ø Jensen, Vishwanath Jogini, David W Borhani, Abba E Leffler, Ron O Dror, and David E Shaw. Mechanism of voltage gating in potassium channels. *Science*, 336(6078):229–233, 2012.
- [139] PG Jones. Crystal structure determination: a critical view. *Chemical Society Reviews*, 13(2):157–172, 1984.
- [140] Yasushi Kakizawa and Miyuki Miyake. Creation of new functions by combination of surfactant and polymer-complex coacervation with oppositely charged polymer and surfactant for shampoo and body wash. *Journal of oleo science*, page ess19081, 2019.
- [141] Matej Kanduč, Emanuel Schneck, Philip Loche, Steven Jansen, H Jochen Schenk, and Roland R Netz. Cavitation in lipid bilayers poses strict negative pressure stability limit in biological liquids. *Proceedings of the National Academy of Sciences*, 117(20):10733–10739, 2020.
- [142] Matthias Karg, Isabel Pastoriza-Santos, Luis M Liz-Marzán, and Thomas Hellweg. A versatile approach for the preparation of thermosensitive pnipam core–shell microgels with nanoparticle cores. *ChemPhysChem*, 7(11):2298–2301, 2006.
- [143] U Kästner, H Hoffmann, R Dönges, and R Ehrler. Hydrophobically and cationically modified hydroxyethyl cellulose and their interactions with surfactants. *Colloids and Surfaces A: Physicochemical and Engineering Aspects*, 82(3):279–297, 1994.
- [144] U. Kästner, H. Hoffmann, R. Donges, and R. Ehrler. Interactions between modified hydroxyethyl cellulose (HEC) and surfactants. *Colloids Surf., A*, 112(2-3):209–225, 1996.
- [145] Susumu Kawamura. Effectiveness of natural polyelectrolytes in water treatment. *Journal-American Water Works Association*, 83(10):88–91, 1991.
- [146] Maciej Kawecki, Franz A Adlmann, Philipp Gutfreund, Peter Falus, David Uhrig, Sudipta Gupta, Bela Farago, Piotr Zolnierczuk, Malcom Cochran, and Max Wolff. Direct measurement of topological interactions in polymers under shear using neutron spin echo spectroscopy. *Scientific reports*, 9(1):1–6, 2019.

- [147] U Keiderling. The new ‘bersans-pc’ software for reduction and treatment of small angle neutron scattering data. *Applied physics A*, 74(1):s1455–s1457, 2002.
- [148] Aimee M Ketner, Rakesh Kumar, Tanner S Davies, Patrick W Elder, and Srinivasa R Raghavan. A simple class of photorheological fluids: surfactant solutions with viscosity tunable by light. *Journal of the American Chemical Society*, 129(6):1553–1559, 2007.
- [149] Ali Khademhosseini and Robert Langer. A decade of progress in tissue engineering. *Nature protocols*, 11(10):1775–1781, 2016.
- [150] Fatemeh Khalili-Araghi, James Gumbart, Po-Chao Wen, Marcos Sotomayor, Emad Tajkhorshid, and Klaus Schulten. Molecular dynamics simulations of membrane channels and transporters. *Current opinion in structural biology*, 19(2):128–137, 2009.
- [151] Nasreen Khan and Blair Brettmann. Intermolecular interactions in polyelectrolyte and surfactant complexes in solution. *Polymers*, 11(1):51, 2019.
- [152] Dieter Klemm, Brigitte Heublein, Hans-Peter Fink, and Andreas Bohn. Cellulose: fascinating biopolymer and sustainable raw material. *Angewandte chemie international edition*, 44(22):3358–3393, 2005.
- [153] Ksenija Kogej. Association and structure formation in oppositely charged polyelectrolyte–surfactant mixtures. *Advances in colloid and interface science*, 158(1-2):68–83, 2010.
- [154] Hiroyuki Kojima, Fumihiko Tanaka, Christine Scherzinger, and Walter Richtering. Temperature dependent phase behavior of pnipam microgels in mixed water/methanol solvents. *Journal of Polymer Science Part B: Polymer Physics*, 51(14):1100–1111, 2013.
- [155] Sabine Kosmella, Joachim Kötz, K Shirahama, and J Liu. Cooperative nature of complex formation in mixed polyelectrolyte- surfactant systems. *The Journal of Physical Chemistry B*, 102(34):6459–6464, 1998.
- [156] Dennis M Krüger and Shina CL Kamerlin. Micelle maker: An online tool for generating equilibrated micelles as direct input for molecular dynamics simulations. *ACS omega*, 2(8):4524–4530, 2017.
- [157] SK Kundu, S Gupta, J Stellbrink, L Willner, and D Richter. Relating structure and flow of soft colloids. *The European Physical Journal Special Topics*, 222(11):2757–2772, 2013.

- [158] Jan Cornelis Theodorus Kwak. *Polymer-surfactant systems*, volume 77. CRC Press, 1998.
- [159] Christopher N Lam, Changwoo Do, Yangyang Wang, Guan-Rong Huang, and Wei-Ren Chen. Structural properties of the evolution of ctab/nasal micelles investigated by sars and rheometry. *Physical Chemistry Chemical Physics*, 21(33):18346–18351, 2019.
- [160] Christian Lang, Joachim Kohlbrecher, Lionel Porcar, and Minne Paul Lettinga. The connection between biaxial orientation and shear thinning for quasi-ideal rods. *Polymers*, 8(8):291, 2016.
- [161] Christian Lang, Lionel Porcar, Hartmut Kriegs, and M Paul Lettinga. A quest for shear banding in ideal and non ideal colloidal rods. *Journal of Physics D: Applied Physics*, 52(7):074003, 2018.
- [162] Dominique Langevin. Complexation of oppositely charged polyelectrolytes and surfactants in aqueous solutions. a review. *Advances in colloid and interface science*, 147:170–177, 2009.
- [163] Yakov Lapitsky, Maider Parikh, and Eric W Kaler. Calorimetric determination of surfactant/polyelectrolyte binding isotherms. *The Journal of Physical Chemistry B*, 111(29):8379–8387, 2007.
- [164] André Laschewsky. Recent trends in the synthesis of polyelectrolytes. *Current Opinion in Colloid & Interface Science*, 17(2):56–63, April 2012.
- [165] J E Lennard-Jones. Cohesion. *Proceedings of the Physical Society*, 43(5):461–482, sep 1931.
- [166] Michael J Leonard and Helmut H Strey. Phase diagrams of stoichiometric polyelectrolyte- surfactant complexes. *Macromolecules*, 36(25):9549–9558, 2003.
- [167] PS Leung, ED Goddard, C Han, and CJ Glinka. A study of polycation—anionic-surfactant systems. *Colloids and surfaces*, 13:47–62, 1985.
- [168] Dongcui Li, Manish S Kelkar, and Norman J Wagner. Phase behavior and molecular thermodynamics of coacervation in oppositely charged polyelectrolyte/surfactant systems: a cationic polymer jr 400 and anionic surfactant sds mixture. *Langmuir*, 28(28):10348–10362, 2012.

- [169] Guobao Li, Hongmin Ma, and Jingcheng Hao. Surfactant ion-selective electrodes: A promising approach to the study of the aggregation of ionic surfactants in solution. *Soft Matter*, 8(4):896–909, 2012.
- [170] Perry FC Lim, LY Chee, SB Chen, and Bing-Hung Chen. Study of interaction between cetyltrimethylammonium bromide and poly (acrylic acid) by rheological measurements. *The Journal of Physical Chemistry B*, 107(26):6491–6496, 2003.
- [171] Björn Lindman, Filipe Antunes, Saule Aidarova, Maria Miguel, and Tommy Nylander. Polyelectrolyte-surfactant association—from fundamentals to applications. *Colloid Journal*, 76(5):585–594, 2014.
- [172] Bjorn Lindman, Kyrre Thalberg, ED Goddard, and KP Ananthapadmanabhan. Interactions of surfactants with polymers and proteins. *CRC, Boca Raton*, 203, 1993.
- [173] Roger CW Liu, Yotaro Morishima, and Francoise M Winnik. Rheological properties of mixtures of oppositely charged polyelectrolytes. a study of the interactions between a cationic cellulose ether and a hydrophobically modified poly [sodium 2-(acrylamido)-2-methylpropanesulfonate]. *Polymer journal*, 34(5):340–346, 2002.
- [174] Xiaoqing Liu, Jean-Paul Chapel, and Christophe Schatz. Structure, thermodynamic and kinetic signatures of a synthetic polyelectrolyte coacervating system. *Advances in colloid and interface science*, 239:178–186, 2017.
- [175] Xiaoyang Liu and Nicholas L Abbott. Spatial and temporal control of surfactant systems. *Journal of colloid and interface science*, 339(1):1–18, 2009.
- [176] Zhenhai Liu, Yazhuo Shang, Jian Feng, Changjun Peng, Honglai Liu, and Ying Hu. Effect of hydrophilicity or hydrophobicity of polyelectrolyte on the interaction between polyelectrolyte and surfactants: molecular dynamics simulations. *The Journal of Physical Chemistry B*, 116(18):5516–5526, 2012.
- [177] Dennis WPM Löwik, EHP Leunissen, Maaïke van den Heuvel, MB Hansen, and Jan CM van Hest. Stimulus responsive peptide based materials. *Chemical Society Reviews*, 39(9):3394–3412, 2010.
- [178] Alexander D MacKerell Jr. Empirical force fields for biological macromolecules: overview and issues. *Journal of computational chemistry*, 25(13):1584–1604, 2004.
- [179] A Maestro, C Gonzalez, and JM Gutierrez. Rheological behavior of hydrophobically modified hydroxyethyl cellulose solutions: A linear viscoelastic model. *Journal of rheology*, 46(1):127–143, 2002.

- [180] Anna Malovikova, Katumitu Hayakawa, and Jan CT Kwak. Surfactant-polyelectrolyte interactions. 4. surfactant chain length dependence of the binding of alkylpyridinium cations to dextran sulfate. *The Journal of Physical Chemistry*, 88(10):1930–1933, 1984.
- [181] Angelo S Mao and David J Mooney. Regenerative medicine: current therapies and future directions. *Proceedings of the National Academy of Sciences*, 112(47):14452–14459, 2015.
- [182] Fabrizio Marinelli, Fabio Pietrucci, Alessandro Laio, and Stefano Piana. A kinetic model of trp-cage folding from multiple biased molecular dynamics simulations. *PLoS Comput Biol*, 5(8):e1000452, 2009.
- [183] Eduardo F Marques, Oren Regev, Ali Khan, Maria da Graça Miguel, and Björn Lindman. Interactions between catanionic vesicles and oppositely charged polyelectrolytes phase behavior and phase structure. *Macromolecules*, 32(20):6626–6637, 1999.
- [184] Bruno Medronho, Anabela Romano, Maria Graça Miguel, Lars Stigsson, and Björn Lindman. Rationalizing cellulose (in) solubility: reviewing basic physicochemical aspects and role of hydrophobic interactions. *Cellulose*, 19(3):581–587, 2012.
- [185] TG Meikle, CJ Drummond, Frances Separovic, and CE Conn. Membrane-mimetic inverse bicontinuous cubic phase systems for encapsulation of peptides and proteins. In *Advances in Biomembranes and Lipid Self-Assembly*, volume 25, pages 63–94. Elsevier, 2017.
- [186] Venkata S Meka, Manprit KG Sing, Mallikarjuna R Pichika, Srinivasa R Nali, Venkata RM Kolapalli, and Prashant Kesharwani. A comprehensive review on polyelectrolyte complexes. *Drug discovery today*, 22(11):1697–1706, 2017.
- [187] Róbert Mészáros, Laurie Thompson, Martin Bos, Imre Varga, and Tibor Gilányi. Interaction of sodium dodecyl sulfate with polyethyleneimine: surfactant-induced polymer solution colloid dispersion transition. *Langmuir*, 19(3):609–615, 2003.
- [188] Ferenc Mezei. Neutron spin echo: A new concept in polarized thermal neutron techniques. *Zeitschrift für Physik A Hadrons and nuclei*, 255(2):146–160, 1972.
- [189] Ferenc Mezei, Catherine Pappas, and Thomas Gutberlet. *Neutron spin echo spectroscopy: Basics, trends and applications*, volume 601. Springer Science & Business Media, 2002.

- [190] Carolina Montoya, Yu Du, Anthony L Gianforcaro, Santiago Orrego, Maobin Yang, and Peter I Lelkes. On the road to smart biomaterials for bone research: definitions, concepts, advances, and outlook. *Bone Research*, 9(1):1–16, 2021.
- [191] David A Mortimer. Synthetic polyelectrolytes—a review. *Polymer International*, 25(1):29–41, 1991.
- [192] Michael Muthig, Sylvain Prévost, Reinhold Orglmeister, and Michael Gradzielski. Saset: a program for series analysis of small-angle scattering data. *Journal of Applied Crystallography*, 46(4):1187–1195, 2013.
- [193] Kyoyu Nakayama, Isao Tari, Masashi Sakai, Yoshio MURATA, and Gohsuke SUGIHARA. Aggregation behavior of sodium mono-n-dodecyl phosphate surfactant in aqueous media, and function in catalytic activity. i. multi-step aggregates formation and catalytic activity for hydrolysis of p-nitrophenyl acetate in aqueous solution. *Journal of Oleo Science*, 53(5):247–265, 2004.
- [194] F Nallet, G Jannink, JB Hayter, R Oberthür, and C Picot. Observation of the dynamics of polyelectrolyte strong solutions by quasi-elastic neutron scattering. *Journal de Physique*, 44(1):87–99, 1983.
- [195] KL Ngai. Dynamics of semidilute solutions of polymers and associating polymers. *Advances in colloid and interface science*, 64:1–43, 1996.
- [196] M Nierlich, CE Williams, François Boué, JP Cotton, M Daoud, B Famoux, G Jannink, Cl Picot, M Moan, C Wolff, et al. Small angle neutron scattering by semidilute solutions of polyelectrolyte. *Journal de Physique*, 40(7):701–704, 1979.
- [197] Susanne Nilsson, Krister Thuresson, Per Hansson, and Björn Lindman. Mixed solutions of surfactant and hydrophobically modified polymer. controlling viscosity with micellar size. *The Journal of Physical Chemistry B*, 102(37):7099–7105, 1998.
- [198] Takuhiro Nishio and Toshio Shimizu. Model analysis of surfactant–polymer interaction as cooperative ligand binding to linear lattice. *Biophysical chemistry*, 117(1):19–25, 2005.
- [199] Takuhiro Nishio, Toshio Shimizu, Jan CT Kwak, and Akira Minakata. The cooperative binding of large ligands to a one-dimensional lattice: the steric hindrance effect. *Biophysical chemistry*, 104(2):501–508, 2003.
- [200] Christopher K Ober and Gerhard Wegner. Polyelectrolyte–surfactant complexes in the solid state: Facile building blocks for self-organizing materials. *Advanced Materials*, 9(1):17–31, 1997.

- [201] K Ohbu, O Hiraishi, and I Kashiwa. Effect of quaternary ammonium substitution of hydroxyethylcellulose on binding of dodecyl sulfate. *Journal of the American Oil Chemists' Society*, 59(2):108–112, 1982.
- [202] Ulf Olsson, Kozo Shinoda, and Bjoern Lindman. Change of the structure of microemulsions with the hydrophile-lipophile balance of nonionic surfactant as revealed by nmr self-diffusion studies. *The Journal of Physical Chemistry*, 90(17):4083–4088, 1986.
- [203] Chris Oostenbrink, Alessandra Villa, Alan E Mark, and Wilfred F Van Gunsteren. A biomolecular force field based on the free enthalpy of hydration and solvation: the gromos force-field parameter sets 53a5 and 53a6. *Journal of computational chemistry*, 25(13):1656–1676, 2004.
- [204] A. Ortega and J. García De La Torre. Hydrodynamic properties of rodlike and disklike particles in dilute solution. *J. Chem. Phys.*, 119:9914–9919, 2003.
- [205] Yoshihito Osada and Alexei Khokhlov. *Polymer gels and networks*. CRC Press, 2001.
- [206] Santipharp Panmai, Robert K Prud'homme, Dennis G Peiffer, Steffen Jockusch, and Nicholas J Turro. Interactions between hydrophobically modified polymers and surfactants: a fluorescence study. *Langmuir*, 18(10):3860–3864, 2002.
- [207] Robert Pelton. Temperature-sensitive aqueous microgels. *Advances in colloid and interface science*, 85(1):1–33, 2000.
- [208] Willis B Person, George R Anderson, James N Fordemwalt, H Stammreich, and Roberto Forneris. Infrared and raman spectra, force constants, and the structures of some polyhalide ions: Icl_2^- , icl_4^- , brcl_2^- , and br_3^- . *The Journal of Chemical Physics*, 35(3):908–914, 1961.
- [209] Lennart Piculell and Björn Lindman. Association and segregation in aqueous polymer/polymer, polymer/surfactant, and surfactant/surfactant mixtures: similarities and differences. *Advances in Colloid and Interface Science*, 41:149–178, 1992.
- [210] Nopparat Plucktaveesak, Andrew J Konop, and Ralph H Colby. Viscosity of polyelectrolyte solutions with oppositely charged surfactant. *The Journal of Physical Chemistry B*, 107(32):8166–8171, 2003.
- [211] G Porod. General theory. In *Small angle X-ray scattering*. 1982.

- [212] Alexandre GS Prado, Julio L Macedo, Sílvia CL Dias, and José A Dias. Calorimetric studies of the association of chitin and chitosan with sodium dodecyl sulfate. *Colloids and surfaces B: Biointerfaces*, 35(1):23–27, 2004.
- [213] M Prasad, R Palepu, and SP Moulik. Interaction between sodium dodecyl sulfate (sds) and polyvinylpyrrolidone (pvp) investigated with forward and reverse component addition protocols employing tensiometric, conductometric, microcalorimetric, electrokinetic, and dls techniques. *Colloid and Polymer Science*, 284(8):871–878, 2006.
- [214] PN Pusey. Correlation and light beating spectroscopy, 1974.
- [215] Srinivasa R Raghavan and Eric W Kaler. Highly viscoelastic wormlike micellar solutions formed by cationic surfactants with long unsaturated tails. *Langmuir*, 17(2):300–306, 2001.
- [216] Deepa Rajamani, Spencer Thiel, Sandor Vajda, and Carlos J Camacho. Anchor residues in protein–protein interactions. *Proceedings of the National Academy of Sciences*, 101(31):11287–11292, 2004.
- [217] Radha Ranganathan, Linh Tran, and Barney L Bales. Surfactant-and salt-induced growth of normal sodium alkyl sulfate micelles well above their critical micelle concentrations. *The Journal of Physical Chemistry B*, 104(10):2260–2264, 2000.
- [218] Oren Regev, Eduardo F Marques, and Ali Khan. Polymer-induced structural effects on cationic vesicles: formation of faceted vesicles, disks, and cross-links. *Langmuir*, 15(2):642–645, 1999.
- [219] STA Regismond, FM Winnik, and ED Goddard. Surface viscoelasticity in mixed polycation anionic surfactant systems studied by a simple test. *Colloids and Surfaces A: Physicochemical and Engineering Aspects*, 119(2-3):221–228, 1996.
- [220] Sudarshi T. A. Regismond, Yew-Meng Heng, E. Desmond Goddard, and Françoise M. Winnik. Fluorescence microscopy observation of the adsorption onto hair of a fluorescently labeled cationic cellulose ether. *Langmuir*, 15(8):3007–3010, March 1999.
- [221] Stefan Reinicke, Matthias Karg, Alain Lapp, Lutz Heymann, Thomas Hellweg, and Holger Schmalz. Flow-induced ordering in cubic gels formed by p2vp-b-peo-b-p (gme-co-eg) triblock terpolymer micelles: A rheo-sans study. *Macromolecules*, 43(23):10045–10054, 2010.

- [222] D Richard, M Ferrand, and GJ Kearley. Analysis and visualisation of neutron-scattering data. *Journal of Neutron Research*, 4(1-4):33–39, 1996.
- [223] Dieter Richter, Michael Monkenbusch, Arantxa Arbe, and Juan Colmenero. Neutron spin echo in polymer systems. In *Neutron Spin Echo in Polymer Systems*, pages 1–221. Springer, 2005.
- [224] Matthias Rief, Mathias Gautel, Filipp Oesterhelt, Julio M Fernandez, and Hermann E Gaub. Reversible unfolding of individual titin immunoglobulin domains by afm. *science*, 276(5315):1109–1112, 1997.
- [225] EA Robinson and MW Lister. A linear relationship between bond orders and stretching force constants. *Canadian Journal of Chemistry*, 41(12):2988–2995, 1963.
- [226] S Rogers, J Kohlbrecher, and MP Lettinga. The molecular origin of stress generation in worm-like micelles, using a rheo-sans laos approach. *Soft Matter*, 8(30):7831–7839, 2012.
- [227] Paola Roscigno, Fioretta Asaro, Giorgio Pellizer, Ornella Ortona, and Luigi Paduano. Complex formation between poly (vinylpyrrolidone) and sodium decyl sulfate studied through nmr. *Langmuir*, 19(23):9638–9644, 2003.
- [228] Jonathan P Rothstein. Strong flows of viscoelastic wormlike micelle solutions. *Rheol. Rev*, 2008:1–46, 2008.
- [229] Iwao Satake and Jen Tsi Yang. Interaction of sodium decyl sulfate with poly (l-ornithine) and poly (l-lysine) in aqueous solution. *Biopolymers: Original Research on Biomolecules*, 15(11):2263–2275, 1976.
- [230] JEAN-PIERRE SCHERMANN. 1 - modelling. In JEAN-PIERRE SCHERMANN, editor, *Spectroscopy and Modeling of Biomolecular Building Blocks*, pages 1–57. Elsevier, Amsterdam, 2008.
- [231] Howard G Schild. Poly (n-isopropylacrylamide): experiment, theory and application. *Progress in polymer science*, 17(2):163–249, 1992.
- [232] Emanuel Schneck, Dominik Horinek, and Roland R Netz. Insight into the molecular mechanisms of protein stabilizing osmolytes from global force-field variations. *The Journal of Physical Chemistry B*, 117(28):8310–8321, 2013.
- [233] Sebastian Schoettl, Julien Marcus, Oliver Diat, Didier Touraud, Werner Kunz, Thomas Zemb, and Dominik Horinek. Emergence of surfactant-free micelles from ternary solutions. *Chemical Science*, 5(8):2949–2954, 2014.

- [234] Beth A Schubert, Norman J Wagner, Eric W Kaler, and Srinivasa R Raghavan. Shear-induced phase separation in solutions of wormlike micelles. *Langmuir*, 20(9):3564–3573, 2004.
- [235] Kenneth S Schweizer, Matthias Fuchs, G Szamel, Marina Guenza, and Hai Tang. Polymer-mode-coupling theory of the slow dynamics of entangled macromolecular fluids. *Macromolecular theory and simulations*, 6(6):1037–1117, 1997.
- [236] M.J Schwuger. Mechanism of interaction between ionic surfactants and polyglycol ethers in water. *Journal of Colloid and Interface Science*, 43(2):491–498, 1973.
- [237] Alec B Scranton, B Rangarajan, and J Klier. Biomedical applications of polyelectrolytes. *Biopolymers II*, pages 1–54, 1995.
- [238] Sobhan Sen, Dipankar Sukul, Partha Dutta, and Kankan Bhattacharyya. Fluorescence anisotropy decay in polymer- surfactant aggregates. *The Journal of Physical Chemistry A*, 105(32):7495–7500, 2001.
- [239] Sobhan Sen, Dipankar Sukul, Partha Dutta, and Kankan Bhattacharyya. Solvation dynamics in aqueous polymer solution and in polymer- surfactant aggregate. *The Journal of Physical Chemistry B*, 106(15):3763–3769, 2002.
- [240] Sanjay K Sharma and Ackmez Mudhoo. *A handbook of applied biopolymer technology: synthesis, degradation and applications*. Royal society of chemistry, 2011.
- [241] Qiang Shen, Hao Wei, Liancheng Wang, Yong Zhou, Ying Zhao, Zhiqing Zhang, Dujin Wang, Guiying Xu, and Duanfu Xu. Crystallization and aggregation behaviors of calcium carbonate in the presence of poly (vinylpyrrolidone) and sodium dodecyl sulfate. *The Journal of Physical Chemistry B*, 109(39):18342–18347, 2005.
- [242] Wenjian Shi, Yuanzhang Zhang, Qin Qin, and Xuan Chen. Research progress in novel functional materials—cationic cellulose. *Materials Review*, 1, 2010.
- [243] Indira H Shrivastava and Mark SP Sansom. Simulations of ion permeation through a potassium channel: molecular dynamics of kcsa in a phospholipid bilayer. *Biophysical journal*, 78(2):557–570, 2000.
- [244] David Sidler, Markus Meuwly, and Peter Hamm. An efficient water force field calibrated against intermolecular thz and raman spectra. *The Journal of chemical physics*, 148(24):244504, 2018.
- [245] Jesper Sjöström and Lennart Piculell. Interactions between cationically modified hydroxyethyl cellulose and oppositely charged surfactants studied by gel swelling

- experiments—effects of surfactant type, hydrophobic modification and added salt. *Colloids and Surfaces A: Physicochemical and Engineering Aspects*, 183:429–448, 2001.
- [246] Jiří Smilek, Sabína Jarábková, Tomáš Velcer, and Miloslav Pekař. Compositional and temperature effects on the rheological properties of polyelectrolyte–surfactant hydrogels. *Polymers*, 11(5):927, 2019.
- [247] Christopher D Snow, Bojan Zagrovic, and Vijay S Pande. The trp cage: folding kinetics and unfolded state topology via molecular dynamics simulations. *Journal of the American Chemical Society*, 124(49):14548–14549, 2002.
- [248] Markus Stieger and Walter Richtering. Shear-induced phase separation in aqueous polymer solutions: Temperature-sensitive microgels and linear polymer chains. *Macromolecules*, 36(23):8811–8818, 2003.
- [249] R. Strey. I. experimental facts: Water-nonionic surfactant systems, and the effect of additives. 100(3):182–189, March 1996.
- [250] Mikhail R Stukan, Edo S Boek, Johan T Padding, Wim J Briels, and John P Crawshaw. Flow of wormlike micelles in an expansion-contraction geometry. *Soft Matter*, 4(4):870–879, 2008.
- [251] Hao Sun, Christopher P Kabb, Michael B Sims, and Brent S Sumerlin. Architecture-transformable polymers: Reshaping the future of stimuli-responsive polymers. *Progress in Polymer Science*, 89:61–75, 2019.
- [252] Makiko Takeda, Takumi Kusano, Takuro Matsunaga, Hitoshi Endo, Mitsuhiro Shibayama, and Toshiyuki Shikata. Rheo-sans studies on shear-thickening/thinning in aqueous rodlike micellar solutions. *Langmuir*, 27(5):1731–1738, 2011.
- [253] K. C. Tam. Rheological properties of poly(ethylene oxide) in anionic surfactant solutions. In *Advances in Chemistry*, pages 205–217. American Chemical Society, January 1996.
- [254] R Tanaka, J Meadows, GO Phillips, and PA Williams. Viscometric and spectroscopic studies on the solution behaviour of hydrophobically modified cellulosic polymers. *Carbohydrate polymers*, 12(4):443–459, 1990.
- [255] Shuangcheng Tang. Synthesis and characterizations of stimuli-responsive polymeric materials for biomedical applications. 2015.

- [256] DJF Taylor, RK Thomas, PX Li, and J Penfold. Adsorption of oppositely charged polyelectrolyte/surfactant mixtures. neutron reflection from alkyl trimethylammonium bromides and sodium poly (styrenesulfonate) at the air/water interface: the effect of surfactant chain length. *Langmuir*, 19(9):3712–3719, 2003.
- [257] Eiji Terada, Yulia Samoshina, Tommy Nylander, and Björn Lindman. Adsorption of cationic cellulose derivatives/anionic surfactant complexes onto solid surfaces. i. silica surfaces. *Langmuir*, 20(5):1753–1762, 2004.
- [258] Kyrre Thalberg, Bjoern Lindman, and Gunnar Karlstroem. Phase diagram of a system of cationic surfactant and anionic polyelectrolyte: tetradecyltrimethylammonium bromide-hyaluronan-water. *Journal of Physical Chemistry*, 94(10):4289–4295, 1990.
- [259] Kyrre Thalberg, Bjoern Lindman, and Gunnar Karlstroem. Phase behavior of a system of cationic surfactant and anionic polyelectrolyte: the effect of salt. *The Journal of Physical Chemistry*, 95(15):6004–6011, 1991.
- [260] Prachi Thareja, Ingo H Hoffmann, Matthew W Liberatore, Matthew E Helgeson, Y Thomas Hu, Michael Gradzielski, and Norman J Wagner. Shear-induced phase separation (sips) with shear banding in solutions of cationic surfactant and salt. *Journal of Rheology*, 55(6):1375–1397, 2011.
- [261] Krister Thuresson, Svante Nilsson, and Björn Lindman. Effect of hydrophobic modification on phase behavior and rheology in mixtures of oppositely charged polyelectrolytes. *Langmuir*, 12(2):530–537, 1996.
- [262] S Trabelsi, S Guillot, H Ritacco, F Boué, and D Langevin. Nanostructures of colloidal complexes formed in oppositely charged polyelectrolyte/surfactant dilute aqueous solutions. *The European Physical Journal E*, 23(3):305–311, 2007.
- [263] S Trabelsi and D Langevin. Co-adsorption of carboxymethyl-cellulose and cationic surfactants at the air- water interface. *Langmuir*, 23(3):1248–1252, 2007.
- [264] Siwar Trabelsi, Pierre-Antoine Albouy, Marianne Impéror-Clerc, Samuel Guillot, and Dominique Langevin. X-ray diffraction study of the structure of carboxymethylcellulose–cationic surfactant complexes. *ChemPhysChem*, 8(16):2379–2385, 2007.
- [265] Marina Tsianou and Paschalis Alexandridis. Control of the rheological properties in solutions of a polyelectrolyte and an oppositely charged surfactant by the addition of cyclodextrins. *Langmuir*, 15(23):8105–8112, 1999.

- [266] Maren Umlandt, David Feldmann, Emanuel Schneck, Svetlana A Santer, and Marek Bekir. Adsorption of photoresponsive surfactants at solid–liquid interfaces. *Langmuir*, 36(46):14009–14018, 2020.
- [267] Karsten Vogtt, Miriam Siebenbürger, Daniel Clemens, Christian Rabe, Peter Lindner, Margarita Russina, Michael Fromme, Ferenc Mezei, and Matthias Ballauff. A new time-of-flight small-angle scattering instrument at the helmholtz-zentrum berlin: V16/vsans. *Journal of Applied Crystallography*, 47(1):237–244, 2014.
- [268] C Von Ferber and H Löwen. Complexes of polyelectrolytes and oppositely charged ionic surfactants. *The Journal of chemical physics*, 118(23):10774–10779, 2003.
- [269] Peter Walde, Michaela Wessicken, Ulf Rädler, Nathalie Berclaz, Kilian Conde-Frieboes, and Pier Luigi Luisi. Preparation and characterization of vesicles from mono-n-alkyl phosphates and phosphonates. *The Journal of Physical Chemistry B*, 101(38):7390–7397, 1997.
- [270] Torsten Wallin and Per Linse. Monte carlo simulations of polyelectrolytes at charged micelles. 1. effects of chain flexibility. *Langmuir*, 12(2):305–314, 1996.
- [271] Torsten Wallin and Per Linse. Monte carlo simulations of polyelectrolytes at charged micelles. 2. effects of linear charge density. *The Journal of Physical Chemistry*, 100(45):17873–17880, 1996.
- [272] C Wang and KC Tam. New insights on the interaction mechanism within oppositely charged polymer/surfactant systems. *Langmuir*, 18(17):6484–6490, 2002.
- [273] C Wang and KC Tam. Interactions between poly (acrylic acid) and sodium dodecyl sulfate: isothermal titration calorimetric and surfactant ion-selective electrode studies. *The Journal of Physical Chemistry B*, 109(11):5156–5161, 2005.
- [274] C Wang, KC Tam, RD Jenkins, and CB Tan. Interactions between methacrylic acid/ethyl acrylate copolymers and dodecyltrimethylammonium bromide. *The Journal of Physical Chemistry B*, 107(19):4667–4675, 2003.
- [275] Dali Wang, Yue Jin, Xinyuan Zhu, and Deyue Yan. Synthesis and applications of stimuli-responsive hyperbranched polymers. *Progress in Polymer Science*, 64:114–153, 2017.
- [276] Geng Wang and Gerd Olofsson. Titration calorimetric study of the interaction between ionic surfactants and uncharged polymers in aqueous solution. *The Journal of Physical Chemistry B*, 102(46):9276–9283, 1998.

- [277] Wei Wang, Wensheng Lu, and Long Jiang. Influence of ph on the aggregation morphology of a novel surfactant with single hydrocarbon chain and multi-amine headgroups. *The Journal of Physical Chemistry B*, 112(5):1409–1413, 2008.
- [278] Xiaoyong Wang, Jinben Wang, Yilin Wang, and Haike Yan. Salt effect on the complex formation between cationic gemini surfactant and anionic polyelectrolyte in aqueous solution. *Langmuir*, 20(21):9014–9018, 2004.
- [279] Ya Chung Wei and Samuel M Hudson. Binding of sodium dodecyl sulfate to a polyelectrolyte based on chitosan. *Macromolecules*, 26(16):4151–4154, 1993.
- [280] Yuan Wei and Michael JA Hore. Characterizing polymer structure with small-angle neutron scattering: A tutorial. *Journal of Applied Physics*, 129(17):171101, 2021.
- [281] Roger W. Welker. Chapter 4 - size analysis and identification of particles. In Rajiv Kohli and K.L. Mittal, editors, *Developments in Surface Contamination and Cleaning*, pages 179–213. William Andrew Publishing, Oxford, 2012.
- [282] Françoise M Winnik and Sudarshi TA Regismond. Fluorescence methods in the study of the interactions of surfactants with polymers. *Colloids and Surfaces A: Physicochemical and Engineering Aspects*, 118(1-2):1–39, 1996.
- [283] Françoise M Winnik, Sudarshi TA Regismond, and E Desmond Goddard. Interactions of an anionic surfactant with a fluorescent-dye-labeled hydrophobically-modified cationic cellulose ether. *Langmuir*, 13(1):111–114, 1997.
- [284] Mitchell A Winnik, Simon M Bystryak, Christophe Chassenieux, Vladimir Strashko, Peter M Macdonald, and Junaid Siddiqui. Study of interaction of poly (ethylene imine) with sodium dodecyl sulfate in aqueous solution by light scattering, conductometry, nmr, and microcalorimetry. *Langmuir*, 16(10):4495–4510, 2000.
- [285] John E Wong, Akhilesh K Gaharwar, Detlef Müller-Schulte, Dhirendra Bahadur, and Walter Richtering. Dual-stimuli responsive pnipam microgel achieved via layer-by-layer assembly: Magnetic and thermoresponsive. *Journal of colloid and interface science*, 324(1-2):47–54, 2008.
- [286] Sander Woutersen, Rolf Pfister, Peter Hamm, Yuguang Mu, Daniel S Kosov, and Gerhard Stock. Peptide conformational heterogeneity revealed from nonlinear vibrational spectroscopy and molecular-dynamics simulations. *The Journal of chemical physics*, 117(14):6833–6840, 2002.
- [287] Jiang Yang. Viscoelastic wormlike micelles and their applications. *Current opinion in colloid & interface science*, 7(5-6):276–281, 2002.

- [288] Li Yang, Lei Sun, and Wei-Qiao Deng. Combination rules for morse-based van der waals force fields. *The Journal of Physical Chemistry A*, 122(6):1672–1677, 2018.
- [289] Yuriy Zakrevskyy, Piotr Cywinski, Magdalena Cywinska, Jens Paasche, Nino Lomadze, Oliver Reich, Hans-Gerd Löhmannsröben, and Svetlana Santer. Interaction of photosensitive surfactant with dna and poly acrylic acid. *The Journal of chemical physics*, 140(4):01B613_1, 2014.
- [290] Yuriy Zakrevskyy, Marcel Richter, Svitlana Zakrevska, Nino Lomadze, Regine von Klitzing, and Svetlana Santer. Light-controlled reversible manipulation of microgel particle size using azobenzene-containing surfactant. *Advanced Functional Materials*, 22(23):5000–5009, 2012.
- [291] Fulong Zhang, Zhiqiang Pang, Cuihua Dong, and Zong Liu. Preparing cationic cotton linter cellulose with high substitution degree by ultrasonic treatment. *Carbohydrate Polymers*, 132:214–220, 2015.
- [292] Shuguang Zhang. Emerging biological materials through molecular self-assembly. *Biotechnology advances*, 20(5-6):321–339, 2002.
- [293] Yongmin Zhang, Zonglin Chu, Cécile A Dreiss, Yuejiao Wang, Chenhong Fei, and Yujun Feng. Smart wormlike micelles switched by co₂ and air. *Soft Matter*, 9(27):6217–6221, 2013.
- [294] Shuiqin Zhou, Christian Burger, and Benjamin Chu. Supramolecular structures of polyethylenimine-sodium alkyl sulfate complexes. *The Journal of Physical Chemistry B*, 108(30):10819–10824, 2004.
- [295] Shuiqin Zhou, Christian Burger, Fengji Yeh, and Benjamin Chu. Charge density effect of polyelectrolyte chains on the nanostructures of polyelectrolyte- surfactant complexes. *Macromolecules*, 31(23):8157–8163, 1998.
- [296] Shuiqin Zhou and Benjamin Chu. Assembled materials: polyelectrolyte–surfactant complexes. *Advanced Materials*, 12(8):545–556, 2000.
- [297] Shuiqin Zhou, Haibo Hu, Christian Burger, and Benjamin Chu. Phase structural transitions of polyelectrolyte- surfactant complexes between poly (vinylamine hydrochloride) and oppositely charged sodium alkyl sulfate. *Macromolecules*, 34(6):1772–1778, 2001.

- [298] Shuiqin Zhou, Chang Xu, Jun Wang, Patricia Golas, James Batteas, and Lowell Kreeger. Phase behavior of cationic hydroxyethyl cellulose- sodium dodecyl sulfate mixtures: effects of molecular weight and ethylene oxide side chain length of polymers. *Langmuir*, 20(20):8482–8489, 2004.
- [299] Shuiqin Zhou, Fengji Yeh, Christian Burger, and Benjamin Chu. Formation and transition of highly ordered structures of polyelectrolyte- surfactant complexes. *The Journal of Physical Chemistry B*, 103(12):2107–2112, 1999.
- [300] B. H. Zimm. Dynamics of polymer molecules in dilute solution: Viscoelasticity, flow birefringence and dielectric loss. *J. Chem. Phys.*, 24:269–278, 1956.
- [301] Bruno H Zimm and JK Bragg. Theory of the phase transition between helix and random coil in polypeptide chains. *The journal of chemical physics*, 31(2):526–535, 1959.